DI Andreas Egger

Mechanically Assisted Suction Reed Valve of a Hermetic Reciprocating Compressor

DISSERTATION / DOCTORAL THESIS

to achieve the university degree of
Doktor der technischen Wissenschaften

submitted to

Graz University of Technology

1st Reviewer

Ao.Univ.-Prof. Dipl.-Ing. Dr.techn. Raimund Almbauer
Institute of Internal Combustion Engines and Thermodynamics at Graz University of Technology

2nd Reviewer

Prof. Nikola Stosic
Department of Mechanical Engineering and Aeronautics at City University of London

Graz, April 2021

Institute of Internal Combustion Engines and Thermodynamics
Chairman: Univ.-Prof. DI Dr. Helmut Eichlseder

STATUTORY DECLARATION

I declare that I have authored this thesis independently, that I have not used other than the declared sources/resources, and that I have explicitly indicated all material which has been quoted either literally or by content from the sources used. The text document uploaded to TUGRAZonline is identical to the present dissertation.

EIDSTATTLICHE ERKLÄRUNG

Ich erkläre an Eides statt, dass ich die vorliegende Arbeit selbstständig verfasst, andere als die angegebenen Quellen/Hilfsmittel nicht benutzt, und die den benutzten Quellen wörtlich und inhaltlich entnommenen Stellen als solche kenntlich gemacht habe. Das in TUGRAZonline hochgeladene Textdokument ist mit der vorliegenden Dissertation identisch.

DI Andreas Egger

Graz, Datum

ACKNOWLEDGEMENTS

This dissertation was written as part of my work as a project assistant at the Institute of Internal Combustion Engines and Thermodynamics (IVT) - Department of Thermodynamics at Graz University of Technology. The underlying work was funded through a research project called eValD, which was supported by the Austrian Research Promotion Agency (FFG) under reference number 861517 and by Secop GmbH.

First of all, I would like to thank Univ.-Prof. Dipl.-Ing. Dr.techn. Helmut Eichlseder (Head of the Institute) and Ao.Univ.-Prof. Dipl.-Ing. Dr.techn. Raimund Almbauer (Head of the Thermodynamics Department) for the opportunity to write a dissertation at the IVT.

Special thanks go to Prof. Almbauer for the excellent supervision of my work. In the course of numerous discussions, many good ideas as well as constructive and creative inputs emerged, which enriched my work. I would also like to highlight his willingness to help quickly and with great effort whenever I asked for it. Many thanks also for the trust and the opportunity to take on responsibility, not only in the context of this dissertation, but also in other projects of the department. This allowed me to put the theoretical knowledge from various courses in project management and leadership into practice and gain valuable experience.

Many thanks also to Prof. Nikola Stosic, who immediately agreed to do the second review of this thesis. I really appreciate his efforts and time for reviewing my work.

Last but not least, I would like to thank all my colleagues of the Thermodynamics Department. The great working atmosphere led to a lot of joy and fun at work. The intensive communication and willingness to work together as a team and learn from each other meant a lot to me. Special thanks go to DI Lukas Albrecht Dür for the countless constructive discussions on the topic of compressors and design of experiments, as well as for proofreading this thesis.

KURZFASSUNG

Der Kältesektor hat einen Anteil von ca. 20 % am weltweiten elektrischen Energieverbrauch mit steigender Tendenz. In einem gewöhnlichen europäischen Haushalt zählen Kühl- und Gefriergeräte zu den größten Verbrauchern von elektrischer Energie. Während bisher hauptsächlich Kompressoren mit konstanter Drehzahl den Kältekreislauf von Haushaltskühl- und Gefriergeräten antreiben, ist bereits klar, dass die zukünftigen Anforderungen an die Energieeffizienz nur mit drehzahlvariablen Kompressoren erreicht werden können. Drehzahlvariable Kompressoren sind mit dem gleichen Ventilkonzept ausgestattet wie Kompressoren mit konstanter Drehzahl, was häufig zu einer unzureichenden Ventildynamik führt. Die Ventildynamik ist aber entscheidend für die Effizienz, die Kälteleistung, die Zuverlässigkeit und die Akustik dieser Kompressoren. Insbesondere bei drehzahlvariablen Kompressoren erfordert eine weitere Verbesserung der Ventildynamik die Berücksichtigung neuer Ventilkonzepte.

In der vorliegenden Arbeit wurde ein neues und kostengünstiges Ventilkonzept, das mechanisch unterstützte Saugventil (MASV), an einem hermetischen Kolbenverdichter untersucht. Dafür wurde zu Beginn ein internes Kompressor-Simulationsmodell entsprechend erweitert und mit Messdaten validiert. Anschließend erfolgte die Erstellung von Metamodellen unter Verwendung von Design of Experiments (DOE) Methoden. Mit Hilfe dieser Metamodelle, die den Zusammenhang zwischen Design Faktoren und entscheidenden Qualitätskriterien beschreiben, wurde dann eine systematische Design Optimierung in Bezug auf Energieeffizienz (COP), Kälteleistung, Zuverlässigkeit und Akustik mittels eines Multi-Response-Optimierungsansatzes durchgeführt. Darüber hinaus erfolgten umfangreiche Messungen, um das MASV hinsichtlich seiner tatsächlichen Verbesserungen bei verschiedenen Betriebsbedingungen experimentell zu untersuchen.

Mit der optimierten Design-Variante wurden COP-Verbesserungen bis zu 3,6 % und Kälteleistungsverbesserungen bis zu 6 % experimentell ermittelt, wobei höhere Kompressordrehzahlen tendenziell bessere Ergebnisse erzielten als niedrigere Drehzahlen. Es zeigte sich auch, dass Ventilschließverzögerungen und die damit verbundene Gasrückströmung bei hohen Kompressordrehzahlen besonders kritisch sind. Simulationsergebnisse bei 5000 U/min zeigten, dass durch ein MASV die Ventilschließverzögerung verringert und damit die Ansaugmasse um bis zu 22 % erhöht wird. Darüber hinaus führt die Vermeidung zwischenzeitlicher Ventilaufschläge sowie eine deutliche Reduktion der Ventilaufschlaggeschwindigkeit zu einer Reduktion der Ventilbelastung und somit zu einer höheren Zuverlässigkeit des Kompressors. Akustische Untersuchungen in einem Hallraum ergaben bei niedrigen Kompressordrehzahlen zum Teil eine Erhöhung des Schallleistungspegels, was auf die Bewegung der mechanischen Ventilunterstützung zurückzuführen ist und höchstwahrscheinlich ihren Ursprung in den Lagerstellen hat. Vibrationsmessungen ergaben keine grundsätzlichen Änderungen bei Verwendung des MASV. Die Sauggaspulsation hingegen konnte deutlich reduziert werden.

Nicht nur aus technischer, sondern auch aus wirtschaftlicher Sicht scheint das MASV angesichts der Einfachheit des Konzepts und der damit erzielbaren Vorteile machbar. Die weltweite Anwendung des MASV in allen zukünftigen Kompressoren für Haushaltskühlgeräte würde schätzungsweise zu einer jährlichen Stromeinsparung von 2,7 TWh - 5,5 TWh führen,

was beispielsweise 3,8 % - 7,6 % des jährlichen Stromverbrauchs von Österreich im Jahr 2019 entspricht.

ABSTRACT

The refrigeration sector holds approximately 20 % of the global electrical energy consumption and is expected to grow further. An analysis of the electrical energy consumption in a common European household indicates that refrigeration appliances are among the largest electricity consumers. While up to now, mainly fixed-speed compressors have been used to drive the refrigeration system of domestic refrigeration appliances, it has already become clear that future energy efficiency saving requirements in domestic refrigeration can only be achieved by means of variable-speed compressors. Variable-speed compressors are equipped with the same valve concept as fixed-speed compressors which often leads to insufficient valve dynamics. The valve dynamics of reed valves, which are widely used in compressors for domestic refrigeration, is crucial in terms of efficiency, cooling capacity, reliability and acoustics of the compressor. Especially in variable-speed compressors, a further improvement of the valve dynamics requires the consideration of a new valve concept.

In this work, a new and cost-effective concept of a mechanically assisted suction reed valve (MASV) is introduced. An in-house compressor simulation model was adopted to a 9.6 cm^3 hermetic reciprocating compressor to include the new MASV concept. After validation with measurement data, simulation-based surrogate models were created to systematically optimize the design in terms of energy efficiency (COP), cooling capacity, reliability and acoustics using a multi-response optimization approach. In addition, extensive measurements were carried out to experimentally investigate the MASV regarding its actual improvements at various operating conditions.

COP improvements up to 3.6 % and cooling capacity improvements up to 6 % were measured with one of the optimized design variants, whereby higher compressor speeds tend to achieve better results than lower speeds. It turned out, that valve closing delays and the associated gas backflow is particularly critical at high compressor speeds. Simulation results at 5000 rpm showed that the optimal design variant is capable of increasing the suction mass up to 22 % by reducing the valve closing delay. In addition, fewer intermediate valve impacts and a substantial reduction in valve impact velocity reduce valve stress and thus increase the reliability of the compressor. Acoustic measurements in a reverberation room indicated some increase in the sound power level at low compressor speeds which could be attributed to the motion of the MASV mechanism and most likely has its origin in the bearing points. Vibration measurements indicated no fundamental changes when using the MASV. In contrast, the suction gas pulsation was significantly reduced.

Not only technically, but also from an economic point of view, the MASV seems feasible given the simplicity of the concept and the benefits that can be achieved with it. The global use of the MASV in all future domestic refrigeration compressors could lead to global annual electricity savings of about 2.7 TWh - 5.5 TWh, which would be equivalent to 3.8% - 7.6 % of Austria's total electricity consumption in 2019.

TABLE OF CONTENTS

LIST OF FIGURES

LIST OF TABLES

NOMENCLATURE

Roman letters

a	–	number of factor levels of factor A
A	mm	factor rod diameter
A_{eff}	m^2	effective flow area
b	–	number of factor levels of factor B
B	mm	factor actuation amplitude
c	$\mathrm{N\ m^{-1}}$	stiffness
c	$\mathrm{m\ s^{-1}}$	speed of sound
C	°ca	factor actuation phase angle shift
COP	–	coefficient of performance
d	$\mathrm{kg\ s^{-1}}$	damping
d	–	desirability value
d	m	diameter
D	–	overall desirability
D	mm	factor spiral spring offset
E	$\mathrm{N\ mm^{-1}}$	factor spiral spring stiffness
f	Hz	frequency
F	N	force
F	mm	factor suction hole diameter
f_0	Hz	first natural frequency
f_1	–	degrees of freedom of the factor
f_2	–	degrees of freedom of the error
f_{l}	Hz	lower passband limit
f_{m}	Hz	centre frequency
f_{u}	Hz	upper passband limit
G	g	factor suction valve equivalent mass
h	$\mathrm{J\ kg^{-1}}$	specific enthalpy
H	$\mathrm{N\ mm^{-1}}$	factor suction valve stiffness
I	$\mathrm{W\ m^{-2}}$	sound intensity
I	N	factor suction valve preload force
J	mm	factor discharge valve lift
k	–	number of factors
k	–	number of individual desirability values
K	°ca	factor discharge valve closure after tdc
L	rpm	factor compressor speed
L_p	dB	sound pressure level
L_v	dB	particle velocity level
L_w	dB	sound power level
m	kg	mass
$\dot{m}$	$\mathrm{kg\ s^{-1}}$	mass flow
M	°C	factor operating condition
n	–	number of responses
n	–	number of runs
n	–	number of replicates

n_{C}	–	number of centre runs
n_{comp}	rpm, s^{-1}	compressor speed
n_{F}	–	number of factorial runs
p	–	fraction number
p	–	number of model parameters
p	Pa	pressure
P	W	power
$\dot{Q}_0$	W	cooling capacity
q_0	J kg^{-1}	energy per unit mass
R	J $(kg\ K)^{-1}$	specific gas constant
R^2	–	coefficient of determination
s	J $(Kg\ K)^{-1}$	specific entropy
S	m^2	surface
s_{c}	–	contact switch
t	s	time
T	K, °C	temperature
v	$m^3\ kg^{-1}$	specific volume
v	m s^{-1}	velocity
V	m^3	volume
w	J kg^{-1}	specific work
W	J	work
x	–	factor level
x	m	coordinate
$\boldsymbol{X}(t)$	[m, m, m, m s^{-1}, m s^{-1}, m s^{-1}]	state vector of multi-body system
y	J, kg, m s^{-1}	response
y	m	coordinate
Δf	Hz	bandwidth
$\Delta x_{23,0}$	m	distance offset
$\tilde{p}$	Pa	effective sound pressure
$\tilde{p}_0$	Pa	reference sound pressure
$\tilde{v}$	m s^{-1}	effective particle velocity
$\tilde{v}_0$	m s^{-1}	reference particle velocity

Greek letters

α	–	distance of star points from the centre
β	–	model parameter
ε	–	random error
η	–	efficiency
κ	–	isentropic exponent (specific heat ratio)
μ	–	overall mean effect
μ	–	flow coefficient
ξ		natural factor level
π	–	mathematical constant
ρ	kg m^{-3}	density

σ	–	area ratio
σ^2	–	variance
τ	–	factor effect
χ	–	coded factor level

Operators and designations

d	total differential
∂	partial differential
Π	product
$\sum$	sum
Δ	difference operator
$\dot{}$	first time derivative
$\ddot{}$	second time derivative

Further indices and abbreviations

0d	zero-dimensional
1d	one-dimensional
3d	three-dimensional
act	actuation
adj	adjusted
amb	ambient
ANOVA	analysis of variance
ASHRAE	American society of heating, refrigerating and air-conditioning engineers
BBD	Box-Behnken design
bdc	bottom dead centre
c	contact
ca	crank angle
CAD	computer-aided design
CCD	central composite design
CFD	computational fluid dynamics
comp	compressor
cond	condensing
d	damping
d	downstream
DES	differential equation system
df	degree of freedom
dis	discharge
displ	displacement
DOE	design of experiments
DSD	definitive screening design
el	electrical
equ	equivalent
err	error
evap	evaporating

FD	factorial design
FEM	finite element method
FFD	fractional factorial design
FS	full scale
FSI	fluid-structure interaction
H_0	null hypotheses
H_1	alternative hypotheses
HXK95	hermetic reciprocating compressor type
i	matrix index
i	indicated
IHX	internal heat exchanger
imp	impact
is	isentropic
j	matrix index
LBP	low back pressure
LDV	laser Doppler vibrometer
log	common logarithm with base 10 ($\log_{10}$)
m	mechanical
MASV	mechanically assisted suction reed valve
max	maximum
MBP	medium back pressure
min	minimum
n	nominal
OFAT	one factor at a time
p	pico (10^{-12})
PB	Plackett-Burmann
r	desirability function exponent
R134a	1,1,1,2-tetrafluoroethane (refrigerant)
R600a	isobutane (refrigerant)
ref	refrigerant
RMS	root mean square
rpm	revolutions per minute
RSD	response surface design
samp	sampling
SS	sum of squares
std	standard
sub	subcooling
suc	suction
sup	superheating
sv	suction valve
tdc	top dead centre
th	theoretical
tot	total
u	upstream
v	valve
var	variante
vol	volumetric

1 Introduction

1.1 Motivation

According to [32] the refrigeration sector holds approximately 20 % of the global electrical energy consumption. The total number of refrigeration, air conditioning and heat pump systems in operation worldwide is around 5 billion units, with domestic refrigeration appliances (refrigerators and freezers) alone accounting for 2 billion units [32]. The whole sector is expected to grow further due to global warming, growing world population and increasing prosperity particularly in emerging economies. Fig 1 shows a worldwide market forecast for domestic refrigeration appliances. It indicates a continuous growth in volume except for a small decrease in 2020 due to the Corona pandemic.

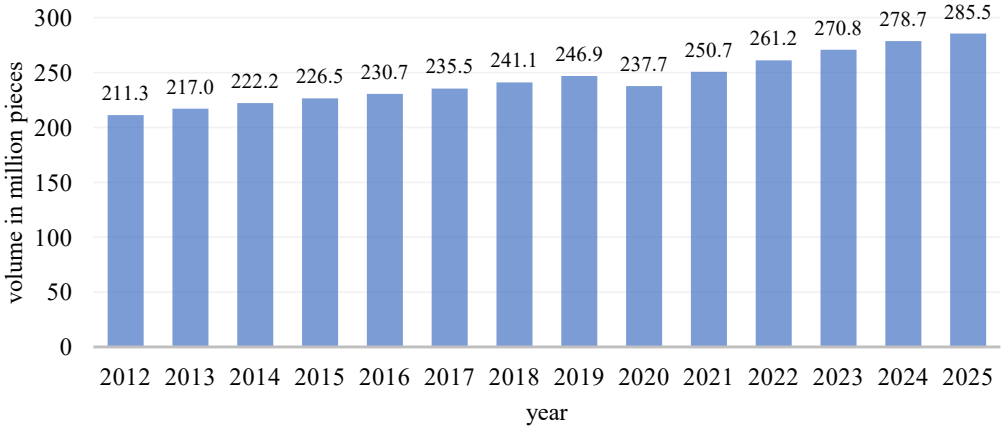

Fig. 1: Market forecast for domestic refrigeration appliances (refrigerators and freezers) worldwide [54, 55].

An analysis of the electrical energy consumption per sector in a common European household indicates that refrigeration appliances are among the largest electricity consumers, see Fig. 2.

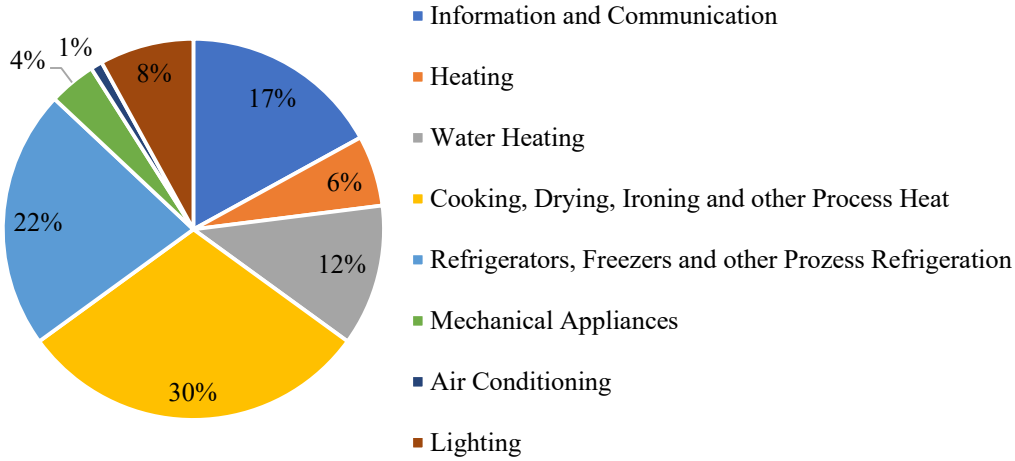

Fig. 2: Domestic electrical energy consumption per sector in Germany 2018 [9].

Most of this electrical energy is still currently produced by burning fossil fuels, which is associated with the emission of the greenhouse gas carbon dioxide. Making domestic refrigeration systems more energy efficient would thus have a considerable influence on the reduction of the anthropogenic greenhouse effect and thereby help to meet the Paris Agreement

from 2016 [61] to limit the global temperature rise well below 2 °C.

In order to further improve the energy efficiency of domestic refrigeration appliances and to accelerate the market orientation towards energy-efficient technologies, EU regulation no. 1060/2010 [24] on energy labelling of domestic refrigeration appliances was introduced. The regulation involves a labelling strategy, where refrigeration appliances are classified in energy efficiency classes from A+++ (highest efficiency) to G (lowest efficiency). This regulation has already been replaced by the regulation 2019/2016 [25] which applies from 1st March, 2021. It includes revised requirements for energy labelling to further reduce energy consumption.

The scale for energy labelling is now only from A (highest efficiency) to G (lowest efficiency), see Fig. 3, whereby the energy consumption limits of the individual classes are further reduced. This should lead to a reduction of the annual energy consumption of refrigeration appliances of approximately 10TWh by 2030 [25].

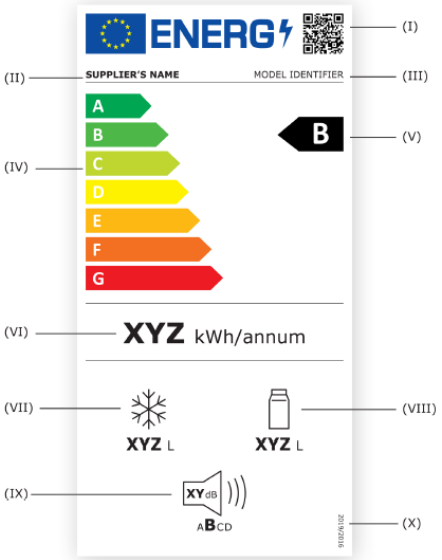

Fig. 3: New energy label for refrigeration appliances [25].

There are several approaches for improving the efficiency of refrigeration appliances, such as a larger heat exchanger area, top-mounted condensing coils, vacuum insulated panels, improved gasket seals, adaptive defrost and anti-sweat heaters, direct-current fan motors, separate compressors for fresh food and freezer storage, improved compressor efficiency and variable-speed compressors. However, no single refrigerator currently utilizes all of these approaches [38].

While up to now, mainly fixed-speed compressors have been used to drive the refrigeration system, it has already become clear that future energy efficiency requirements in domestic refrigeration can only be achieved by means of variable-speed compressors. While fixed-speed compressors are switched on and off, variable-speed compressors can adopt their speed to maintain a certain compartment temperature in a refrigeration appliance. This leads to a better match between required and delivered cooling capacity of the system, avoiding losses associated with the start/stop process and overperformance. However, variable-speed compressors still face challenges concerning the valve dynamics.

1.2 Literature Review and Problem Statement

Reed valves are widely used to control in- and outflow of the cylinder in hermetic reciprocating compressors for domestic refrigeration. They are characterised by a simple and inexpensive design and by their automatic adaption to different operating conditions as they are pressure actuated only. Reed valves are crucial components in terms of efficiency, cooling capacity, acoustics and reliability of the compressor.

Numerous studies based on experimental or numerical methods have been carried out to investigate and improve the behaviour of reed valves in reciprocating compressors. [44] used a strain gauge to measure the dynamic behaviour of a suction valve. [47] experimentally determined the p-V diagram and the valve motion simultaneously in order to obtain a better understanding of the valve losses. Other authors investigated the influence of different design and operation parameters on valve dynamics [16, 26, 35], backflow rates [58] or valve failure [43, 64]. [65] and [46] investigated the influence of oil on the valve dynamics and [40] experimentally investigated the effect of valve damping on efficiency and valve impact velocity.

The results of the studies mentioned above indicate that the main causes of thermodynamic and volumetric losses are valve opening delays due to oil sticking and inertia effects as well as intermediate valve closings, often referred as valve flutter, and valve closing delays. The suction reed valve in particular shows a high flutter intensity, since the suction phase requires almost half a revolution of the crank shaft. [10] conducted a sensitivity analysis of different suction valve parameters using a 1d compressor model. They emphasized the importance of reduced valve flutter for the reduction of valve losses. [15] analysed the influence of the main reed valve parameters on the performance of the compressor by means of a spring-damper-mass system model with one degree-of-freedom. They investigated the potential of a theoretical valve without valve flutter and found that the suction power consumption decreased by 36 % leading to a COP increase of 2 %.

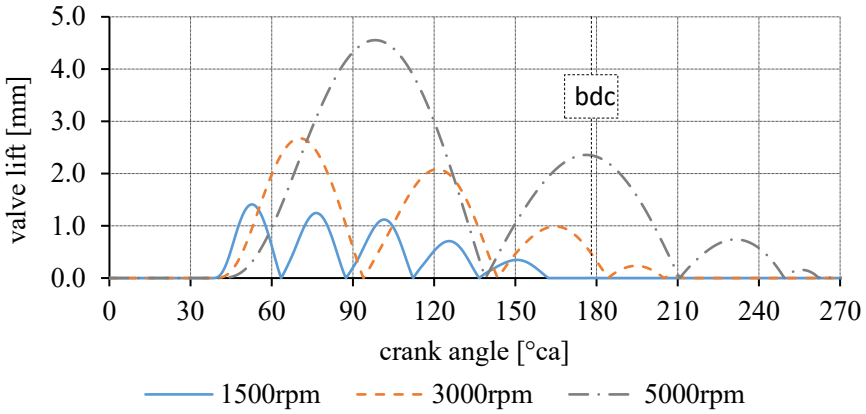

Fig. 4: Conventional suction reed valve motion at different compressor speeds.

While reed valves already cause a significant proportion of the thermodynamic losses in fixed-speed compressors, it is even worse in variable-speed compressors. In variable-speed operation, the suction and discharge time varies with the compressor speed while the valve flutter frequency remains constant [57, 62, 63]. This may reduce the volumetric efficiency due to gas

backflow caused by valve closing delays [44, 58]. Unlike the discharge valve, the suction valve lift is not limited by a stopper. Thus, increasing compressor speed leads to increasing valve lifts and higher valve impact velocities which may cause serious reliability issues. Fig. 4 shows the valve lift related to the crank angle of a conventional suction reed valve at different compressor speeds.

The optimization of a conventional reed valve is limited to a few parameters such as geometrical parameters (length, width and thickness) and material properties (steel type etc.). Some system characteristics, e.g., valve flutter or delayed valve closing in variable-speed compressors, cannot be avoided with the conventional reed valve concept. A further improvement of the valve dynamics requires the consideration of new valve concepts.

An ideal suction valve opens immediately from zero to maximal valve lift once pressure equalisation between upstream and downstream side of the valve occurs. It remains at maximal valve lift during the entire suction phase and finally closes immediately as soon as back-flow begins. Fig. 5 shows the COP and cooling capacity improvement potential as a function of the compressor speed. The difference between ΔCOP (ideal suction valve) and ΔCOP (no suction work) is that throttling effects still occur when the ideal suction valve is passed through, whereas no suction work means that the entire suction process is loss-free. Depending on the compressor speed, the theoretical COP improvement potential of an ideal suction reed valve is between 2 % and 4 %. In addition, the potential for improving cooling capacity at high compressor speeds is substantial since backflow is avoided.

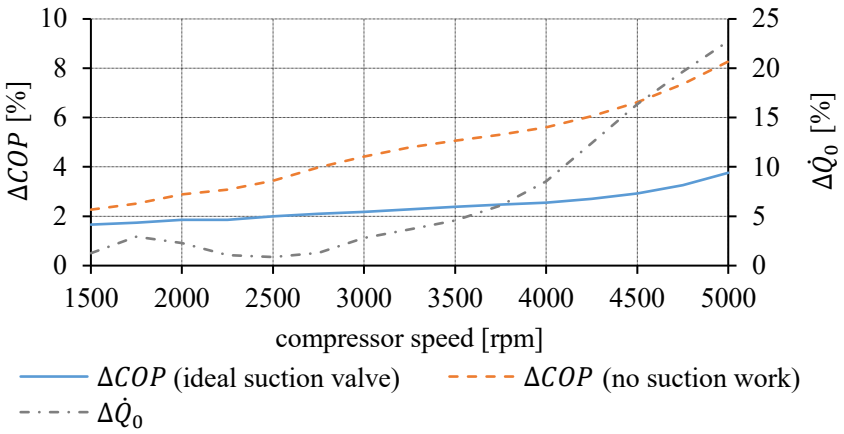

Fig. 5: Theoretical *COP* and cooling capacity improvement potential as a function of the compressor speed of an ideal suction valve[1].

A first attempt towards an ideal suction reed valve was made by [30]. They studied the reduction of the suction losses using a suction valve with a negative preload force in combination with an electromagnetic coil. Calorimeter measurements showed a COP improvement potential of up to 1.7 %. However, the COP improvement was strongly influenced by the operating condition

[1] Simulation results based on in-house compressor simulation model described in section 3.2, calculation of ΔCOP according to equation 17.

and the energy consumption of the electromagnetic coil was not considered in the calculation.

[22] investigated a mechanically assisted suction reed valve to improve the efficiency and overcome the challenges of variable-speed operation. An important constraint was that the automatic adaptation of the valve control to different operating conditions must be maintained. Preliminary experimental investigations indicated a favourable behaviour of the valve dynamics and calorimeter measurements at different operating conditions showed an average COP improvement of 1.9 %. However, the investigated concept is too costly and, therefore, not suitable for an application in domestic refrigeration.

1.3 Research Question

The question arises whether there is an alternative, more cost-effective concept of a mechanically assisted suction reed valve. If so, what is the optimal design factor setting to improve the COP, cooling capacity and reliability of the compressor simultaneously? In the low to medium compressor speed range, efficiency is of particular importance, while at high speeds it is important to provide sufficient cooling capacity. It is important to know how a mechanically assisted suction reed valve contributes to those compressor speed dependent demands.

Thus, the following research questions are addressed in this thesis:

1. How can an alternative and cost-effective concept of a mechanically assisted suction reed valve look like?
2. How does a hermetic reciprocating compressor equipped with a mechanically assisted suction reed valve behave over a wide range of compressor speed in terms of efficiency, colling performance, reliability and acoustics?
3. What is the optimal design variant to improve the efficiency, cooling capacity, reliability and acoustics of the compressor simultaneously and which quantitative improvements can be achieved?

1.4 Mechanically Assisted Suction Reed Valve (MASV)

Reed valves are widely used to control the in- and outflow of compression gas in the cylinder of hermetic reciprocating compressors. They are characterised by a simple and inexpensive design, as they essentially consist of a single metal sheet that opens and closes automatically depending on the pressure difference. As described in section 1.2, reed valves are crucial components in terms of efficiency, cooling capacity, acoustics and reliability of the compressor.

An ideal reed valve opens immediately to maximal valve lift as soon as pressure equalisation between upstream and downstream side of the valve occurs. It remains at maximal valve lift during the entire in- or outflow phase and finally closes immediately as soon as pressure equalisation is reached again. Conventional reed valves, however, are far from showing this ideal valve behaviour.

Reed valves are usually preloaded, i.e., they are pressed onto the valve seat when closed in order to achieve sufficient sealing. In addition, the closing force increases with increasing valve opening due to the spring effect. Together with oil sticking and inertia effects, this results in an actual valve motion characterised by opening delays, intermittent valve closing and closing delays. The associated increase in suction work reduces the energy efficiency of the compressor. In addition to energy efficiency, the valve motion also influences the acoustic

properties and reliability of the compressor. The oscillating valve causes noise and mechanical load when it hits the valve seat, especially if the impact velocity is high. An additional source of noise is the gas pulsation due to the discontinuous flow, particularly when delayed valve opening leads to greater pressure differences between the cylinder and the muffler.

To further improve the valve dynamics and acoustics of hermetic reciprocating compressors, alternative valve concepts must be considered. One option could be the forced movement of the valve through mechanical, hydromechanical or electrical drives. However, this principle is linked to a high control effort (sensors, etc.) to account for different valve timings at different operating conditions. Since only a low-cost solution is conceivable for the type of compressor under consideration, this principle will not lead to a viable solution.

An alternative to the forced valve movement could be to only support the valve through an additional force. This supporting force could help to improve the valve dynamics of reed valves while maintaining automatic adaptation to different operating conditions. The valve support can basically be divided into three phases with different requirements, i.e., valve opening phase, keep valve open phase and valve closing phase.

In the opening phase, the supporting force should compensate for oil sticking and inertia effects to achieve faster opening of the valve. Premature opening due to too high forces must be avoided. In the second phase, the supporting force should serve to keep the valve open, while in the third and final phase, the aim is to support the valve during the closing process in order to achieve timely closing and low impact velocities. Thus, the supporting force must be variable in time.

In principle, the supporting force can be generated mechanically, hydromechanically or electrically. Above all, the two aspects of costs and integrability led to the decision to pursue the mechanical generation of the supporting force.

Compared to the discharge valve, the suction valve has a higher oscillation intensity because the valve lift is not limited by a stopper. In addition, the suction valve is more critical in terms of reliability, as the impact velocities and thus the loads are very high. For this reason, the underlying work is dedicated to search for a suitable suction valve support mechanism.

Fig. 6 shows a proposed solution for a mechanically assisted suction reed valve (MASV). The MASV mechanism basically consists of a grooved disc fixed to the crank shaft, a lever and a spring element attached to the lever. A bearing pin at one end of the lever slides in an eccentric circular groove producing a sinusoidal motion of the spring element in valve opening direction. Magnitude and timing of the supporting force can be influenced through the spring stiffness, the leverage ratio and the groove design. A preliminary investigation of this concept can be found in [22]. Experimental results indicated a favourable behaviour of the valve dynamics and calorimeter measurements at different operating conditions showed an average COP improvement of 1.9 %. However, the lever-based design is too expensive related to the COP improvement potential. In addition, the mechanical losses produced by the groove actuation might be further reduced as the friction path per revolution is large. Thus, an alternative, more cost-effective concept of a MASV needs to be found.

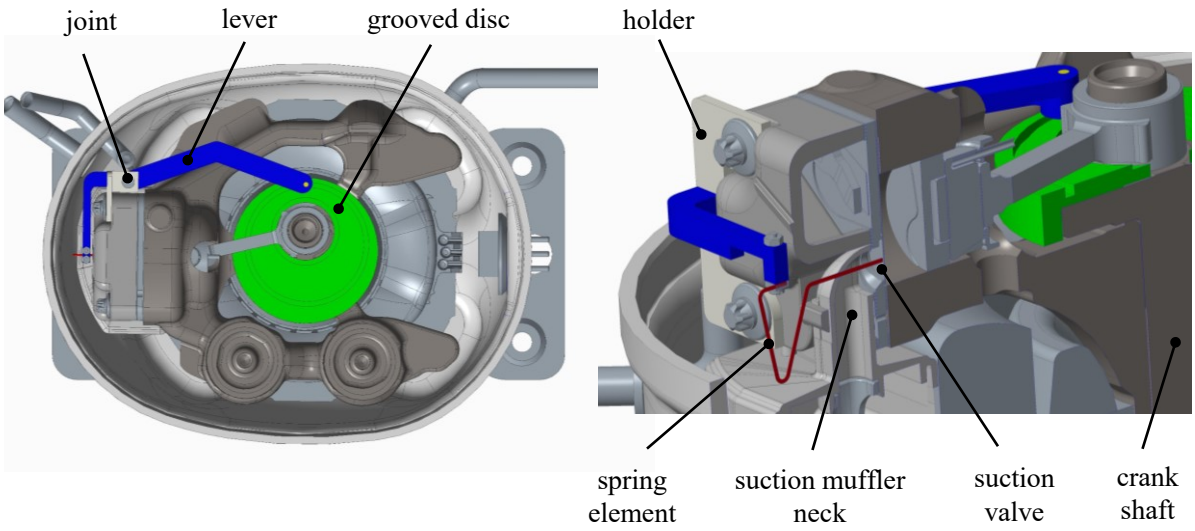

Fig. 6: Hermetic reciprocating compressor equipped with a MASV mechanism [22].

A very simple alternative concept of a MASV is shown in Fig. 7. The core idea of this concept is to realise the transmission of the actuation from the crank shaft to the valve and the generation of the supporting force via a single component. A cam disc which is fixed to the crank shaft elastically deforms a pivoted rod causing the right end of the rod to move towards the suction valve and applying the supporting force. The magnitude and timing of the supporting force mainly depends on the cam shape and the stiffness of the rod. Preloading the rod against a friction plate would result in additional damping of the suction valve oscillation.

Transient 3d-FEM analyses were carried out to preliminary investigate the valve dynamics. As a first approximation, the differential pressure between both sides of the valve was applied through a pressure boundary condition, which was previously determined using the in-house compressor simulation model described in [1]. Oil sticking forces were not considered in these preliminary investigations.

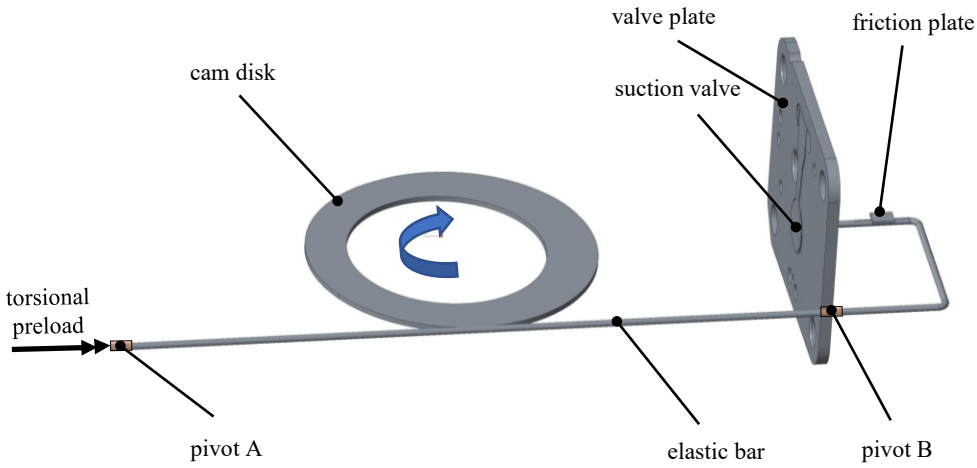

Fig. 7: MASV based on a cam disk with an elastic rod.

Fig. 8 and Fig. 9 show the results of the preliminary 3d-FEM analyses. The duration of the valve oscillation is very long compared to the suction phase, see Fig. 8. The rod design is restricted by the arrangement of the crank shaft and the suction valve. The required stiffness of

the rod is very low compared to the required dimension. This results in a long oscillation duration and a high inertia of the system. Especially at higher compressor speeds, this can lead to significant valve closing delays. By modifying the cam shape and using a friction plate, valve oscillation can be significantly reduced, see Fig. 8. However, this additional friction is associated with an increase in mechanical losses, which affects the overall efficiency of the compressor.

Another drawback of this concept is that, due to the kinematics, the right end of the rod does not perform a purely translatory movement in valve opening direction. Thus, the bore diameter in the suction muffler neck must be significantly larger than the rod diameter, leading to thermodynamic losses and acoustic problems.

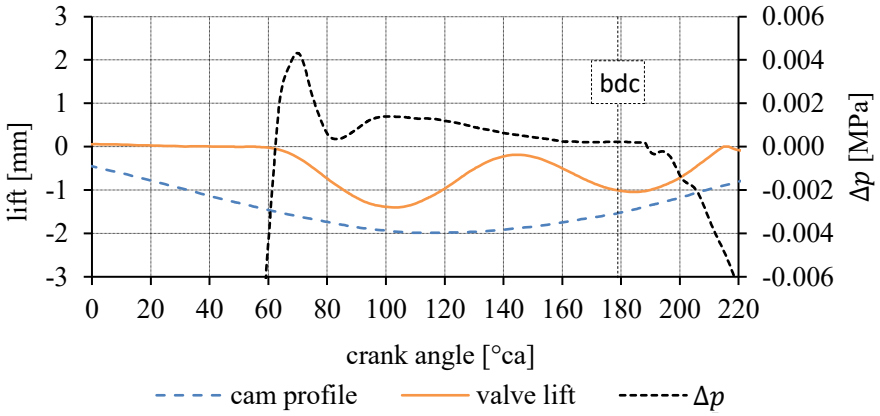

Fig. 8: Preliminary FEM investigation of MASV based on a cam disk and an elastic rod excluding the friction plate (compressor speed = 3000 rpm, rod diameter = 1.25 mm).

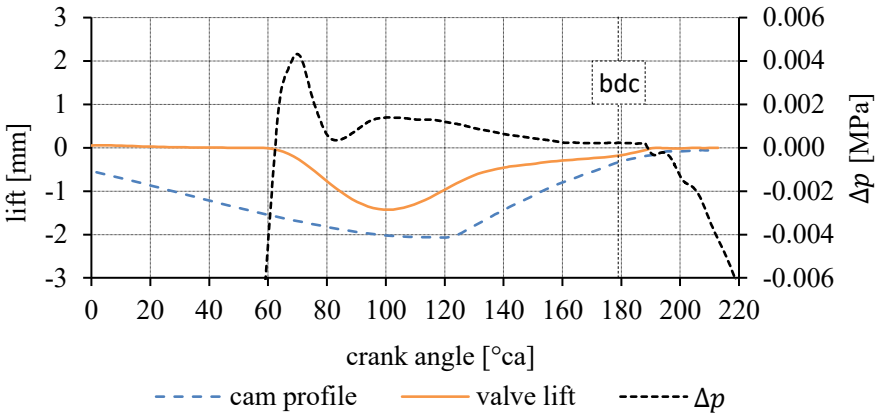

Fig. 9: Preliminary FEM investigation of MASV based on a cam disk and an elastic rod including the friction plate (compressor speed = 3000rpm, rod diameter = 1.25 mm, torsional preload angle = 10 °, friction coefficient = 0.1).

Based on the findings of the above concepts, a further MASV concept was developed. The two tasks of motion transmission and force generation are carried out by two separate components to increase the dynamic performance of the MASV. Fig. 10 shows the proposed mechanism of a cost-effective MASV concept that will be further investigated within this thesis. The

mechanism is assembled to a small hermetic reciprocating compressor for domestic refrigeration as described in section 2.2.1. The assembly consists of a mechanical actuation unit, a connection rod and a spiral spring. The actuation unit drives the connection rod through an eccentric bore and thus leads to a sinusoidal motion of the spiral spring in valve opening direction. The compression of the spiral spring generates a variable force on the surface of the suction valve which is supposed to improve the valve dynamics.

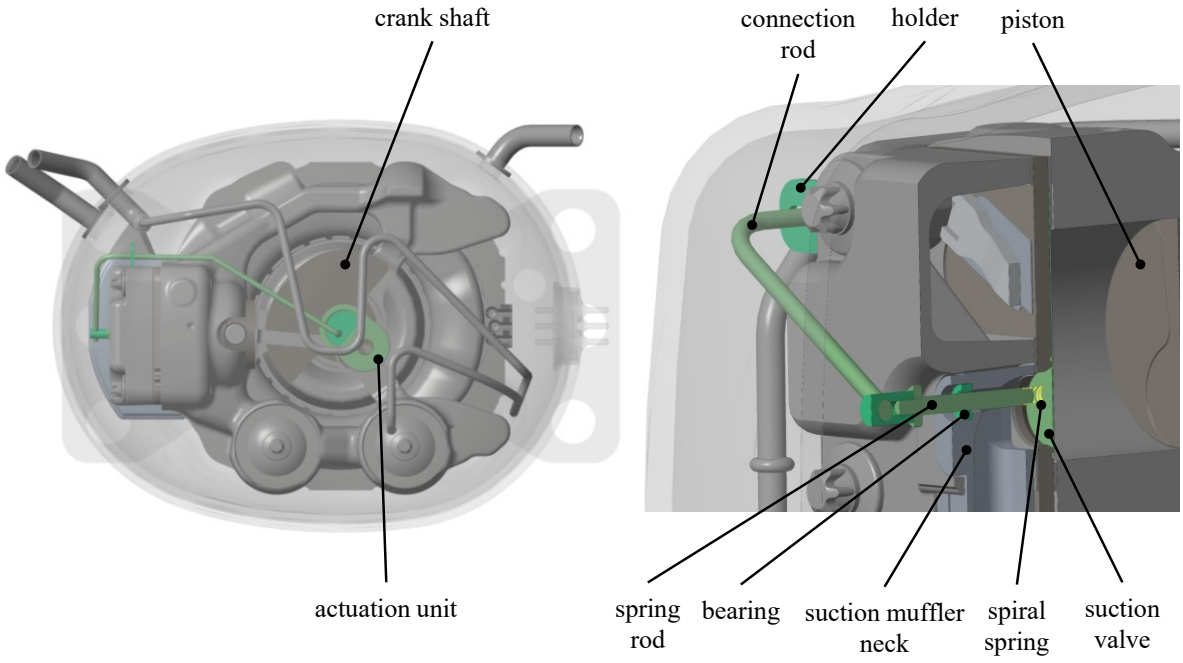

Fig. 10: Proposed concept of a mechanically assisted suction reed valve (MASV).

Important design parameters are the actuation amplitude, actuation phase angle shift, spiral spring stiffness and the distance offset between the spiral spring and suction valve. The illustrated design of the mechanism allows for adjusting these important design parameters. Once the optimal design parameters have been determined, the mechanism can be further simplified, e.g., to combine connection rod and spring rod, or to design the actuation unit as one simple flap which is fixed to the crank pin.

2 Theoretical Background

2.1 Domestic Refrigeration

There are many systems which involve different variants of a refrigeration plant. Since this thesis is focused on the hermetic reciprocating compressor for domestic refrigeration, the following section describes the refrigeration plant which is commonly used for domestic refrigeration appliances i.e. refrigerators and freezers.

The refrigeration plant of most domestic refrigeration appliances is based on the vapor compression cycle in which a refrigerant, mostly R134a or R600a, undergoes phase changes [5]. In its simplest form, a refrigeration plant consists at least of the four components evaporator, condenser, expansion device and compressor. The schematic in Fig. 11 shows the main components of the refrigeration plant of domestic refrigeration appliances. The numbers refer to the state points in the underlying vapor compression cycle, illustrated in Fig. 14.

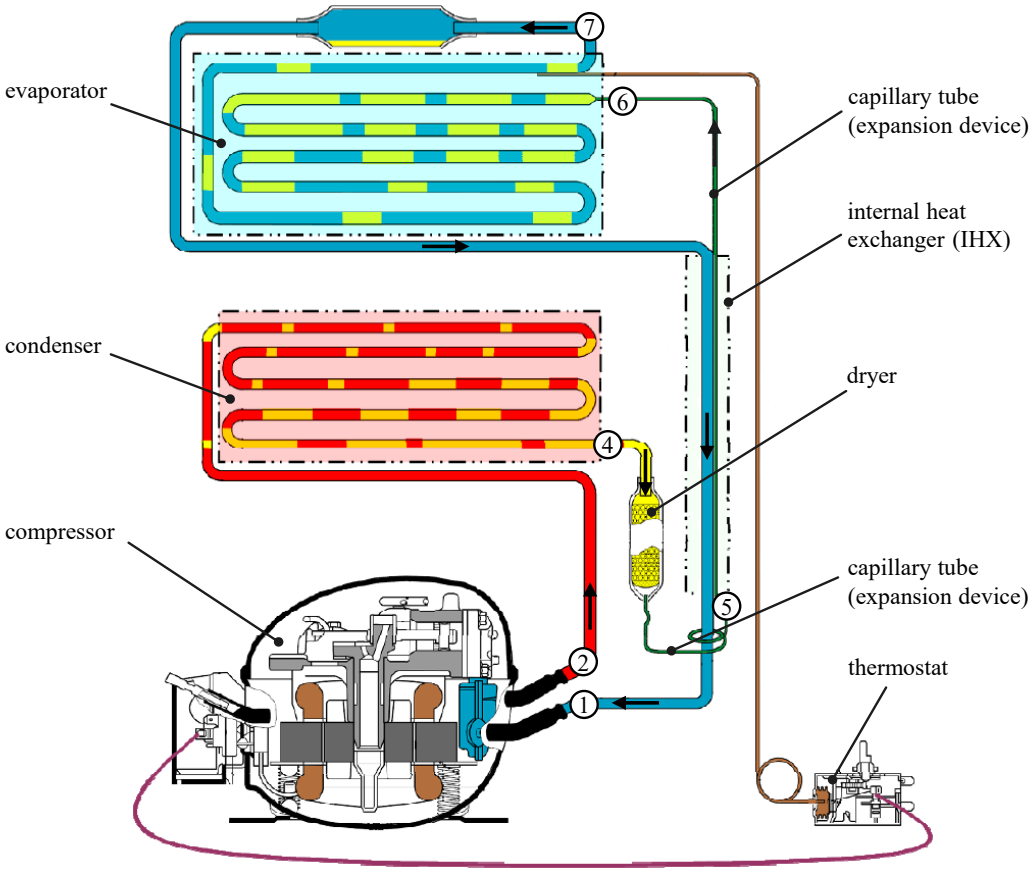

Fig. 11: Schematic of a refrigeration plant for domestic refrigeration [14].

2.1.1 Main Components

Compressor

In domestic refrigeration, mostly a hermetic reciprocating compressor is used to drive the refrigeration plant. It lifts the pressure of the refrigerant from evaporating pressure to condensing pressure level. Up to now, mainly fixed-speed compressors with on/off-control are used in domestic refrigeration. A thermostat measures the temperature inside the refrigerator. If the temperature is too high, the compressor is switched on and starts the refrigeration plant. When the desired cooling temperature is reached, the compressor and thus the refrigeration plant is switched off again. Modern refrigerators increasingly use variable-speed compressors to improve the energy efficiency by better matching the supplied cooling capacity with the required one. A detailed description of the hermetic reciprocating compressor is given in section 2.2.

Condenser

The refrigerant leaves the compressor at high pressure and high temperature levels and flows through the condenser where heat is rejected to the ambient air. The condenser is usually located either on the rear wall or in the base of the refrigeration appliance, leading to heat transfer based on natural or forced convection.

Expansion device (capillary tube)

An expansion device expands the liquid refrigerant coming from the condenser back to the evaporating pressure level. In domestic refrigeration, the expansion device is usually designed as a capillary tube which is basically a long tube of small diameter.

Mostly an internal heat exchanger is part of the refrigeration plant since the compressor is very sensitive to the suction of liquid refrigerant. Small droplets within the refrigerant steam can cause serious damage to the compressor. The first section of the capillary tube is thereby attached to the outlet section of the evaporator forming a counterflow heat exchanger. The internal heat exchanger transfers heat from the hot liquid refrigerant in the capillary tube to the suction gas, leading to subcooled refrigerant at the high-pressure side and superheated refrigerant at the low-pressure side of the refrigeration plant. Subcooling increases the amount of heat that can be absorbed by the evaporator, thus increasing the cooling capacity and efficiency of the refrigeration plant, while the superheating ensures that no wet steam enters the compressor. A more detailed description of the capillary tube is given in [29].

Evaporator

The evaporator extracts heat from the compartment, which is why it is usually built into the wall of the refrigeration appliance. Due to a temperature difference between the compartment and the evaporator, a heat flux is established in the direction of the evaporator which cools the compartment and simultaneously evaporates refrigerant in the evaporator.

2.1.2 Vapor Compression Cycle

Carnot cycle

The Carnot cycle is a theoretical, ideal thermodynamic cycle to convert work into heat or vice versa at maximum efficiency, see Fig. 12. The Carnot cycle consists of two isothermal (heat input from 4 to 1 and heat output from 2 to 3) and two isentropic (compression from 1 to 2 and expansion from 3 to 4) state changes.

The efficiency of an energy conversion can always be described as the quotient of benefit and effort. In refrigeration, the efficiency is often referred as coefficient of performance COP, which is generally defined as

$$COP = \frac{\text{useful refrigerating effect}}{\text{net energy supplied from external sources}} \quad (1)$$

where in a mechanical vapor compression cycle the net energy is supplied as mechanical or electrical work [4].

Taking into account the first law of thermodynamics, the COP of the Carnot cycle is calculated according to equation 2. The lower the temperature difference between the condensing temperature T_{cond} and the evaporating temperature T_{evap}, the higher the COP. However, the condensing temperature level is restricted to the ambient room temperature of the refrigeration appliance, while the evaporating temperature is restricted to the desired compartment temperature. Typical operating conditions for specifying the COP in domestic refrigeration are $T_{\mathrm{evap}} = -23.3$ °C and $T_{\mathrm{cond}} = 54.4$ °C as well as $T_{\mathrm{evap}} = -23.3$ °C and $T_{\mathrm{cond}} = 45$ °C. The former leads to a COP_{Carnot} of 3.22, the latter to 3.66.

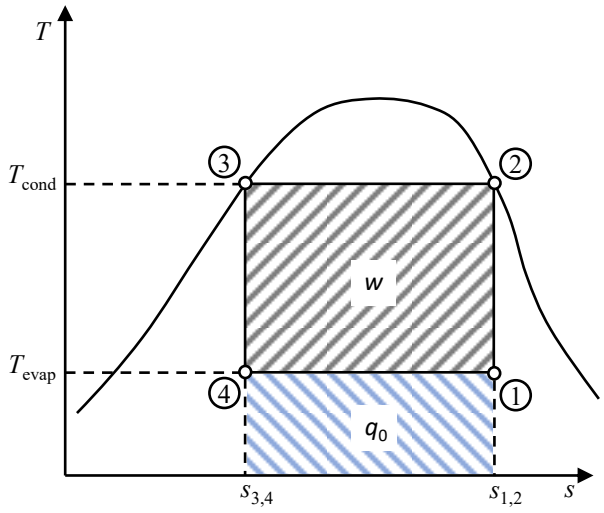

Fig. 12: Carnot cycle.

$$COP_{\mathrm{Carnot}} = \frac{T_{\mathrm{evap}}}{T_{\mathrm{cond}} - T_{\mathrm{evap}}} \quad (2)$$

Evans-Perkins cycle

Due to concerns about high initial costs and maintenance requirements, actual refrigeration systems do not include an expander (motor or turbine), but use a simple expansion valve or capillary tube that throttles the refrigerant from high to low pressure instead. The Evans-Perkins cycle is, therefore, a more suitable ideal vapor compression cycle, see Fig. 13. It consists of isentropic compression (1 - 2), isobaric cooling (2 - 3), isenthalpic expansion (3 - 4) and isobaric evaporation (4 - 1). In contrast to the Carnot cycle, the Evans-Perkins cycle does not allow to recover the expansion energy.

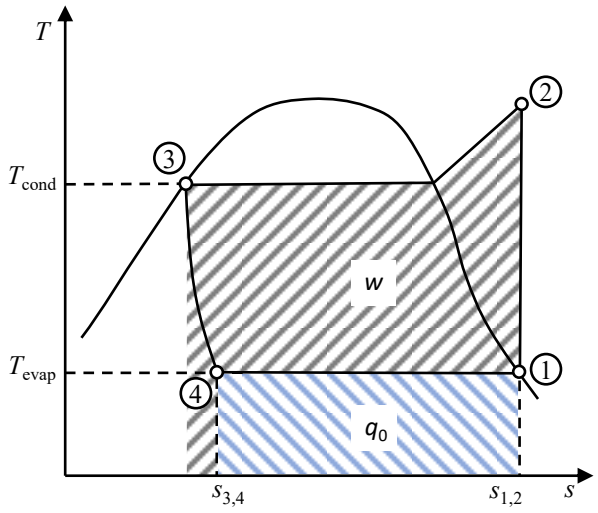

Fig. 13: Evans-Perkins cycle

The Evans-Perkins cycle does not allow to give a medium-independent formulation of the COP. The COP of the Evans-Perkins cycle is calculated according to equation 3.

$$COP_{\text{Evans-Perkins}} = \frac{q_0}{w} = \frac{h_1 - h_4}{h_2 - h_1} \qquad (3)$$

where q_0 corresponds to the usable energy per unit mass in the evaporator and w refers to the indicated compression work per unit mass.

ASHRAE cycle

The ASHRAE standard 23.1 [3] describes testing methods for performance rating of refrigerant compressors used for domestic refrigeration. Fig. 14 shows the ASRAE cycle in a Ts diagram for the refrigerant isobutane (R600a). Compared to the Evans-Perkins cycle, both isobaric superheating and isobaric subcooling of the refrigerant take place. The typical ASHRAE rating condition is composed of − 23.3 °C (− 10 °F) evaporating temperature, 54.4 °C (130 °F) condensing temperature, and 32.2 °C (90 °F) ambient temperature, with suction gas superheated and liquid subcooled to 32.2 °C (90 °F). In a further frequently used rating condition, the condensing temperature is set to 45 °C.

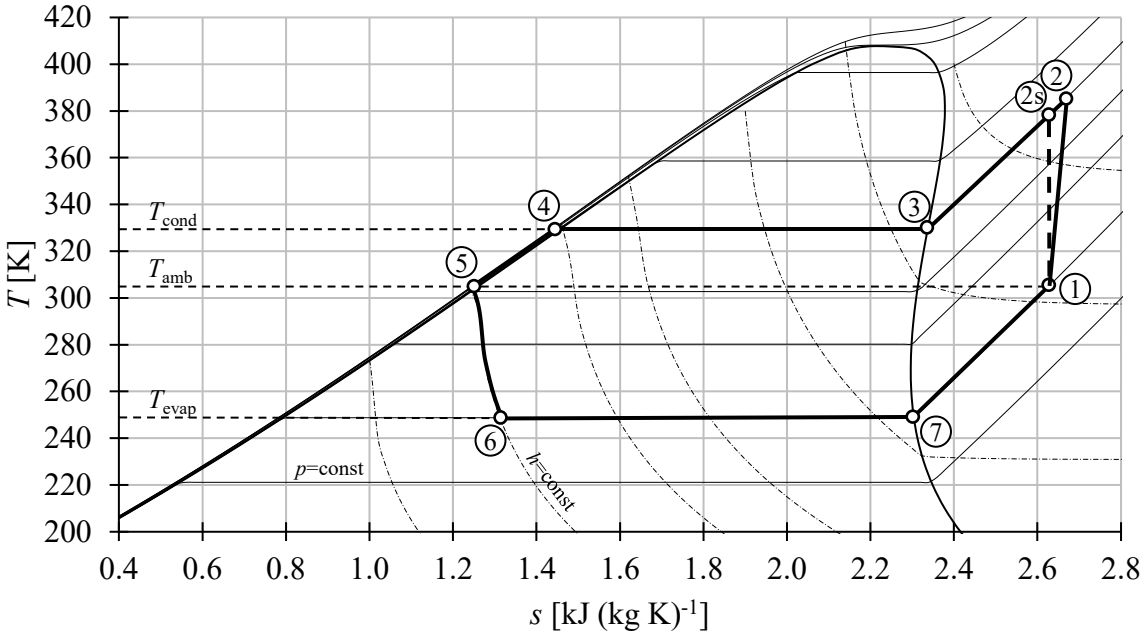

Fig. 14: ASHRAE cycle [3] for isobutane (R600a) at T_{evap} = − 23.3 °C, T_{cond} = 54.4 °C and $T_{amb} = T_{sub} = T_{sup}$ = 32.2 °C.

The theoretical COP of the ASHRAE-cycle is calculated according to equation 4.

$$COP_{th} = \frac{h_1 - h_6}{h_{2s} - h_1} = \frac{q_0}{w_{is,comp}} \quad (4)$$

where $w_{is,comp}$ refers to the compression work per unit mass assuming isentropic compression. By definition, the amount of heat required for superheating is counted to q_0. For R600a with T_{evap} / T_{cond} of − 23.3 °C / 54.4 °C and − 23.3 °C / 45 °C respectively, this results in a COP_{th} of 2.40 and 2.90.

Actual cycle

The Ts diagram in Fig. 15 schematically shows an actual vapor compression cycle of a cooling appliance, neglecting pressure drops in the components. Prior to the compression, the refrigerant is heated up due to hot surfaces in the suction line and the cylinder. With increasing compression, the refrigerant temperature exceeds the surface temperature of the cylinder, leading to a reverse heat flux and thus bending the compression line to the left. After completion of compression, the refrigerant is further cooled in the downstream discharge line of the compressor.

A refrigeration appliance mostly includes an internal heat exchanger (IHX). The amount of energy per unit mass which is transferred from the hot liquid to the cold suction gas is illustrated as hatched area below the lines 5 - 5’ and 7 - 1. Thus, the usable energy per unit mass in the evaporator can be increased from 6 to 6’. Although the use of an IHX leads to higher compression start temperature and thus to a higher compression work per unit mass, it usually increases the COP because the increasing energy per unit mass in the evaporator outweighs the increasing compression work per unit mass.

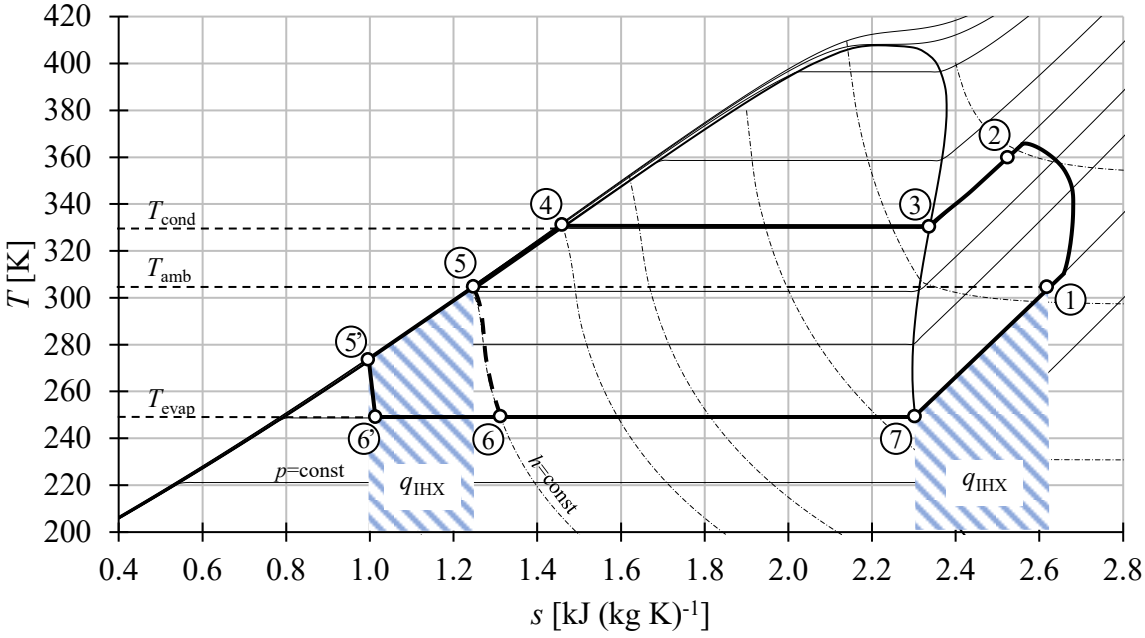

Fig. 15: Actual vapor compression cycle for isobutane (R600a) with and without an internal heat exchanger (IHX) at $T_{evap} = -23.3$ °C, $T_{cond} = 54.4$ °C and $T_{amb} = T_{sub} = T_{sup} = 32.2$ °C. Pressure drops in the components are neglected.

Finally, it should be mentioned, that for a holistic determination of the efficiency of a refrigeration appliance, additional electrical consumers such as light, user interface or fans for forced convection in the evaporator and condenser must be included. In addition, the ASHRAE cycle describes a stationary operating condition of the refrigeration system. In order to adapt the cooling capacity to the actual cooling demand of the cooling appliance, the compressor is usually operated via a simple on-off control or, more recently, via speed control. In reality, the refrigeration appliance therefore never reaches stationary operating conditions. For that reason, different test procedures are required to rate the performance of refrigeration appliances, which may vary from region to region. The common procedure for Europe is described in the standard ICE 62552 [31]. However, since this thesis focuses on investigations on the refrigerant compressor, these procedures will not be further explained.

2.2 Hermetic Reciprocating Compressor

As mentioned in section 2.1.1, the compressor is one of the four main components of a vapor compression cycle, beside the evaporator, condenser and expansion device. In general, compressors can be divided in two different categories: positive displacement and dynamic compressors. Positive-displacement compressors increase the pressure by reducing the volume of a compression chamber while dynamic compressors continuously transfer kinetic energy into pressure based on rotating components. Positive-displacement compressors include many different types, such as rotary (e.g. rolling piston, rotary vane, screw), orbital (e.g. scroll) and reciprocating compressors. Depending on the application, different aspects like physical size, noise, efficiency, costs, capacity, etc. influence the selection of a specific compressor type [6].

Vapor compression cycles in domestic refrigeration are almost exclusively driven by hermetic reciprocating compressors. This section describes the design, function and loss mechanisms of a hermetic reciprocating compressor in more detail.

2.2.1 Kappa Compressor (HXK95)

The design and functional principle of a hermetic reciprocating compressor is explained using the Kappa compressor (HXK95) of the European compressor manufacturer Secop GmbH, as all investigations of this work were carried out on this compressor platform. However, the basic design of hermetic reciprocating compressors hardly differs from manufacturer to manufacturer and has remained unchanged over many decades.

Fig. 16 shows the flow schematics of the HXK95 compressor. The low-pressure gas enters the compressor at the suction inlet, where it flows through the suction line into the cylinder. After compression in the cylinder system, the high-pressure gas flows through the discharge line to the discharge outlet and leaves the compressor. Due to the sequential operation of the reciprocating compressor and the associated discontinuous flow, see also section 2.2.2, undesirable pressure pulsations occur in the suction and discharge line. These pressure pulsations may affect the volumetric efficiency, vibration and noise level of the compressor. Large volumes in suction and discharge line help to reduce these pressure pulsations. A CAD drawing of the HXK95 is given in Fig. 17. The corresponding key-data are summarized in Table 1.

A special design aspect of the hermetic reciprocating compressor is that the electric motor and the compressor itself are installed in the same housing, called shell. The top and bottom part of the steel shell are welded together, making it hermetically sealed. The reason for the hermetic design is that one central requirement of the refrigeration plant and its components is to be maintenance-free. The refrigerant must not leak out of the system over the entire lifetime of typically 15 to 20 years. In addition, if a flammable refrigerant is used, leakage would be a serious safety hazard.

The rotation axis of the single-phase asynchronous motor is vertically aligned, whereby the rotor is fixed to the crank shaft and the stator is fixed to the crank case. The crank case is connected to the shell via four suspension springs in order to absorb vibration. The mechanical power coming from the motor is transferred to the refrigerant via a crank drive which is composed of the three main components crank shaft, connecting rod and piston. The crank shaft also contains the oil pump of the compressor. The oil collected in the bottom of the shell (oil

sump) is transported upwards through a combination of centrifugal and helical pump sections inside the crank shaft. It delivers oil to the crank shaft bearings and finally splashes toward piston and shell wall through the top edge of the crank shaft. The pumped oil not only serves to reduce friction in the individual bearing and contact points, but also takes over a large part of the heat transfer in the compressor. A more detailed description concerning the thermodynamic influence of the lubrication oil in hermetic reciprocating compressors is given in [56].

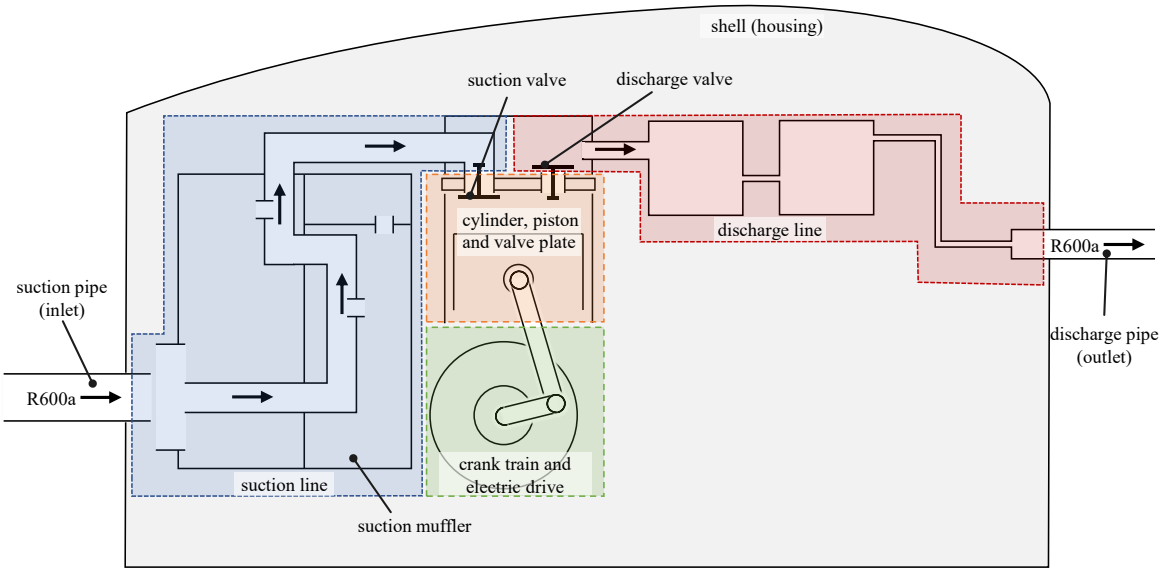

Fig. 16: Flow schematics of HXK95 compressor.

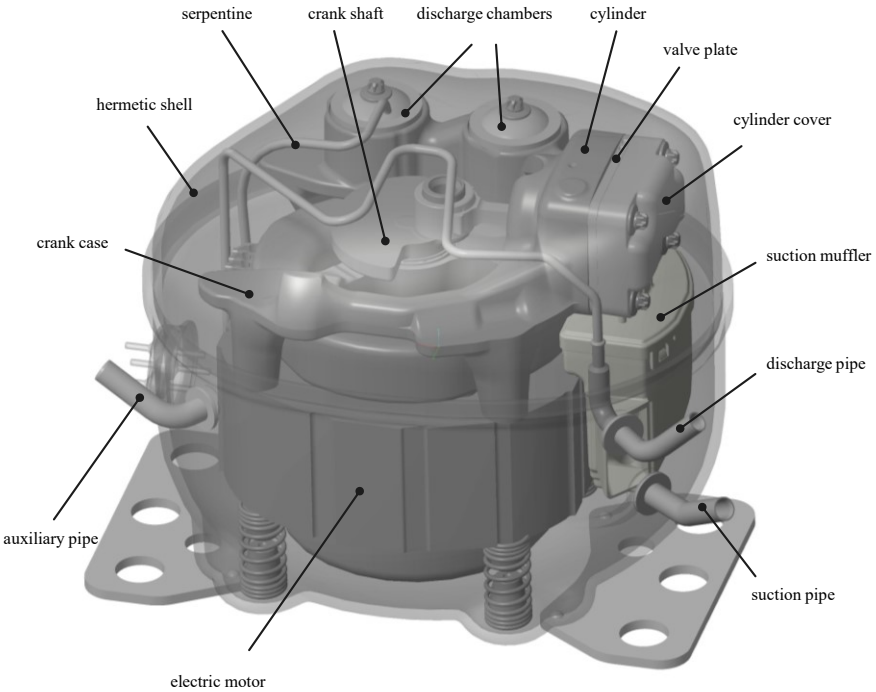

Fig. 17: CAD of HXK95 compressor.

Table 1: Key-data HXK95 compressor.

parameter	unit	value
cylinder diameter	mm	25.4
connecting rod length	mm	47
piston stroke	mm	19
displacement	cm^3	9.6
refrigerant	-	R600a
frequency	Hz	50/60
nominal power input[2]	W	89.5
nominal cooling capacity[2]	W	171
COP[2]	-	1.91

Suction line

The suction line consists of the suction pipe and the suction muffler, see Fig. 18. The suction pipe forms the interface to the refrigeration plant of the refrigeration appliance. The purpose of the suction muffler is to guide the suction gas from the suction pipe (inlet) to the cylinder and to dampen noise transmitted through the suction line. Important design requirements of the suction muffler are: minimum pressure loss, minimum suction gas superheating and sufficient gas pulsation damping.

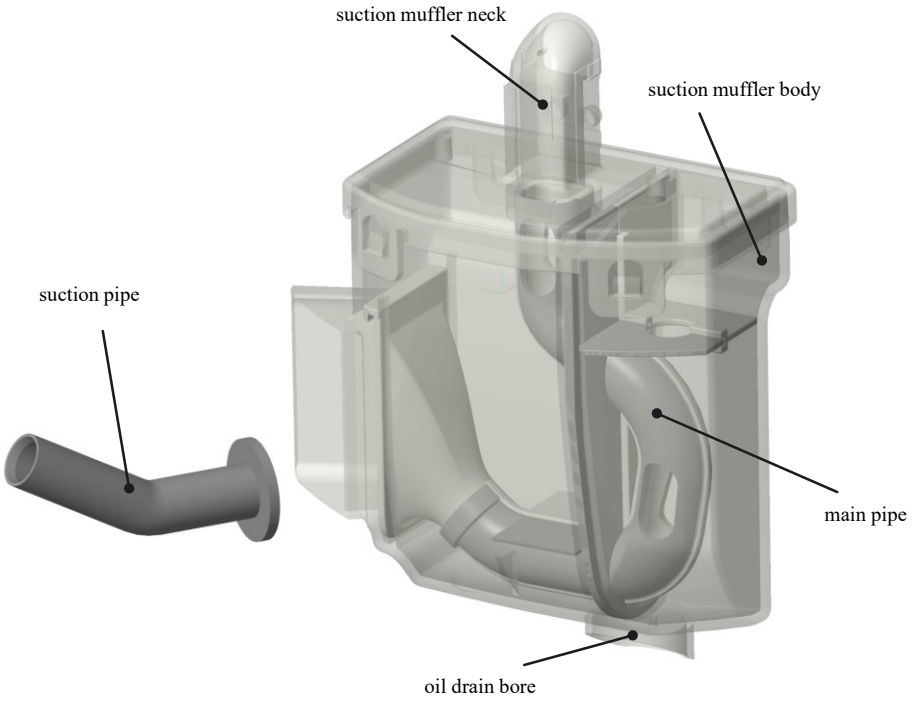

Fig. 18: Suction line.

[2] ASHRAE-cycle [3] at T_{evap} = -23.3 °C, T_{cond} = 54.4 °C, T_{amb} = T_{sub} = T_{sup} = 32.2 °C, f=50 Hz [51].

The suction muffler is made of plastic and consists of one main pipe with connections to several chambers of different size, leading to noise damping based on the Helmholtz resonator principle. An oil drain hole in the bottom of the muffler ensures that the chambers do not fill with separated lubrication oil.

There is no direct connection between the suction pipe (inlet) and the suction muffler, which means that the entire shell volume is connected to the suction line. This indirect connection offers acoustic advantages, but also leads to higher suction gas temperatures and thus to a lower efficiency compared to a direct connection. The last section of the suction muffler, also called neck, is connected to the suction port of the valve plate. The neck design influences the suction valve dynamics such as valve impact velocity and valve timing.

Cylinder, piston and valve plate

Cylinder, piston and the valve plate form the compression chamber of the compressor, see Fig. 19. The cylinder consists of cast iron and includes the cylinder bore, the crank shaft bearing seat and parts of the discharge line. Cylinder and piston are paired to reach an optimal balance between leakage and friction. The cylinder clearance volume has a significant effect on the cooling capacity and efficiency of the compressor. Therefore, the piston design includes a piston nose and a recess of the suction valve contour to reduce the cylinder clearance to a minimum. In addition, to counteract production tolerances, different cylinder gasket thickness classes allow a further distance reduction between the piston top and the valve plate.

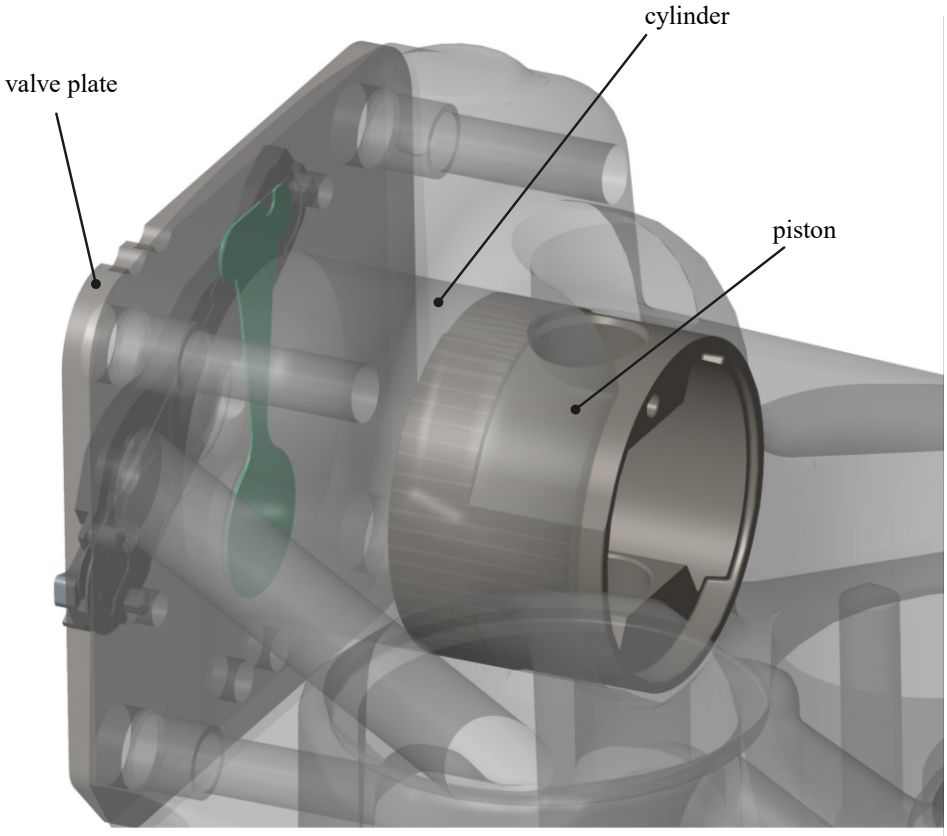

Fig. 19: Cylinder, piston, valve plate.

The valve plate is attached to the cylinder via the cylinder cover and four screws. It includes the suction and discharge valve system, see Fig. 20. Reed valves are used to control the flow in and out of the cylinder. They open and close automatically by the pressure difference between suction line and cylinder (suction valve) or between cylinder and discharge line (discharge valve). Reed valves are crucial compressor components in terms of efficiency, cooling capacity, noise and reliability.

The suction valve system consists of a simple spring-steel sheet of 0.203 mm thickness. When assembled, it is clamped via the valve plate and the cylinder at the outer end of the valve. The discharge valve system consists of three components: bracket, damper and discharge valve. Unlike the suction valve, the discharge valve lift is limited by the bracket. The damper increases the valve stiffness above a certain valve lift and thus influences the valve dynamics. Damper and discharge valve are made of spring-steel sheet and have a thickness of 0.152 mm and 0.203 mm respectively. The valve seat of both, suction and discharge valve, must be designed in a way that minimizes oil sticking and leakage effects.

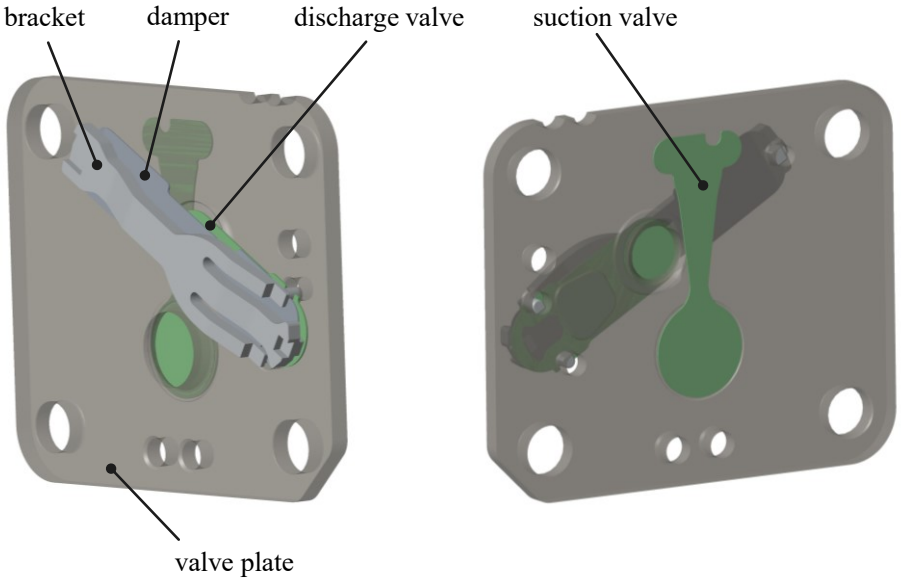

Fig. 20: Valve plate with suction and discharge valve system.

Discharge line

The discharge line, as illustrated in Fig. 21, consists of the cylinder cover, pressure chambers, connection channels, serpentine and the discharge pipe. As with the suction line, the discharge line combines the tasks of flow guidance and noise damping. Important design requirements are minimum pressure loss, minimum heat extraction from the hot discharge gas, minimum vibration transmission to the shell and maximal gas pulsation damping.

The discharge line is partly integrated in the crank case, which makes it cheaper on the one hand, but worsens the cooling of the cylinder on the other. The pressure chambers reduce the gas pulsation caused by the discontinuous flow. The serpentine connects the last pressure chamber to the discharge pipe (outlet). In contrast to suction pipe and suction muffler, a direct connection to the discharge pipe is required. To keep vibration transmissions at a minimum, the serpentine is designed as a long and flexible steel pipe. However, it increases pressure losses as well as heat transfer to the shell volume.

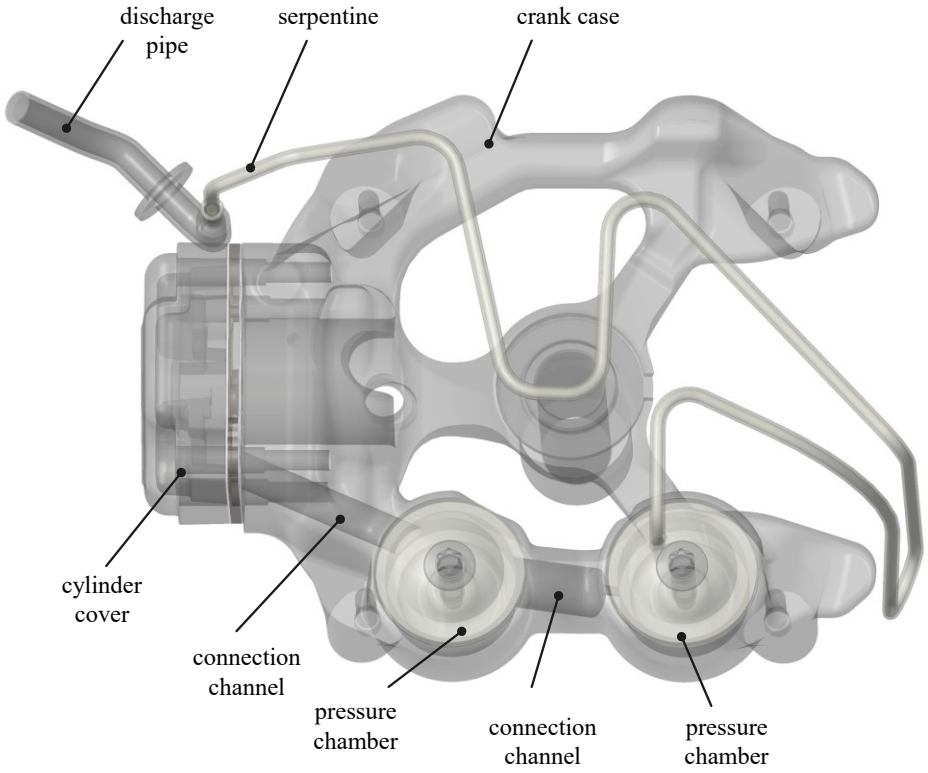

Fig. 21: Discharge line of HXK95.

2.2.2 Compressor Working Cycle

In general, the working cycle of a reciprocating compressor can be divided into three phases. First, the suction phase, where low pressure suction gas enters the cylinder through the suction valve. Second, the compression phase, where the actual compression of the gas from low to high pressure takes place. Third the discharge phase, where high pressure gas leaves the cylinder. Fig. 22 shows the working cycle of an ideal reciprocating compressor in a pV-diagram.

In an ideal working cycle, the following aspects apply:

1. The cylinder volume (clearance volume) is negligibly small when the piston is in the top dead centre (tdc).
2. During suction phase, the conditions in the cylinder are the same as the inlet conditions (no throttling by the suction valve).
3. The compression is frictionless.
4. During discharge phase, the conditions in the cylinder are the same as the outlet conditions (no throttling by the discharge valve).

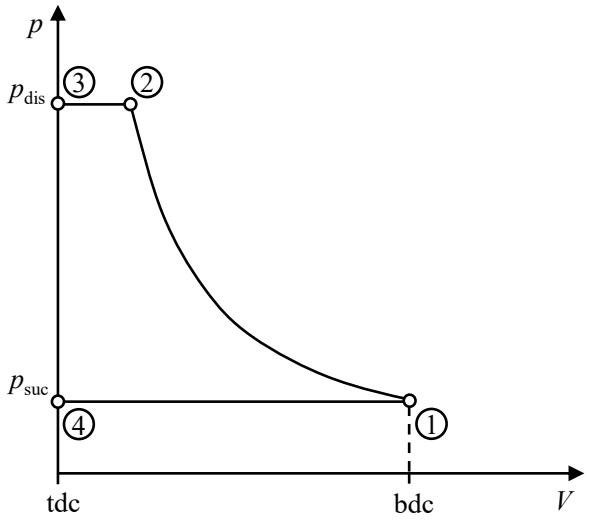

Fig. 22: Ideal working cycle of a reciprocating compressor [6].

If the compression is considered to be adiabatic, the ideal compression process, which requires a minimum of indicated work, would be isentropic. If the compression is considered to be diabatic, the ideal compression process would be isothermal. However, in a reciprocating refrigerant compressor, the isentropic compression process is usually considered as the ideal process.

The real working cycle, as illustrated in Fig. 23, differs from the ideal working cycle. Significant pressure losses occur during the suction and discharge phase, and the compression is not isentropic as a result of friction and heat transfer. Furthermore, re-expansion of compressed gas occurs prior to the suction phase due to a non-negligible clearance volume at tdc.

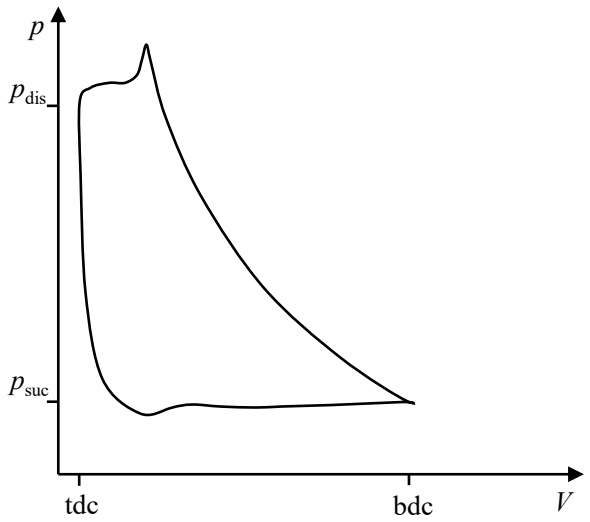

Fig. 23: Real working process.

For both, ideal and real working cycle, the indicated or induced compressor work per cycle can be expressed as the cycle integral of $p\mathrm{d}V$, see equation 5.

$$W_\mathrm{i} = \oint p\mathrm{d}V \qquad (5)$$

2.2.3 Compressor Losses and Efficiencies

Generally, three different categories of losses are distinguished in a reciprocating compressor: i) electrical losses of the electrical motor and its auxiliary components; ii) mechanical losses due to friction losses between piston and cylinder as well as in the bearings of the crank drive; iii) thermodynamic losses due to irreversibilities in the suction, compression and discharge process. Fig. 24a illustrates the breakdown of the three main loss categories of a household reciprocating compressor. The thermodynamic losses account for the largest share.

A further breakdown of those thermodynamic losses is shown in Fig. 24b. The suction gas superheating has the largest share in the thermodynamic losses. It occurs due to heat transfer from the hot wall to the suction gas in the suction line and cylinder. The consequence is a higher compression start temperature, which increases the compression work and reduces the cylinder charge and thus the refrigerant mass flow. A further large share in the thermodynamic losses are viscous losses in the suction and discharge line as well as in the valves.

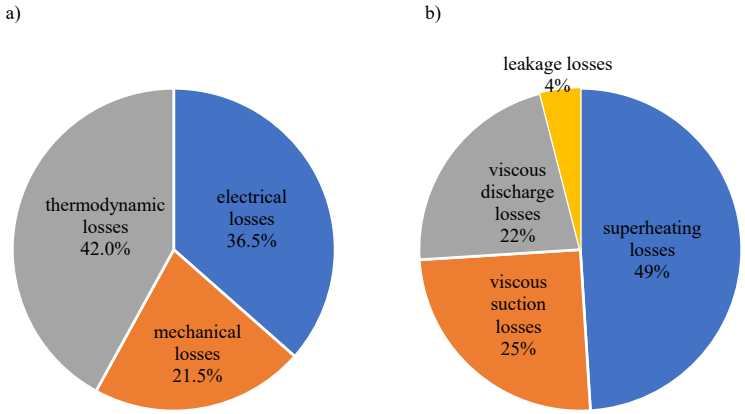

Fig. 24: General loss distribution a)[3] and detailed thermodynamic loss distribution b) in a household reciprocating compressor [48].

The total compressor efficiency η_comp is thus made up of an isentropic, mechanical and electrical component:

$$\eta_\mathrm{comp} = \eta_\mathrm{is}\,\eta_\mathrm{m}\,\eta_\mathrm{el} \qquad (6)$$

where the compression isentropic efficiency η_is is a measure of the deviation of the actual compression work W_i actually delivered to the gas from the isentropic compression work W_is and thus only considers what happens inside the compression chamber.

[3] general loss distribution was calculated based on an electrical efficiency of 88 %, a mechanical efficiency of 92 % and a thermodynamic efficiency of 83 % as published in [48].

$$\eta_{\mathrm{is}} = \frac{W_{\mathrm{is}}}{W_{\mathrm{i}}} \quad (7)$$

The mechanical efficiency η_{m} is defined as ratio of work delivered to the gas W_{i} to work input to the compressor shaft W_{m}.

$$\eta_{\mathrm{m}} = \frac{W_{\mathrm{i}}}{W_{\mathrm{m}}} \quad (8)$$

And the electrical efficiency is the ratio of work delivered to the compressor shaft W_{m} to the work delivered to the electrical motor W_{el}.

$$\eta_{\mathrm{el}} = \frac{W_{\mathrm{m}}}{W_{\mathrm{el}}} \quad (9)$$

Hence, the actual electrical power input of the compressor is related to the ideal, isentropic power input through the isentropic, mechanical and electrical efficiency.

$$P_{\mathrm{el}} = \frac{P_{\mathrm{m}}}{\eta_{\mathrm{el}}} = \frac{P_{\mathrm{i}}}{\eta_{\mathrm{m}}\,\eta_{\mathrm{el}}} = \frac{P_{\mathrm{is}}}{\eta_{\mathrm{is}}\,\eta_{\mathrm{m}}\,\eta_{\mathrm{el}}} \quad (10)$$

The cooling capacity $\dot{Q}_0$ can be expressed as the refrigerant mass flow $\dot{m}_{\mathrm{ref}}$ times the energy per unit mass in the evaporator q_0.

$$\dot{Q}_0 = \dot{m}_{\mathrm{ref}}\, q_0 \quad (11)$$

The ratio of actual to ideal refrigerant mass flow is defined as volumetric efficiency η_{vol}.

$$\eta_{\mathrm{vol}} = \frac{\dot{m}_{\mathrm{ref}}}{\dot{m}_{\mathrm{ref,ideal}}} \quad (12)$$

where the ideal refrigerant mass flow is calculated based on suction gas density, compressor displacement and compressor speed.

$$\dot{m}_{\mathrm{ref,ideal}} = \rho_{\mathrm{suc}}\, V_{\mathrm{displ}}\, n_{\mathrm{comp}} \quad (13)$$

In order to rate the performance of a refrigeration compressor, the actual COP is determined experimentally based on a standardized cycle e.g. ASHRAE cycle (see section 2.1.2) according to equation 14.

$$COP = \frac{\dot{Q}_0}{P_{\mathrm{el}}} \quad (14)$$

whereby the cooling capacity $\dot{Q}_0$ and the electrical compressor power P_{el} are usually measured with a calorimeter test bench, see section 2.3.

To assess the effect of a particular design change (variant) on the efficiency of the compressor,

the COP difference is related to the COP of the standard compressor according to equation 15.

$$\Delta COP = \frac{COP_{\mathrm{var}} - COP_{\mathrm{std}}}{COP_{\mathrm{std}}}\ 100\% \tag{15}$$

With

$$COP = \frac{\dot{Q}_0}{P_{\mathrm{el}}} = \frac{n_{\mathrm{comp}}\, Q_0}{n_{\mathrm{comp}} W_{\mathrm{el}}} = \frac{m_{\mathrm{ref}}\, q_0}{W_{\mathrm{i}}}\ \eta_{\mathrm{el}}\, \eta_{\mathrm{m}} \tag{16}$$

inserted into equation 15 and assuming that the electrical and mechanical efficiency does not change, the COP change can be written as follows:

$$\Delta COP = \left[\frac{m_{\mathrm{ref,var}}}{m_{\mathrm{ref,std}}}\ \frac{W_{\mathrm{i,std}}}{W_{\mathrm{i,var}}} - 1\right] 100\% \tag{17}$$

Thus, a positive change of the COP will only occur if the product of the two fractions is greater than one. Ideally, the mass discharged per working cycle is increased while at the same time the indicated compressor work is reduced.

2.3 Calorimeter Testbench

The Calorimeter is a laboratory apparatus to measure the performance of a refrigeration compressor at standardized and stationary operating conditions. Depending on the test standard (e.g. ASHRAE, see section 2.1.2), different values can be set for the ambient, evaporating, condensing, superheating and subcooling temperature. The calorimeter used in this work uses R600a as refrigerant, which is undergoing a classical vapor compression cycle. Fig. 25 shows the schematic of the calorimeter testbench.

The COP can be calculated based on the measurement results of the electrical compressor power and the cooling capacity of the evaporator. The electrical power consumption of the compressor is measured by a wattmeter. The cooling capacity is determined indirectly through a special approach. A calorimetric vessel contains a secondary fluid at two-phase condition and ambient temperature, where the evaporation of the R600a is carried out. Due to heat transfer from the vessel to the vapor compression cycle, the temperature and thus the pressure in the vessel would decrease. For that reason, an electrical heater keeps the vessel's pressure and temperature constant. The electrical power of the heater which corresponds to the cooling capacity, is measured by a wattmeter. Table 2 gives the main specifications of the calorimeter testbench.

Table 2: Main specifications of the calorimeter testbench.

type	secondary fluid calorimeter
manufacturer	Microline
complying standard	ASHRAE 23 [3]
refrigerant	R600a
max. cooling capacity	300W

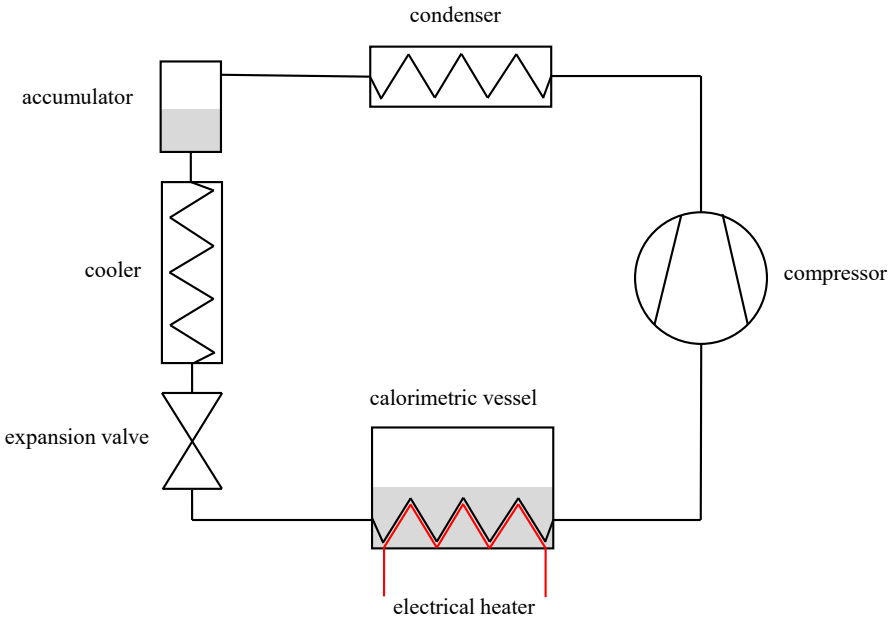

Fig. 25: Schematic of calorimeter testbench.

2.4 Acoustic Basics

This section provides some important acoustic basics from the literature, which served as foundation for the acoustic investigations in section 4. A more comprehensive treatment of acoustics in reciprocating compressors can be found in [53].

Sound refers to mechanical vibrations of elastically vibrating media such as air, liquids and solids. Vibrations in air and liquids are called airborne and liquid-borne sound, while vibrations in solids are called structure-borne sound. Sound is categorized according to its frequency range as listed in Table 3. Infrasound is particularly relevant for vibrations in solids, while ultrasound is used, for example, in medical technology and non-destructive material testing. The frequency range audible to humans extends from approximately 16 Hz to 16 kHz.

Table 3: Sound categories by frequency range [11].

sound category	frequency range
infrasound	< 16 Hz
audible sound	16 Hz – 16 kHz
ultrasound	16 kHz – 1 GHz
hypersound	> 1 GHz

2.4.1 Field Quantities

Field quantities are all mechanical quantities that characterize the disturbed state caused by a sound field. The two main field quantities to describe a sound field are sound pressure and sound velocity. Both are immission quantities, i.e. they characterize the sound field at a specific location.

Sound Pressure

A sound source causes the surrounding air to vibrate, which leads to very small pressure fluctuations that are superimposed on the atmospheric pressure. This small pressure fluctuation is called sound pressure p. Since the atmospheric pressure changes only very slowly compared to the sound pressure, it can be assumed to be constant. Fig. 26 shows the time course of the air pressure at a specific location in the sound field.

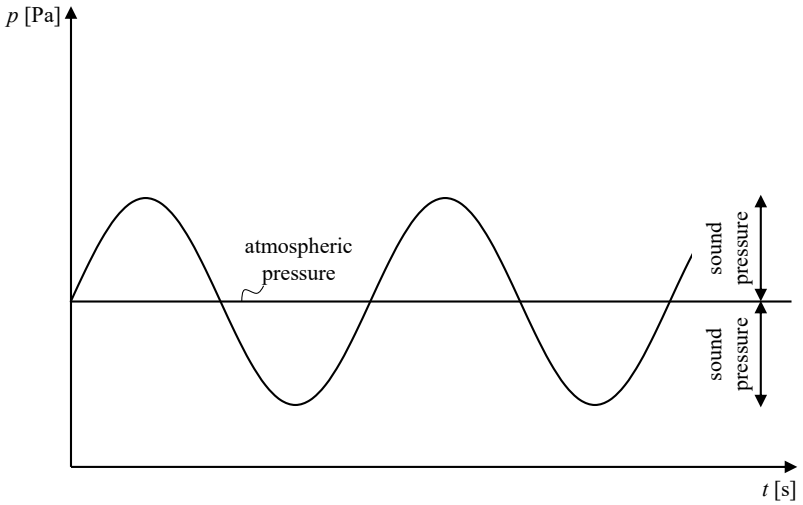

Fig. 26: Pressure fluctuations in sound field.

The sound pressure is usually given as an effective value (RMS). This effective value is obtained according to equation 18. In measuring instruments, the effective value is usually calculated over a period of seconds.

$$\tilde{p} = \sqrt{\frac{1}{T}\int_0^T p^2(t)\,\mathrm{d}t} \tag{18}$$

The effective sound pressure at normal conversation volume at a distance of 1 m from the speaker corresponds to about 10^{-1} Pa. The threshold of hearing is about 2×10^{-5} Pa, while the threshold of discomfort is about 10^2 Pa. [11]

The pressure fluctuations are directly linked to very small fluctuations in air temperature and air density. Like sound pressure, these very small temperature and density fluctuations are also undirected sound field variables. However, they are difficult to measure and therefore not used.

Particle Velocity

The local particle velocity v, not to be confused with the speed of sound c, is the speed at which the air particles move back and forth in a sound field. In calm air, the particle movement takes place around a rest position, and the particle velocity takes on positive and negative values. In moving air, the particle velocity caused by the sound field is superimposed on the mean flow velocity. In contrast to the sound pressure, the particle velocity is a directional field quantity, i.e. a vector. In a plane sound wave, the following relationship applies between the sound pressure p and the sound velocity v

$$p = \rho\, c\, v \tag{19}$$

where ρ corresponds to the density of the medium and c is the speed of sound. The product ρc is called impedance and is about 400 kg $m^{-2}s^{-1}$for air.

Analogous to the sound pressure, the effective value of the particle velocity is

$$\tilde{v} = \sqrt{\frac{1}{T}\int_0^T v^2(t)\,\mathrm{d}t} \tag{20}$$

2.4.2 Sound Intensity

The sound intensity I corresponds to the sound energy that passes through a unit of area per unit of time and has the dimension W m^{-2}. The intensity of a sound wave results from the product of the field quantities sound pressure and particle velocity

$$I = \frac{1}{T}\int_0^T p(t)\, v(t)\,\mathrm{d}t \tag{21}$$

Since the particle velocity is a directional quantity, the sound intensity is also a directional quantity. The following applies to the intensity in a plane sound wave

$$I = \tilde{p}\,\tilde{v} = \frac{\tilde{p}^2}{\rho c} = \rho\, c\, \tilde{v}^2 \tag{22}$$

2.4.3 Sound Power

The sound power indicates how much sound energy passes through a surface S in a unit of time. Sound power indicates the acoustic power emitted into the environment, e.g. by a machine. The sound power is therefore an emission quantity. The sound power P passing through the surface S results from the intensity I according to

$$P = \int_S I \,\mathrm{d}S \tag{23}$$

If the sound wave passes perpendicularly through the surface, equations 22 and 23 lead to

$$P = \frac{1}{\rho c}\int_S \tilde{p}^2 \,\mathrm{d}S \tag{24}$$

Equation 24 indicates that the sound power of the source can be calculated based on the sound pressure at a specific distance from the sound source.

2.4.4 Sound Levels

Since the occurring sound pressures, particle velocities and sound powers extend over a large numerical range, logarithmic ratios called levels are usually formed. The use of levels has the additional advantage that our hearing sensation roughly corresponds to a logarithmic stimulus scale. Thus, the wide perceptual range of the human auditory system is described from 0 dB (hearing threshold) to approximately 140 dB (pain threshold). It should be noted, however, that the calculation rules for logarithms are applied.

The sound pressure level L_p is defined as follows

$$L_p = 10\log\frac{\tilde{p}^2}{\tilde{p}_0^2} = 20\log\frac{\tilde{p}}{\tilde{p}_0} \tag{25}$$

where $\tilde{p}_0$ corresponds to reference sound pressure, which is internationally standardized and represents the hearing threshold at 1 kHz. For airborne sound $\tilde{p}_0$ is 2×10^{-5} Pa.

If there are several sound sources, the total sound pressure level is calculated according to equation 26.

$$L_{p,\mathrm{total}} = 10\log\left[\frac{p_1^2 + p_2^2 + \cdots + p_\mathrm{n}^2}{p_0^2}\right] \tag{26}$$

or with the individual sound pressure level values

$$L_{p,\mathrm{total}} = 10\log\left[10^{\frac{L_{p1}}{10}} + 10^{\frac{L_{p2}}{10}} + \cdots + 10^{\frac{L_{pn}}{10}}\right] \tag{27}$$

The local particle velocity level L_v is defined according to equation 28, with the reference value $\tilde{v}_0$ being 5×10^{-8} m s^{-1}.

$$L_v = 10 \log \frac{\tilde{v}^2}{\tilde{v}_0^2} = 20 \log \frac{\tilde{v}}{\tilde{v}_0} \tag{28}$$

And finally, the sound power level L_w is defined as

$$L_w = 10 \log \frac{P}{P_0} \tag{29}$$

with the reference sound power P_0 being 10^{-12} W. The calculation of the total sound power level of multiple sound sources is identical to the calculation of the total sound pressure level.

$$L_{w,\text{total}} = 10 \log \left[\frac{P_1^2 + P_2^2 + \cdots + P_n^2}{P_0^2} \right] = 10 \log \left(\sum_{i=1}^{N} \frac{P_i^2}{P_0^2} \right) \tag{30}$$

and

$$L_{w,\text{total}} = 10 \log \left[10^{\frac{L_{w1}}{10}} + 10^{\frac{L_{w2}}{10}} + \cdots + 10^{\frac{L_{wn}}{10}} \right] = 10 \log \left(\sum_{i=1}^{N} 10^{\frac{L_i}{10}} \right) \tag{31}$$

Table 4 gives some useful level differences, e.g. a doubling of the sound power corresponds to a sound power level increase of 3 dB. Table 5 contains some examples of level quantities for everyday noise situations.

Table 4: Some useful level differences. [11]

ratio of sound pressure	ratio of sound intensity or power
$\sqrt{2}$: 1 ≈ 3 dB	$\sqrt{2}$: 1 ≈ 1.5 dB
2 : 1 ≈ 6 dB	2 : 1 ≈ 3 dB
3 : 1 ≈ 10 dB	3 : 1 ≈ 5 dB
5 : 1 ≈ 14 dB	5 : 1 ≈ 7 dB
10 : 1 = 20 dB	10 : 1 = 10 dB

Table 5: Sound pressure level examples for everyday noise situations. [42]

effective sound pressure (Pa)	sound pressure level (dB)	situation (-)
2×10^{-5}	0	hearing threshold
2×10^{-4}	20	forest with low wind
2×10^{-3}	40	library
2×10^{-2}	60	office
2×10^{-1}	80	busy city street
2×10^{0}	100	pneumatic hammer, siren
2×10^{1}	120	jet aircraft take-off
2×10^{2}	140	pain threshold

2.4.5 Bandpass Filters

In order to determine the frequency composition, i.e. the spectrum of a sound event, a frequency analysis must be carried out. In some cases, a high-resolution method is required to determine the spectral content of signals. A frequently used method is the so-called FFT analysis. [42]

Often, however, high resolution is neither desired nor necessary. In this case, the determination of the frequency composition of signals is carried out in wider sub-bands using filters. These filters consist of electrical networks that only allow an applied voltage to pass if it is in a certain frequency range. The filter is characterised by its bandwidth Δf, by the lower passband limit f_l and the upper passband limit f_u and by the centre frequency f_m. The bandwidth is equal to the difference between f_l and f_u.

$$\Delta f = f_\mathrm{u} - f_\mathrm{l} \tag{32}$$

In acoustics, almost only filters with a constant relative bandwidth are used. In this case, the bandwidth is proportional to the centre frequency of the filter, i.e. the bandwidth increases with increasing centre frequency.

The most important representatives of filters with constant relative bandwidth are the octave filter and the one-third octave filter. The following relationship applies to all filters with constant relative bandwidth:

$$f_\mathrm{m} = \sqrt{f_\mathrm{l}\, f_\mathrm{u}} \tag{33}$$

whereby the following also applies for one-third octave bands

$$f_\mathrm{u} = 2^{\frac{1}{3}} f_\mathrm{l} \tag{34}$$

and

$$f_{m+1} = 2^{\frac{1}{3}} f_m \tag{35}$$

Similarly, for octave bands

$$f_u = 2 f_l \tag{36}$$

and

$$f_{m+1} = 2 f_m \tag{37}$$

Table 6: One-third octave bands.

f_l (Hz)	f_m (Hz)	f_u (Hz)
14.1	16	17.8
17.8	20	22.4
22.4	25	28.2
28.2	31.5	35.5
35.5	40	44.7
44.7	50	56.2
56.2	63	70.8
70.8	80	89.1
89.1	100	112
112	125	141
141	160	178
178	200	224
224	250	282
282	315	355
355	400	447
447	500	562
562	630	708
708	800	891
891	1000	1122
1122	1250	1413
1413	1600	1778
1778	2000	2239
2239	2500	2818
2818	3150	3548
3548	4000	4467
4467	5000	5623
5623	6300	7079
7079	8000	8913
8913	10000	11220

The band limits and centre frequencies of one-third octaves and octaves are specified in the standard sheets DIN 45651 and DIN 45652. Table 6 gives the centre frequencies as well as the lower and upper limits of the one-third octave bands.

The advantage of measuring one-third octave levels is the higher resolution as more measuring points in the same frequency range are obtained. The octave levels are always higher than the one-third octave levels due to the larger frequency band. The calculation of the octave level based on the corresponding one-third octave levels can be done according to equation 27.

2.4.6 Frequency Rating

The relationship between the objective quantities of sound pressure or sound pressure level and the subjective quantity of loudness is actually very complicated. An identical sound pressure at two different frequencies, i.e. a higher and a lower tone, does not necessarily mean that the perceived loudness is also the same.

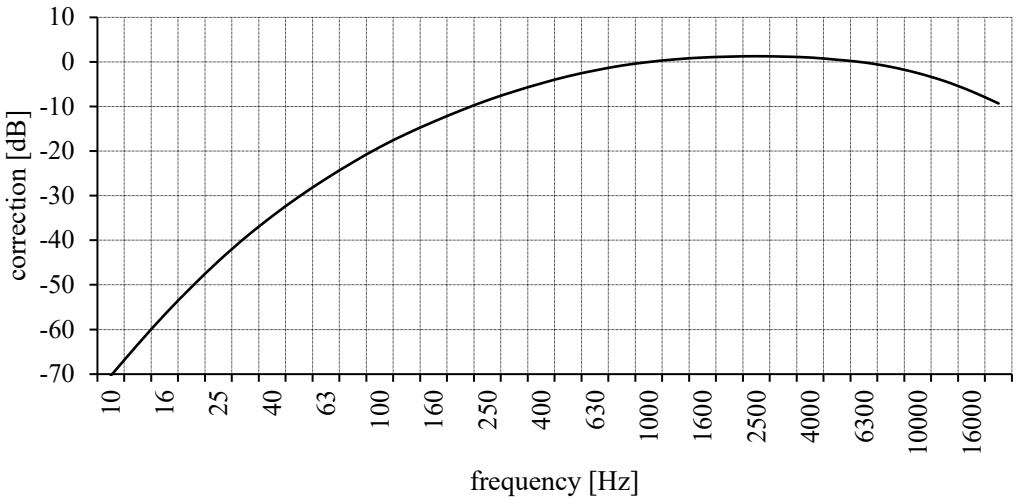

Fig. 27: A-weighting curve.

In addition, the subjective perception of loudness depends not only on the frequency but also on the bandwidth of the sound event. Taking into account all the characteristics of the human auditory system when evaluating loudness would require a very large effort. For this reason, a frequency-weighted sound level is mostly used, which at least fundamentally takes into account the sensitivity of human hearing with comparatively little effort. This so-called A-weighted sound level contains all frequency components of the audible spectrum. In practice, the dB(A) value is measured using A-filter, whose frequency response is shown in Fig. 27. The curve indicates, that the human hearing system is less sensitive to low and very high frequencies than to medium frequencies.

2.5 Compressor Simulation

Three different approaches are commonly used to model a hermetic reciprocating compressor:

- 0d approach: This modelling approach consists of a very simplified representation of the compressor and its components. Using the first law of thermodynamics, the energy fluxes are balanced and global conclusions can be made about heat fluxes or COP. An advantage of these highly simplified models is the low computing effort which enables very short computing times. However, some physical effects, e.g. the influence of certain geometric aspects, cannot be considered in a 0d approach.
- 1d approach: The gas path through the compressor is divided into a finite number of control volumes. The 1d transient conservation equations for mass, momentum and energy are solved for each control volume. In contrast to 0d models, 1d models can also capture fundamental fluid dynamics. Due to the low computing effort, validated 1d models are particularly suitable for parameter studies.
- 3d approach: The computational domain is divided into a 3d computational grid where the conservation equations of mass, momentum and energy are solved for each grid cell. 3d FSI simulations produce the most accurate results regarding the fluid dynamics, valve motion and heat transfer. However, it is also the most computationally intensive approach. Due to the high computing effort, the 3d approach is mainly used for the analysis of individual compressor components and local effects.

2.6 Design of Experiments (DOE)

DOE is a systematic approach for efficient planning and evaluation of experiments based on statistical methods. The roots of modern statistically designed experiments go back to the work of R.A. Fisher in the field of agricultural experimentation. Fisher was a gifted mathematician who graduated at the Cambridge University. In 1919, he turned to the Rothamsted Experimental Station, one of the oldest agricultural research institutions in the world. In his work on agricultural and biological experiments, he was confronted with time-consuming and costly experiments and a large number of variations, which often confused the results. Fisher therefore worked on experimental techniques that i) eliminate natural variation as much as possible, ii) prevent non- eliminated variation from confusing or biasing the tested effects, and iii) can detect cause and effect with minimal experimental effort. He first published his ideas on planning experiments 1926 in the Paper "The arrangement of field experiments" [7] and 9 years later he published the book "The Design of Experiments" [8]. [24]

In the meantime, the use of DOE has spread far beyond the agricultural origins. There is not a single area of science and engineering in which DOE has not been successfully used. [41]

Although originally developed for physical experiments, DOE can also be applied to simulation-based experiments. The direct use of complex simulation models for the analysis or optimization of technical systems is often not practicable due to the high computational effort. Therefore, response models, also called surrogate models or metamodels, are derived from these simulation models using a DOE approach.

The general procedure of a DOE approach is illustrated in Fig. 28. The individual elements of this approach are described in more detail below.

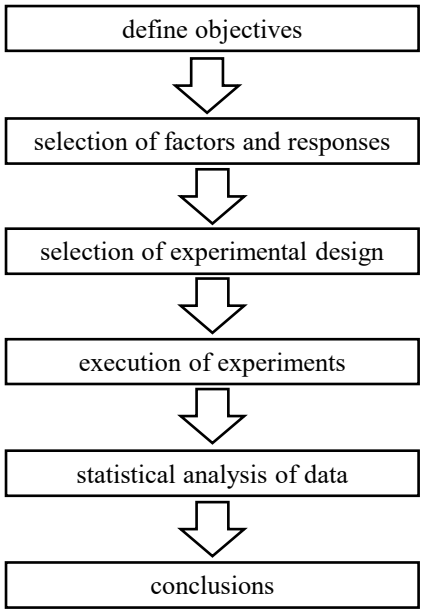

Fig. 28: General procedure of a DOE approach.

2.6.1 Define Objectives

The first stage in a DOE includes the identification of the problem as well as the formulation of the experimental objectives. Reasons for conducting a DOE can be versatile. Objectives can be to determine the cause for variation in measured responses, to find conditions leading to

maximum or minimum responses, to compare responses between different settings of controllable variables or to obtain mathematical models for response prediction. The objective is crucial in selecting a suitable experimental design.

2.6.2 Selection of Factors and Responses

The DOE approach requires to analyse the system under consideration with all its potential influences. For this purpose, a system boundary must first be drawn. Fig. 29 shows the parameter diagram of a general system. Some input (energy, material, etc.), controllable parameters (design parameters, operational parameters, etc.) and uncontrollable parameters (environmental influences, measurement errors, etc.) lead to some output of the system.

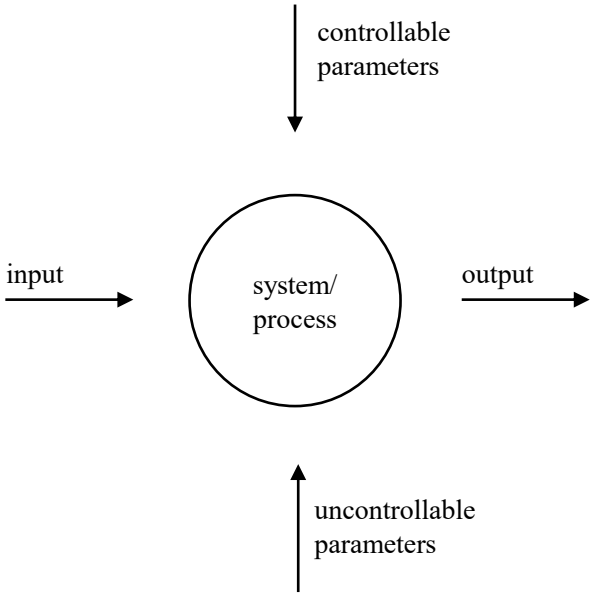

Fig. 29: Parameter diagram of a system.

Factors represent the subset of the controllable parameters whose value (level) will be varied within the DOE approach, i.e. they are varied from run to run. A general objective of an experimenter is to determine the influence of these factors on the responses (dependent variables) of a system. In contrast to the factors, controllable parameters which are not of special interest are held constant at a certain value. Uncontrollable parameters like environmental influences may have a large influence on the system behaviour. If they are known, they must be recorded and included in the subsequent data analysis. If they are not known, experimentation in random run order can help to get proper results from the data analysis.

The responses should represent measurable output variables which provide a meaningful information about the system under study. Depending on the objectives, there might be one or more relevant responses.

2.6.3 Selection of Experimental Design

A widely used approach for the investigation of several factors is the so-called one factor at a time (OFAT) approach, which is very inefficient and can sometimes be misleading when investigating new systems. In an OFAT approach, always one factor is varied, while the others are kept constant. The OFAT approach is neither capable of estimating interaction effects between factors, nor does it guarantee that the tested combinations lead to the optimal result [36, 41, 50]. In contrast, a statistical designed experiment involves the simultaneous variation

of several factors in a systematic manner, where the factor settings in one experimental run is referred as treatment combination. Such experimental designs efficiently lead to valid and objective results. Well-chosen experimental designs maximise the amount of information that can be obtained at a given experimental effort.

Three important principles constitute a statistical designed experiment, namely randomization, blocking and replication. Randomisation means that the individual experimental runs of an experiment (observations) are carried out in a random order. This helps to balance the effects of all unknown disturbances or uncontrollable parameters, e.g. environmental influences, which can influence the results of an experiment. Blocking is used to reduce or eliminate the contribution of certain nuisance factors to the experimental error. Therefore, the entire experimental design is divided in homogeneous blocks in which the nuisance factors are held constant. Replication means that one treatment combination is tested more than once in order to achieve a certain precision in measuring treatment effects.

The selection of an adequate experimental design depends on the objectives of the experiment and the number of factors involved in the investigation. The experimental design is typically structured in table form, with each line representing an experimental run and each column representing the corresponding factor level. Factor levels are usually illustrated in coded units, e.g. if a factor is investigated at two levels, −1 corresponds to the low and +1 corresponds to the high factor level. The relationship between coded and natural factor units is given in equation 38.

$$\chi = \frac{\xi - \frac{\xi_+ + \xi_-}{2}}{\frac{\xi_+ - \xi_-}{2}} \tag{38}$$

where χ is the coded factor level and ξ corresponds to the natural factor level. Coded factor units facilitate the comparison of different factor effects due to the common nominal scale.

Physical experiments are often very costly and the number of factors that can be set in a controlled manner has narrow limits. In physical experiments, the experimental designs are therefore usually kept simple. However, some sources of variability may make it difficult to interpret the experimental results. In contrast, simulation experiments often allow large experimental designs with many factors. This requires proper simulation models which are accurate and able to capture non-linear relationships. In complex cases, DOE competes with other methods of multivariate data analysis (e.g. neural networks, kriging or multivariate adaptive regression splines). [52]

The selection of an adequate experimental design also requires to think about the required empirical model to describe the results. In many cases, a low-order polynomial model will be appropriate [41]. A general first-order model of two factors is given in equation 39.

$$y = \beta_0 + \beta_1 x_1 + \beta_2 x_2 + \varepsilon \tag{39}$$

where y is the response, x_1 and x_2 represent the factor levels, β_0, β_1 and β_2 are the unknown model parameters which will be estimated from the experimental data and ε is the random error term. First-order models are extensively used in screening experiments, with the primary

purpose to screen out the most active factors, i.e. the factors with the largest main effect.

Since interactions between factors are very common, the first-order models are often extended with interaction terms, see equation 40.

$$y = \beta_0 + \beta_1 x_1 + \beta_2 x_2 + \beta_{12} x_1 x_2 + \varepsilon \tag{40}$$

where β_{12} corresponds to the interaction effect of the two factors.

Optimization experiments require models that accurately describe the relationship between factors and response. Therefore, second-order models are widely used if quadratic behaviour is expected within the considered factor space. This requires the selection of a suitable experimental design in which the factors are varied on at least three levels.

$$y = \beta_0 + \beta_1 x_1 + \beta_2 x_2 + \beta_{12} x_1 x_2 + \beta_{11} {x_1}^2 + \beta_{22} {x_2}^2 + \varepsilon \tag{41}$$

Factorial Design (FD)

The factorial design is a very common design, which contains all possible factor level combinations. Fig. 30 shows a comparison of an OFAT and a factorial design based on a fictional experiment with two factors A and B, each tested at two levels. The circles in the diagram represent the individual experimental runs. If the objective is to find the optimum response, a classical OFAT experiment can be divided in two steps. First, one factor, e.g. A, is varied while factor B is held constant. Second, factor A is held constant at its predetermined optimum level, while factor B is varied.

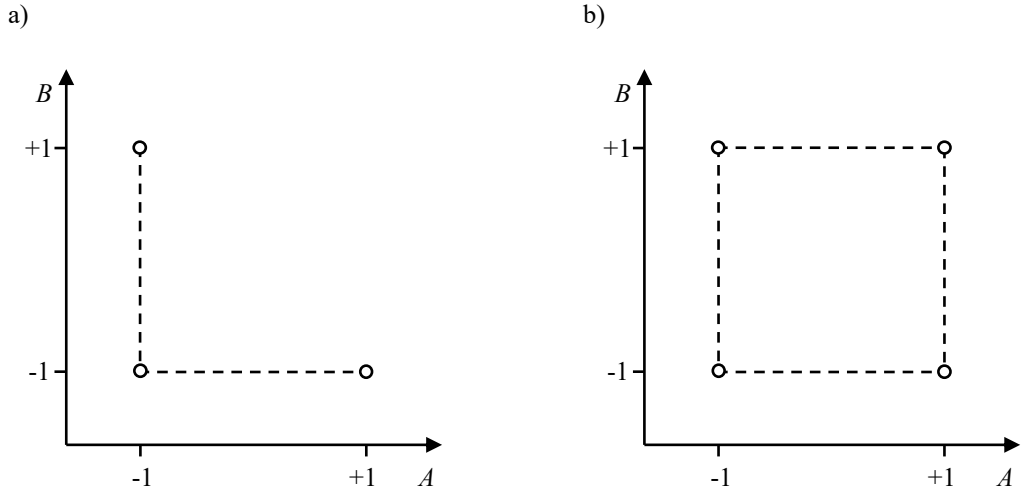

Fig. 30: Comparison of OFAT approach a) and factorial design b).

If four replicate experiments per factor level were to be made in order to reach sufficient statistic power, a total of 12 experimental runs would be required using the OFAT approach. However, if a factorial experiment is conducted, one can make use of hidden replication [36, 41]. As shown in Table 7, a two-level factorial design with two factors already includes two replicates of each factor level. In general, the number of replicates of a specific factor level equals the product of the number of levels of all other factors [36]. In the given example, four replications per factor level would therefore only require a total of 8 experiments. Thus, the relative efficiency of the factorial design compared to the OFAT is 12/8 = 1.5. The relative efficiency

increases further as the number of factors increase, see Fig. 31.

Table 7: Two-level factorial design with factors A and B, and the response y.

run	A	B	y
1	-1	1	y_1
2	1	1	y_2
3	-1	-1	y_3
4	1	-1	y_4

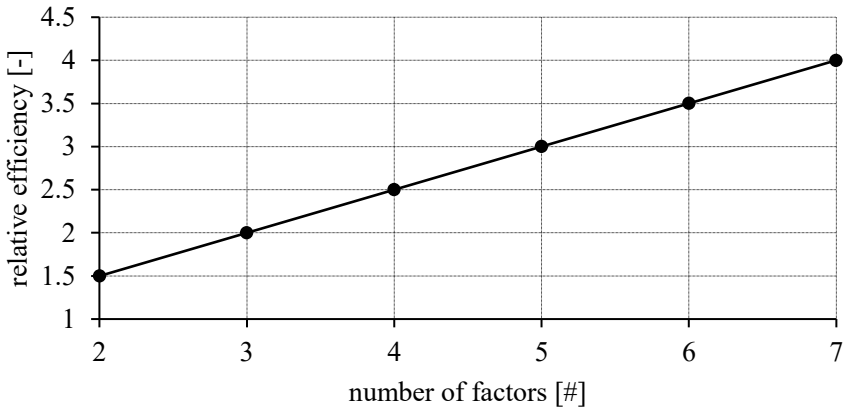

Fig. 31: Relative efficiency of a factorial design compared to an OFAT experiment (two-level factors).

A factorial design is orthogonal and balanced. Orthogonality means that no combination of two columns in an experimental design are correlated. Thus, all effects can be estimated independently of each other. An experimental design is balanced if all factor levels of the factors occur equally often and at a specific level of one factor, the levels of the other factors are equally distributed, see Table 7. Therefore, from a mathematical point of view, it is no problem to detect a small effect of one factor, even if the other factors have a much larger effect [52].

Fractional Factorial Design (FFD)

Since the number of experimental runs of a factorial design with k factors is equal to 2^k, the experimentation effort might become unfeasible if the number of factors is high. Table 8 shows the experimental runs of a two-level factorial design depending on the number of factors.

Table 8: Number of experimental runs in a two-level factorial design.

number of factors	number of runs
2	4
4	16
6	64
8	256
10	1024

A fractional factorial design is often a good compromise between experimental effort and

information that can be drawn from it. In a fractional factorial design only a fraction of the entire factorial design is considered. A common notation of fractional designs is 2^{k-p}, where k corresponds to the number of factors and $(1/2)^p$ represents the fraction of the full factorial 2^k design. For example, a 2^{6-1} design represents a half fraction of a 2^6 full factorial design, 2^{6-2} represents a quarter fraction and so on. A 2^{6-1}design means that 6 factors are investigated at two levels in just 32 instead of 64 experimental runs.

A consequence of the lower number of experimental runs is that some effects are confounded. Confounding or aliasing means that some effects are indistinguishable. For example, if the main effect of a factor A is confounded with the three-factor interaction ABC, it is not possible to determine whether the estimated effect originates from the factor A, the interaction ABC, or both. The degree of confounding is described by the resolution of the design, see Table 9.

Table 9: resolution of fractional factorial designs [18].

resolution	main effects aliased with	2-factor interactions aliased with
III	2-factor interactions	main effects
IV	3-factor interactions	2-factor interactions
V	4-factor interactions	3-factor interactions

In order to preserve orthogonality, the fraction of a full factorial design must be taken with care. One way to select a half fraction of a 2^k factorial design is to choose the runs where the coded factor levels of an interaction column (preferably the highest order interaction) are constant [36]. This procedure is illustrated in Table 10. The left side represents a 2^4 factorial design, where the columns A, B, C and D give the corresponding factor levels which are actually set in the experimental runs and $ABCD$ represents the interaction of these four factors. The level of the four-factor interaction $ABCD$ results from the product of the corresponding factor levels. All runs with high level (+) of $ABCD$ are selected to form the half fraction factorial design as shown at the right side of Table 10. A further inspection of the 2^{4-1} design shows, that in each run, the level of D equals the product of A, B and C. This means that the effect estimated for the factor D is completely confounded with the three-factor interaction ABC. In addition, some other effects are confounded. However, this is a fair price to pay, since in most cases main effects and low order interactions are more dominant than higher order interactions.

Table 10: Creating a half-fraction factorial design from a factorial design [36].

2^4 factorial design						2^{4-1} fractional factorial design (half-fraction)				
run	A	B	C	D	$ABCD$	run	A	B	C	D
1	−	−	−	−	+	1	−	−	−	−
2	+	−	−	−	−	10	+	−	−	+
3	−	+	−	−	−	11	−	+	−	+
4	+	+	−	−	+	4	+	+	−	−
5	−	−	+	−	−	13	−	−	+	+
6	+	−	+	−	+	6	+	−	+	−
7	−	+	+	−	+	7	−	+	+	−
8	+	+	+	−	−	16	+	+	+	+
9	−	−	−	+	−					
10	+	−	−	+	+					
11	−	+	−	+	+					
12	+	+	−	+	−					
13	−	−	+	+	+					
14	+	−	+	+	−					
15	−	+	+	+	−					
16	+	+	+	+	+					

In practice, fractional factorial designs are usually created the other way around. Instead of starting with a factorial design and eliminating runs, start from a factorial design with the desired number of runs and add additional factors. The factor levels of the added factors are chosen to correspond to the product of other factor levels. The complete list of interactions confounded with each main effect and interaction is called the confounding pattern or alias structure of the design. [36]

For example, in the 2^{4-1} design above, where the levels of the fourth factor are equal to the product of the levels of the first three factors, $D = ABC$ is called the *generator* of the design. If we multiply both sides of the *generator* with D, we get $D^2 = ABCD$, or $I = ABCD$, where I represents a column of plus signs. $I = ABCD$ is called the *defining relation* of the fractional factorial design. The length of the shortest word in the defining relation gives the resolution of the fractional factorial design. For example, the 2^{4-1} design with $I = ABCD$ has the resolution IV. A multiplication of both sides of this equation with any factor or interaction leads to the corresponding confounding effect. For example, if both sides of the defining relation are multiplied with A, we get $AI = AABCD$, or $A = BCD$. This means that the factor A is confounded with the three-factor interaction BCD. The estimated factor effect of A is actually a sum of the effects of A and the three-factor interaction BCD, which is why we write $A + BCD$. The complete alias pattern is obtained by multiplying the *defining relation* with each main and interaction effect, which results in $I + ABCD$, $A + BCD$, $B + ACD$, $C + ABD$, $D + ABC$, $AB + CD$, $AC + BD$ and $AD + BC$. The alias pattern can also be illustrated graphically, see Fig. 32. The colour intensity provides information about the correlation between the effects.

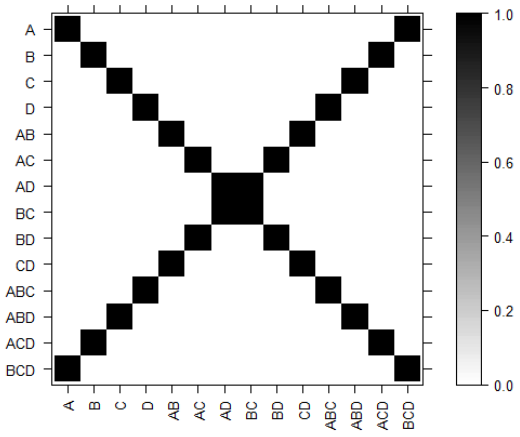

Fig. 32: Colour map of alias pattern of 2^{4-1} design.

Fractional factorial designs are frequently used in various stages of product development as well as process and quality improvement [18]. Resolution III 2^{k-p} fractional factorial designs are particularly suitable for screening experiments, which are usually performed at an early stage of a project with many potentially relevant factors involved. A screening experiment reveals the factors with the largest effects, which can be studied in more detail in follow-up experiments.

Plackett-Burman (PB) Designs

The number of runs in two-level factorial and fractional factorial designs is always a power of 2, i.e. 8, 16, 32, 64, etc., thus the steps between the run sizes are large and not always practical for screening experiments. A frequently used alternative are Plackett-Burman designs. Like 2^{k-p} designs, PB designs consider two levels for each factor, however, the run sizes are multiples of 4, i.e. 8, 12, 16, 20, etc. If the run size of a PB design is also a power of two, it is equal to the 2^{k-p} design. Other run sizes retain the orthogonality property, but have no *generators* or a *defining relation*. The designs for run sizes of 12, 20, and 24 are created through cyclic rotation of the factor levels of the first run as given in Table 11. The factor levels of the following run correspond to the factor level of the previous run but shifted by one factor to the right and the last factor level of the shifted row is assigned to the first factor, see Table 12. [36]

Table 11: Factor levels of first run in a PB-design [36].

run size	factor levels
12	+ + − + + + − − − + −
20	+ + − − + + + + − + − + − − − − + + −
24	+ + + + + − + − + + − − + + − − + − + − − − −

Table 12: 12-run PB-design [36].

run	A	B	C	D	E	F	G	H	J	K	L
1	+	+	−	+	+	+	−	−	−	+	−
2	−	+	+	−	+	+	+	−	−	−	+
3	+	−	+	+	−	+	+	+	−	−	−
4	−	+	−	+	+	−	+	+	+	−	−
5	−	−	+	+	+	+	−	+	+	+	−
6	−	−	−	+	−	+	+	−	+	+	+
7	+	−	−	−	+	−	+	+	−	+	+
8	+	+	−	−	−	+	−	+	+	−	+
9	+	+	+	−	−	−	+	−	+	+	−
10	−	+	+	+	−	−	−	+	−	+	+
11	+	−	+	+	+	−	−	−	+	−	+
12	−	−	−	−	−	−	−	−	−	−	−

PB-designs are of resolution III and have a complex alias structure, i.e. interactions are only partially confounded with main effects that are not included in the respective interaction. It is recommended to leave one to three columns unoccupied by factors in order to be able to estimate the occurring bias due to confounding [52]. Fig. 33 gives a comparison of the alias pattern between a 12-run PB-design with 7 factors and a 2^{7-4} design (8 runs).

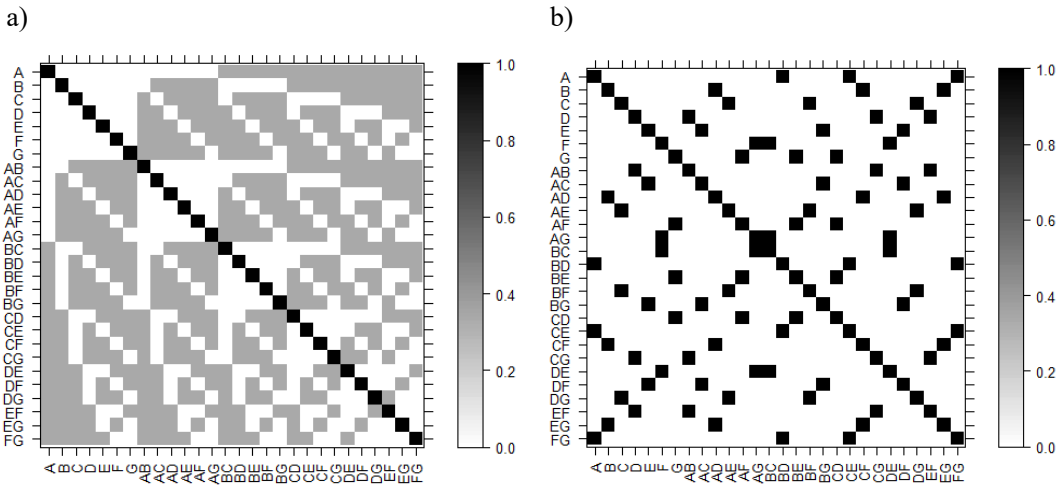

Fig. 33: Colour map comparison of alias pattern between a 12-run PB-design with 7 factors in a) and a resolution III 2^{7-4} design in b).

The comparison of the colour maps shows, that in the 2^{7-4} design confounding occurs with a correlation of 1, whereas in the PB-design it is smaller (0.33). Thus, some interactions can be included in the response model as long as the total number of terms in the model is smaller than the runs of the design.

Response Surface Design (RSD)

RSDs are used to find an appropriate approximation of the true functional relationship between a response and a set of continuous factors in order to conduct an optimization. Usually, a full quadratic model, sometimes referred to as response surface model, as given in equation 41 is

used to describe this relationship. Although, it is unlikely that the quadratic model is capable of describing the true functional relationship over a large factor space, it can work well within a reasonable small region.

For an effective estimation of the model parameters in equation 41, results from an adequate experimental design are required. To estimate for quadratic effects, at least 3 levels per factor are required. Furthermore, a general quadratic model with k factors consists of $1 + 2k + k(k - 1) / 2$ model coefficients, which gives the minimum number of required experimental runs [36]. RSD therefore require many experimental runs, which is why they are usually selected at a later stage of experimentation, when the important factors have already been identified.

The variance of a predicted value at a certain factor setting is of special importance in a response surface model. Since the position of the optimum of a response is not known in advance, it is desired to have a nearly constant variance of the predicted value in the entire design region.

Rotatability and uniform precision are further important properties of response surface designs. A design is called to be rotatable, if the variance of the predicted value only depends on its distance from the design origin. Further, a design has uniform precision, if the variance of a predicted value is the same at the origin and the radius one in the coded design region. Many standard RSD have these properties or are at least very close to having them. [36]

The most popular class of RSD are the so called central composite designs (CCD) from Box and Wilson [13]. In general, a CCD consists of 2^k full factorial design (or a 2^{k-p} fractional factorial design with resolution V) with n_F factorial runs, $2k$ star runs and n_C centre runs. A CCD requires five levels for each factor ($-\alpha$, -1, 0, $+1$, $+\alpha$), where the correct choice of α-value ($\alpha = n_F^{1/4}$) leads to a rotatable design [41]. Fig. 34a shows a CCD with three factors. Sometimes a cuboidal region rather than a spherical region may be the preferred choice, e.g. if the variation of some factors is limited. In this case, a face-centred CCD, where $\alpha = \pm 1$ can be used, see Fig. 34b. In contrast to the circumscribed CCD, the face-centred CCD is not rotatable, however, it requires only three-levels of each factor.

A CCD allows for a sequential experimentation, i.e. the CCD can be run as sequence of two blocks. In the first block, the 2^k design and the centre points at the mid-level of each factor are completed. Subsequently, it can be checked, if a linear model is adequate to represent the data. If this is the case, the remaining block is not required. If the linear model is not adequate, the second block is completed and a block variable is added to the model to account for any external influences between the first and second experimental block. [36]

An alternative frequently used RSD is the so-called Box-Behnken design (BBD) [12]. The BBD requires three levels per factor to estimate the general quadratic model. In general, the BBD requires fewer experimental runs than a CCD, which makes them less costly. However, BBD cannot be built in two blocks beginning with a 2^k factorial design as with the CCD. In addition, it is not possible to check for adequacy of the quadratic model since only three factor levels are included. A BBD should be used if one can be sure that a linear model is not sufficient and the number of runs of a CCD is not feasible. Fig. 34c shows a BBD with three factors.

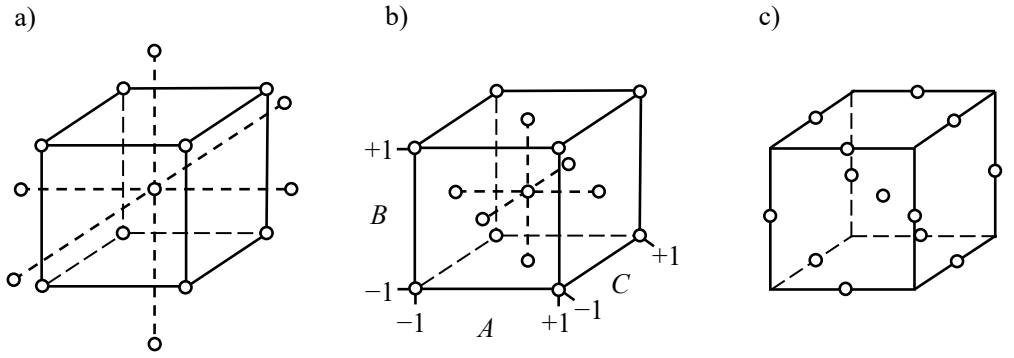

Fig. 34: Original CCD in a), face-centred CCD in b) and Box-Behnken design in c) for 3 factors.

Definitive Screening Designs (DSD)

Since response surface designs require many experimental runs, they are rarely conducted with more than six factors [36]. [33] proposed a new class of design for screening quantitative factors in the presence of active first and second-order effects, called Definitive Screening Design (DSD). DSDs are small designs from which significantly more information can be obtained compared to a resolution III fractional factorial screening design.

Considering quantitative three-level factors, a DSD is capable of estimating quadratic factor effects and requires only $2k+1$ runs for k factors. For designs having 6 to 12 factors, the DSD allows for effect estimation of the full quadratic model in any three factors. A DSD, therefore, offers a good alternative if a classic two-level resolution III or IV fractional factorial design is not sufficient, but the experimental effort of an RSD does not seem feasible.

2.6.4 Statistical Analysis of Data

After a suitable experimental design has been selected, the individual experimental runs can be executed. The experimental matrix is processed line by line and the corresponding responses are recorded. Subsequently, the experimental design matrix can be extended by columns representing the recorded responses. This matrix, consisting of factor level settings and corresponding responses, forms the basis for the following analysis. Depending on the objective, the statistical analysis of the data may take different forms. For example, if only a few beneficial factor level combinations are sought, no further postprocessing is required. Usually, however, response models are generated from the data, which can be used for further analysis such as sensitivity analyses or optimisations. A particularly helpful analysis tool is the effect plot, where main and interaction effects are displayed graphically.

A general approach for a statistical analysis of designed experiments is summarized in Fig. 35. The individual steps are usually performed using a proper statistical software package, e.g. RStudio, Minitab, etc.

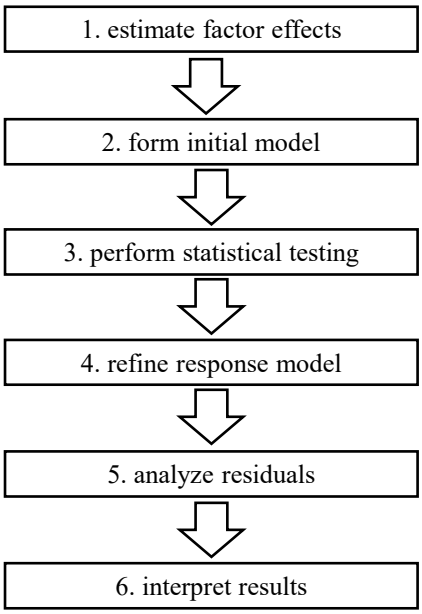

Fig. 35: General analysis procedure statistical analysis of designed experiments. [41]

The first step includes the estimation of factor effects in terms of signs and magnitudes. It gives a preliminary picture of which factors and interactions are important and how the factors must be adjusted to improve the response. Subsequently, an initial full model of the experiment including main and interaction effects is created based on linear regression. The third step includes the test for statistical significance of the estimated main and interaction effects based on the analysis of variance approach (ANOVA). Nonsignificant variables are usually removed from the full model in the fourth step, leading to a refined model. The fifth step includes to check for model adequacy and assumptions through an analysis of the residuals. If the model is inadequate or the assumptions are violated, some further model adjustments are required. Otherwise, the final step can follow where conclusions can be drawn based on graphical analysis (e.g. main- or interaction effect plots or response surface and contour plots). Alternatively, the empirical model which describes the response in relation to the factor settings can be used in further optimization approaches.

Estimation of Factor Effects

In the following example, two different experiments based on the factorial design in Table 7 are analysed. Fig. 36 shows both experiments with the corresponding responses.

The effect of a factor (main effect) is defined as the difference in average response obtained at high level (+1) and low level (−1) of the factor. For example, in the factorial experiment illustrated in Fig. 36b, the main effects of factor A and B are

$$A = \frac{52 + 25}{2} - \frac{2 + 47}{2} = 14 \tag{42}$$

and

$$B = \frac{47 + 25}{2} - \frac{2 + 52}{2} = 9 \tag{43}$$

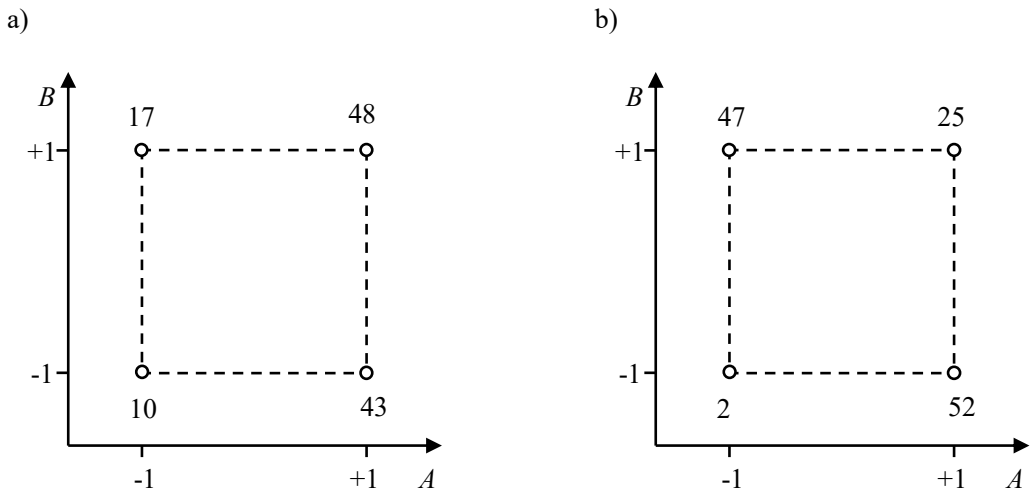

Fig. 36: Two-level factorial experiment with two factors. Response y is shown at the corners for an experiment without a), and with distinctive interaction effects b).

In order to determine the interaction effect AB, first the effect of A at high and low level of B must be evaluated

$$A_{B+} = 25 - 47 = -22 \tag{44}$$

$$A_{B-} = 52 - 2 = 50 \tag{45}$$

Subsequently the interaction effect AB is calculated as the average difference between A_{B+} and A_{B-}

$$AB = \frac{-22 - 50}{2} = -36 \tag{46}$$

A common way to visualize the main and interaction effects is the effect plot as shown in Fig. 37, where size and direction of the effects is clearly visible. The dashed horizontal line represents the intercept, which is the average response of all experimental runs.

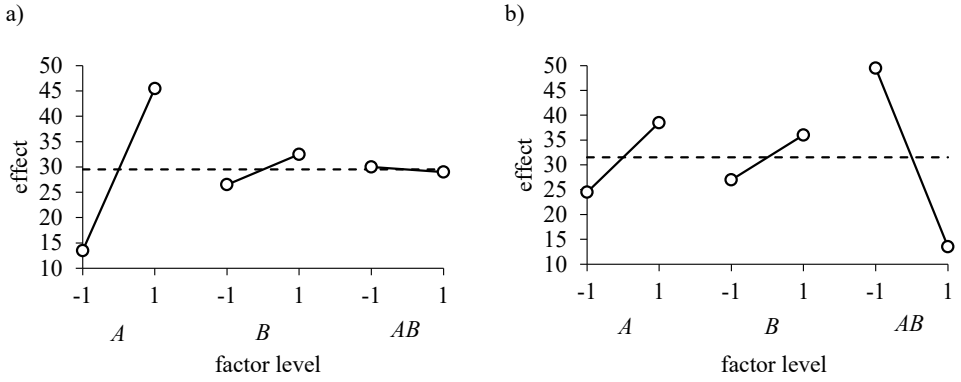

Fig. 37: Effect plot two-level factorial experiment with two factors, a) without interaction and b) with interaction effects.

For example, in Fig. 37a, the factor A has the largest main effect. If the factor level of A is increased from −1 to +1, the relative increase in response will be from 13.5 to 45.5. In contrast to A, the main effect of B and the interaction effect AB is very small. In Fig. 37b the largest effect comes from the interaction AB. The level of the interaction AB is obtained by multiplying the levels of A and B. Since there are two possibilities for each level of AB, a different tool is required to further analyse the two-factor interaction effects.

The two-factor interaction plot as illustrated in Fig. 38 is a further frequently used tool to investigate interactions. It plots the response over factor A at both levels of factor B. The parallel lines in Fig. 38a indicate that no interaction is present while in Fig. 38b a large interaction can be observed.

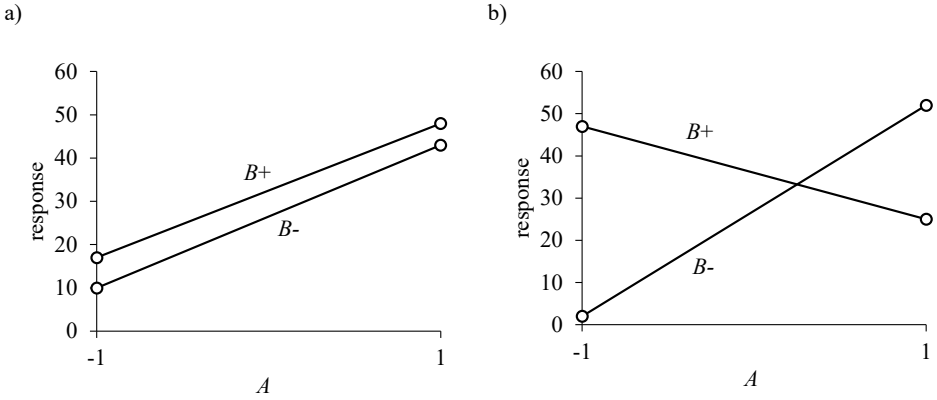

Fig. 38: Two-factor interaction plot of factorial experiment without a) and with interaction effects b).

The main and interaction effects are closely related to the model parameters (least squares estimates) of the empirical model in equation 40. Since the step size of the coded factor levels is two (−1 to +1), the model parameter β_1 and β_2 equal to half of the corresponding main effects A and B, respectively. The same applies to the model parameter β_{12} and the interaction effect. This close relation always applies for a 2^k design [41]. The model parameter β_0 corresponds to the average of all four responses, also called intercept. Thus, the fitted regression model for the experiment in Fig. 36a reads as

$$y = 29.5 + 16x_1 + 3x_2 - 0.5x_1x_2 + \varepsilon \tag{47}$$

and for the experiment in Fig. 36b

$$y = 31.5 + 7x_1 + 4.5x_2 - 18x_1x_2 + \varepsilon \tag{48}$$

Initial Response Modelling

The relationship between a dependent variable y and k independent variables $x_1, x_2, \ldots, x_k$ can be characterised by a mathematical model which is obtained through multiple linear regression based on the experimental data. This model forms the basis for the interpretation of experimental results. In most cases, the true functional relationship between the dependent and the independent variables is unknown, which is why a suitable approximation function must be chosen. Low-order polynomial models are widely used as approximation function. Equation 49

shows a multiple linear regression model with k independent variables

$$y = \beta_0 + \beta_1 x_1 + \beta_2 x_2 + \cdots + \beta_k x_k + \varepsilon \tag{49}$$

where the parameters β_j, j = 0, 1, …, k, are called the regression coefficients. They represent the expected change of y per unit change in x_j when all remaining independent variables are held constant. In general, any regression model which has linear parameters can be written in the form of equation 49. For example, taking a response surface model with two independent variables in the form

$$y = \beta_0 + \beta_1 x_1 + \beta_2 x_2 + \beta_{12} x_1 x_2 + \beta_{11} {x_1}^2 + \beta_{22} {x_2}^2 + \varepsilon \tag{50}$$

and if we write $x_3 = x_1 x_2$, $x_4 = x_1^2$, $x_5 = x_2^2$, $\beta_3 = \beta_{12}$, $\beta_4 = \beta_{11}$ and $\beta_5 = \beta_{22}$, equation 50 becomes

$$y = \beta_0 + \beta_1 x_1 + \beta_2 x_2 + \beta_3 x_3 + \beta_4 x_4 + \beta_5 x_5 + \varepsilon \tag{51}$$

A typical method used for estimating the regression coefficients in a multiple linear regression model is the method of least squares. In the following, the general concept of the least square method is presented. A more detailed description can be found in [41] and various statistic books.

Table 13: Data used for multiple linear regression

y	x_1	x_2	⋯	x_k
y_1	x_{11}	x_{12}	⋯	x_{1k}
y_2	x_{21}	x_{22}	⋯	x_{2k}
⋮	⋮	⋮	⋯	
y_n	x_{n1}	x_{n2}	⋯	x_{nk}

The least square method is based on the assumption that the error term ε has zero mean and a variance of σ^2 [$\varepsilon \sim \mathrm{N}(0, \sigma^2)$]. Suppose that $n > k$ observations on the response variable are available $(y_1, y_2, \ldots, y_n)$. For each observed response y_i we write x_{ij} for the i^{th} level of the independent or regressor variable x_j, see Table 13.

Equation 49 can also be written as

$$y_i = \beta_0 + \sum_{j=1}^{n} \beta_j x_{ij} + \varepsilon_i, \qquad i = 1, 2, \ldots, n \tag{52}$$

In matrix notation and including all data of Table 13 it leads to

$$\boldsymbol{y} = \boldsymbol{X\beta} + \boldsymbol{\varepsilon} \tag{53}$$

$$y = \begin{bmatrix} y_1 \\ y_2 \\ \vdots \\ y_n \end{bmatrix}, X = \begin{bmatrix} 1 & x_{11} & x_{12} & \dots & x_{1k} \\ 1 & x_{21} & x_{22} & \dots & x_{2k} \\ 1 & \vdots & \vdots & & \vdots \\ 1 & x_{n1} & x_{n2} & \dots & x_{nk} \end{bmatrix}, \beta = \begin{bmatrix} \beta_0 \\ \beta_1 \\ \vdots \\ \beta_k \end{bmatrix}, \text{and } \varepsilon = \begin{bmatrix} \varepsilon_1 \\ \varepsilon_2 \\ \vdots \\ \varepsilon_n \end{bmatrix} \tag{54}$$

The key idea of the least square method is to choose the regression coefficients so that the sum of the squared errors ε_i is minimized. The least square function L is

$$L = \sum_{i=1}^{n} {\varepsilon_i}^2 = \boldsymbol{\varepsilon}'\boldsymbol{\varepsilon} = (\boldsymbol{y} - \boldsymbol{X\beta})'(\boldsymbol{y} - \boldsymbol{X\beta}) \tag{55}$$

Thus, the least square estimators $\widehat{\boldsymbol{\beta}}$ must satisfy

$$\left.\frac{\partial L}{\partial \boldsymbol{\beta}}\right|_{\widehat{\boldsymbol{\beta}}} = -2\boldsymbol{X}'\boldsymbol{y} + 2\boldsymbol{X}'\boldsymbol{X}\widehat{\boldsymbol{\beta}} = \boldsymbol{0} \tag{56}$$

which leads to the least square estimators

$$\widehat{\boldsymbol{\beta}} = (\boldsymbol{X}'\boldsymbol{X})^{-1}\boldsymbol{X}\boldsymbol{y} \tag{57}$$

Hence, the fitted linear regression model can be expressed as

$$\widehat{\boldsymbol{y}} = \boldsymbol{X}\widehat{\boldsymbol{\beta}} \tag{58}$$

Analysis of Variance (ANOVA)

In principle, the experimental design with the corresponding responses represents a linear system of equations. Thus, a perfect fit of the experimental data will be obtained if the number of model parameters in a fitted regression model is equal to the number of equations (experimental runs). However, the estimated regression model parameters must not necessarily correspond to the true effects, since a regression model only establishes the mathematical relationship between one dependent variable and several independent variables.

The analysis of variance (ANOVA) approach is used to test for the statistical significance of the regression model parameters. It is one of the most important method for the evaluation of experiments and is usually part of every statistical software. The principle of ANOVA is based on the decomposition of variance into a systematic part (caused by the factor) and a random part (not explainable by the factor). The random part is mostly referred as error. The following gives an overview of the individual steps of an ANOVA based on a general two-factor factorial experiment. A more detailed description can be found in [41].

Let y_{ijk} be the observed response at the i^{th} level of factor A (i = 1, 2, …, a) and the j^{th} level of factor B (j = 1, 2, …, b) for the k^{th} replicate (k = 1, 2, …, n). The general design of a two-factor factorial experiment including replication is given in Table 14.

Table 14: General design of a two-factor factorial design.

B / A	1	2	…	b
1	$y_{111}, y_{112}, \dots, y_{11n}$	$y_{121}, y_{122}, \dots, y_{12n}$	…	$y_{1b1}, y_{1b2}, \dots, y_{1bn}$
2	$y_{211}, y_{212}, \dots, y_{21n}$	$y_{221}, y_{222}, \dots, y_{22n}$	…	$y_{2b1}, y_{2b2}, \dots, y_{2bn}$
⋮	⋮	⋮	⋮	⋮
a	$y_{a11}, y_{a12}, \dots, y_{a1n}$	$y_{a21}, y_{a22}, \dots, y_{a2n}$	…	$y_{ab1}, y_{ab2}, \dots, y_{abn}$

Since the experiment includes n replicates in each cell, there are a total of abn observations (experimental runs). The observations of the two-factor factorial can be described by the effects model

$$y_{ijk} = \mu + \tau_i + \beta_j + (\tau\beta)_{ij} + \varepsilon_{ijk} \begin{cases} i = 1, 2, \dots, a \\ j = 1, 2, \dots, b \\ k = 1, 2, \dots, n \end{cases} \tag{59}$$

where μ refers to the overall mean effect, τ_i is the effect at the i^{th} level of factor A, β_j is the effect at the j^{th} level of factor B, $(\tau\beta)_{ij}$ is the interaction effect and ε_{ijk} is the random error. Both factors are assumed to be fixed, i.e. the levels of the factor are controlled within the experiment. In addition, the factor and interaction effects are defined as deviation from the overall mean, so that

$$\sum_{i=1}^{a} \tau_i = 0, \sum_{j=1}^{b} \beta_i = 0, \text{and} \sum_{i=1}^{a} (\tau\beta)_{ij} = \sum_{j=1}^{b} (\tau\beta)_{ij} = 0 \tag{60}$$

To check for significance of the model effects, the following three hypotheses are tested in a two-way ANOVA approach

$$\begin{aligned} &H_0: \tau_1 = \tau_2 = \cdots = \tau_a = 0 \\ &H_1: \text{at least one } \tau_i \neq 0 \end{aligned} \tag{61}$$

for the factor A,

$$\begin{aligned} &H_0: \beta_1 = \beta_2 = \cdots = \beta_b = 0 \\ &H_1: \text{at least one } \beta_i \neq 0 \end{aligned} \tag{62}$$

for the factor B, and

$$\begin{aligned} &H_0: (\tau\beta)_{ij} = 0, \qquad \text{for all } i, j \\ &H_1: \text{at least one } (\tau\beta)_{ij} \neq 0 \end{aligned} \tag{63}$$

for the interaction between A and B.

Before giving some details about this hypothesis testing, a few more definitions concerning the

individual observations are required. Let $y_{i..}$ be the total of all observations at the i^{th} level of factor A, $y_{.j.}$ the total of all observations at the j^{th} level of factor B, $y_{ij.}$ the total of all observations at the ij^{th} cell and $y_{...}$ the total of all observations. $\bar{y}_{i..}$, $\bar{y}_{.j.}$, $\bar{y}_{ij.}$, and $\bar{y}_{...}$ refer to the corresponding averages.

$$\begin{aligned}
y_{i..} &= \sum_{j=1}^{b}\sum_{k=1}^{n} y_{ijk} \qquad \bar{y}_{i..} = \frac{y_{i..}}{bn} \qquad i = 1, 2, \dots, a \\
y_{.j.} &= \sum_{j=1}^{a}\sum_{k=1}^{n} y_{ijk} \qquad \bar{y}_{.j.} = \frac{y_{.j.}}{an} \qquad j = 1, 2, \dots, b \\
y_{ij.} &= \sum_{k=1}^{n} y_{ijk} \qquad \bar{y}_{ij.} = \frac{y_{ij.}}{n} \qquad i = 1, 2, \dots, a \qquad j = 1, 2, \dots, b \\
y_{...} &= \sum_{i=1}^{a}\sum_{j=1}^{b}\sum_{k=1}^{n} y_{ijk} \qquad \bar{y}_{...} = \frac{y_{...}}{abn}
\end{aligned} \tag{64}$$

The total variation of the experiment is expressed by the total sum of squares SS_{tot}.

$$SS_{\text{tot}} = \sum_{i=1}^{a}\sum_{j=1}^{b}\sum_{k=1}^{n} (y_{ijk} - \bar{y}_{...})^2 \tag{65}$$

It is composed of the sum of squares due to factor A (SS_A), the sum of squares due to factor B (SS_B), the sum of squares due to the interaction of A and B (SS_{AB}) and the sum of squares due to the error (SS_{err}).

$$SS_{\text{tot}} = SS_A + SS_B + SS_{AB} + SS_{\text{err}} \tag{66}$$

where

$$SS_A = nb \sum_{i=1}^{a} (\bar{y}_{i..} - \bar{y}_{...})^2 \tag{67}$$

$$SS_B = na \sum_{j=1}^{b} (\bar{y}_{.j.} - \bar{y}_{...})^2 \tag{68}$$

$$SS_{AB} = SS_{\text{tot}} - SS_{\text{err}} - SS_A - SS_B \tag{69}$$

$$SS_{\text{err}} = \sum_{i=1}^{a}\sum_{j=1}^{b}\sum_{k=1}^{n} (y_{ijk} - \bar{y}_{ij.})^2 \tag{70}$$

The mean sum of squares (MS_A, MS_B, MS_{AB}, MS_{err}) are calculated taking into account the respective degrees of freedom df. Thus, the sum of squares is weighted differently depending on the degrees of freedom. Assuming two factors that have the same contribution to explain the overall variability. It makes a difference if, for example, one factor requires 5 levels (df = 4) and the other only 2 (df = 1). Table 15 shows the degrees of freedom of the individual effects in a general two-factor factorial experiment.

Table 15: Degrees of freedom.

effect	degrees of freedom
factor A	$a-1$
factor B	$b-1$
interaction AB	$(a-1)(b-1)$
error	$ab(n-1)$
total	$abn-1$

If H_0 applies and if we assume that the effect model is adequate, i.e. that the error terms ε_{ijk} are independent and normally distributed with constant variance σ^2, each ratio of mean squares MS_A/MS_{err}, MS_B/MS_{err} and $MS_{AB}/MS_{\mathrm{err}}$ is $F_{f1,f2}$ distributed. The F-distribution (Fisher-distribution) depends on the degrees of freedom of the factor (f_1) and the error (f_2). It allows to determine the probability of finding an F-value that is at least as high as the one found when the corresponding effect does not exist (H_0 is true). This probability is expressed by the p-value. If the p-value is smaller than a previously chosen significance level α, H_0 can be rejected and a significant effect is assumed. Table 16 shows the structure of a two-way ANOVA table.

Table 16: Structure of a two-way analysis of variance (ANOVA) table.

source of variation	sum of squares	degrees of freedom	mean squares	F-ratio
factor A	SS_A	$a-1$	MS_A	MS_A/MS_{err}
factor B	SS_B	$b-1$	MS_B	MS_B/MS_{err}
interaction AB	SS_{AB}	$(a-1)(b-1)$	MS_{AB}	MS_{AB}/MS_{err}
error	SS_{err}	$ab(n-1)$	MS_{err}	
total	SS_{tot}	$abn-1$		

Refine Response Model

The decision of which effect should be included in a response model is a very challenging part. This process is often referred as model selection or model refinement. Typically, some kind of regression subset selection procedure is used to determine the most appropriate model [36]. Two common approaches are the sequential forward selection and the sequential backward elimination.

The sequential forward selection starts with a simple basic model which usually contains only the constant term β_0 (overall mean). Subsequently, the model is extended with new terms in an iterative process. In each step, any term not yet included is added to the current model and the improvement of the model quality is determined. The term which leads to the largest improvement of the model quality is then added to the response model. The extension of the

response model ends when a given model quality is achieved or no significant improvement is achieved anymore.

In contrast to the sequential forward selection, the sequential backward elimination starts from a response model that already contains all available model terms, e.g. a full linear model including interactions as given in equation 40. Each iteration consists of deleting the term whose removal leads to the highest possible improvement of the quality criterion.

An alternative to stepwise regression is to search across all possible models to find subsets of factors that yield a good model based on some criteria. However, this approach is only feasible if the number of factors is moderate due to high computational effort and memory requirements. [34]

Based on planning and analysing of many experiments, three regularities in the relationships among factor and interaction effects have been detected, namely effect sparsity, hierarchical ordering and effect heredity. These regularities are often considered while carrying out the modelling process. The effect sparsity refers to the observation that the number of important effects in a factorial experiment is usually small. The hierarchical ordering principle states that on average the main effects tend to be larger than two-factor interactions and two-factor interactions tend to be larger than three-factor interactions and so on. And finally the effect heredity implies that for an interaction to be significant, at least one of its included factors must be significant. [39]

A common requirement of regression models is to be hierarchical. A hierarchal model requires factors which are involved in higher order interaction terms to be included also the lower order terms, even if they are not significant. For example, if the interaction AB is significant, both main effects A and B must be included in the model. However, hierarchy is not an absolute principle which must be followed in any case [41]. More details regarding the different model selection approaches can be found in [34].

One commonly used criterion to measure the quality of a fitted model is the R^2-value, or coefficient of multiple determination. It gives the percentage of the total variation that is explained by the underlying model.

$$R^2 = 1 - \frac{SS_{\mathrm{err}}}{SS_{\mathrm{tot}}} \tag{71}$$

Thus, R^2 is always between 0 and 1. In general, the higher the R^2 the better the model fits the data coming from the experiment. The more parameters included in a model, the less space is left for the error and thus R^2 increases. If the fitted model has too many parameters compared to the number of observations, the model can get overfitted. An overfitted regression model includes the random error in the estimation of the functional relationship between the response and factors. Hence, it fails to predict future observations reliably. Therefore, R^2 alone is not a suitable criterion for assessing the quality of different model variants, especially if they are of different sizes.

An extension of R^2 helps to deal with this problem. The adjusted R^2 takes into account the number of parameters included in a model.

$$R_{adj}^2 = 1 - (1 - R^2)\frac{n-1}{n-p-1} \quad (72)$$

where n refers to the sample size (number of runs) and p denotes for the number of model parameter excluding the intercept term β_0.

There is a large number of other criteria for assessing the quality of the model, such as AIC, BIC, C_P. Depending on the application, different criteria can be beneficial. For more information see [34].

Model Adequacy Checking

Before drawing conclusions from ANOVA, the adequacy of the underlying model should be checked [41]. The underlying assumptions of the ANOVA are independent and normally distributed error terms with constant variance. Simple graphical tools can be used to check whether these assumptions are valid.

To check whether the experimental error terms are independent, a simple scatter plot of the residuals versus the run order can be created. If this plot shows any obvious pattern, e.g. increasing, decreasing or cyclic zones, it can be assumed that the randomization has not compensated for all disturbances. The normality of the experimental errors can be checked through a normal probability plot of the residuals. If the residuals fall along a straight line, the error terms can be assumed to be normally distributed. A scatter plot of residuals versus factor levels can show whether the variability at each level of the factor is approximately equivalent. Differences in the variability of residuals between factor levels are often due to higher variability in larger responses. This can be checked in a scatter plot showing the residuals over the predicted values. [36]

Once the adequacy of the model is confirmed, it can either be used for further analysis of the main and interaction effects or passed to a subsequent optimization approach.

2.7 Multiple Response Optimization – The Desirability Function Approach

Once response models are available, the optimisation procedure can follow. The desirability function approach from [19] is a simple approach for the simultaneous optimization of several responses. Therefore, each individual response y_i is converted into a standardized desirability value d_i over the range [0,1]. $d_i = 1$ corresponds to the target value (most desirable) while $d_i = 0$ is outside the acceptable region (not desirable). The desirability function gives the functional relationship between a response and the corresponding desirability value. They can be classified in three categories: (i) larger-the-better, which targets to maximize a response; (ii) smaller-the-better, which targets to minimize a response; and (iii) nominal-the-better, which targets a specific response value. Fig. 39 shows the shapes of the three different desirability function categories. The mathematical formulations of these functions are given in equation 73, 74 and 75, respectively. By choosing the exponent $r = 1$, the desirability function is linear. Choosing $r > 1$ puts more emphasis on being close to the target value, while choosing $0 < r < 1$ does the opposite.

$$d_i = \begin{cases} 0 & y_i \leq y_{i,\min} \\ \left(\dfrac{y_i - y_{i,\min}}{y_{i,\max} - y_{i,\min}}\right)^r & y_{i,\min} \leq y_i \leq y_{i,\max} \\ 1 & y_i > y_{i,\max} \end{cases} \tag{73}$$

$$d_i = \begin{cases} 1 & y_i \leq y_{i,\min} \\ \left(\dfrac{y_{i,\max} - y_i}{y_{i,\max} - y_{i,\min}}\right)^r & y_{i,\min} \leq y_i \leq y_{i,\max} \\ 0 & y_i > y_{i,\max} \end{cases} \tag{74}$$

$$d_i = \begin{cases} 0 & y_i \leq y_{i,\min} \\ \left(\dfrac{y_i - y_{i,\min}}{y_{i,\text{target}} - y_{i,\min}}\right)^{r_1} & y_{i,\min} \leq y_i \leq y_{i,\text{target}} \\ \left(\dfrac{y_{i,max} - y_i}{y_{i,\max} - y_{i,\text{target}}}\right)^{r_2} & y_{i,\text{target}} \leq y_i \leq y_{i,\max} \\ 0 & y_i > y_{i,\max} \end{cases} \tag{75}$$

Subsequently, the individual desirability values are combined in the overall desirability D

$$D = (\prod_{i=1}^{k} d_i)^{\frac{1}{k}} \tag{76}$$

where k is the number of individual desirability values. This overall desirability can be optimized by any optimization algorithm [52]. However, to increase the chance of finding the global instead of a local optimum, several optimization trials should be performed at random start values of the involved factors.

The drawback of this simple approach is that the shape of the desirability functions influences the final solution. This final solution is considered optimal, although there could be alternative solutions with almost identical or at least acceptable responses that are preferable, e.g. due to the factor values.

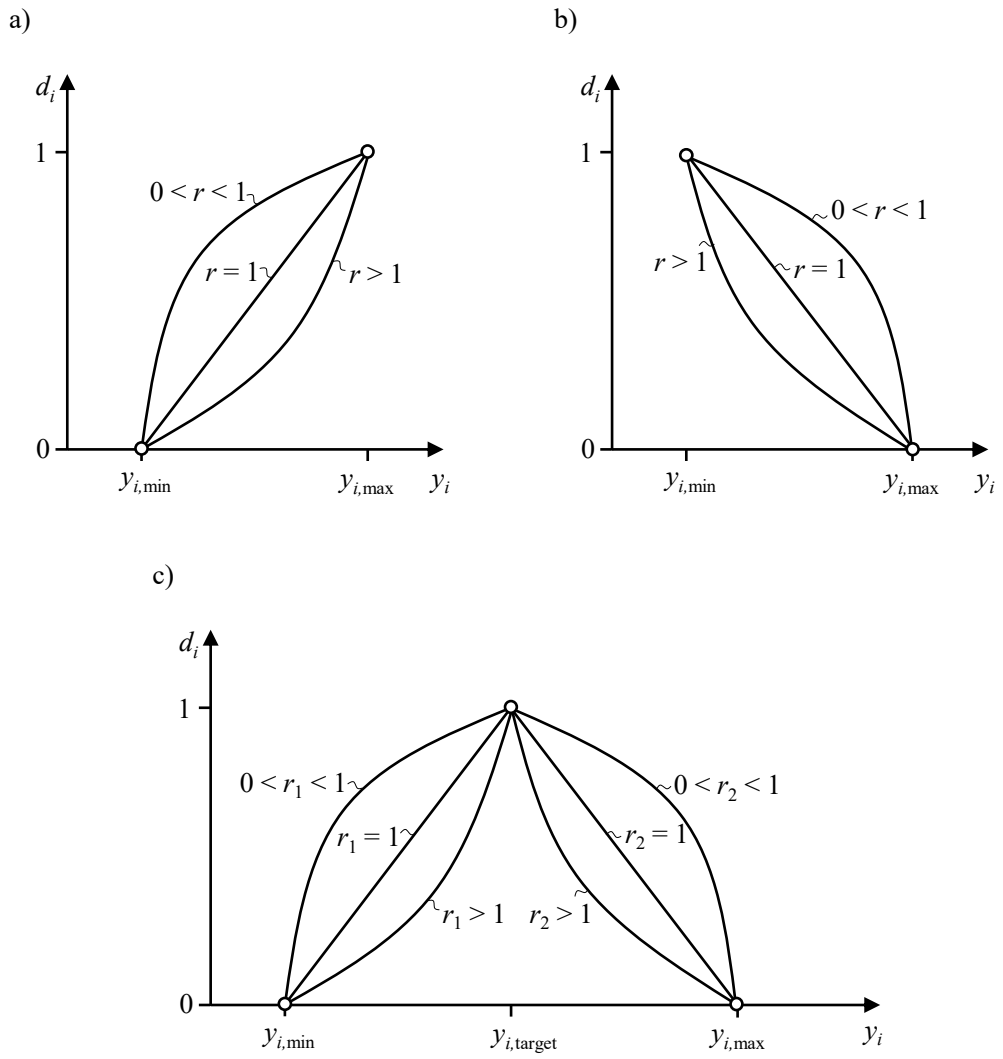

Fig. 39: Different categories of desirability functions, a) larger-the-better, b) smaller-the-better and c) nominal-the-better.

3 Surrogate Model Based Design Optimization of MASV

The main content of this section originates from [21], where the majority of the work was carried out by Andreas Egger. The contribution of the co-authors consisted in supporting the experimental setup, determining the valve parameters, i.e. the $\mu\sigma$-values based on 3d-CFD, and proofreading. The writing itself was solely conducted by Andreas Egger.

It can be assumed that the initial design of the MASV does not utilize the full potential to increase the COP, cooling capacity and reliability of the compressor. Thus, the MASV design has been optimized based on a multi-response optimization approach.

3.1 Optimization Approach

Fig. 40 shows the overall outline of the optimization approach. After the functionality of the MASV had been confirmed in initial design tests, it was considered more feasible to carry out the design optimisation on the basis of an in-house compressor simulation model according to [1], which was adapted and validated with measurement results from the initial design tests. Relevant independent variables (factors) and dependent variables (responses) had to be determined for the optimization study. In the following step, response models (surrogate models) of all optimization relevant responses were generated using a design of experiments (DOE) approach. Finally, all response models were combined in one objective function to enable multi-response optimization with a conventional optimization algorithm in MATLAB [60].

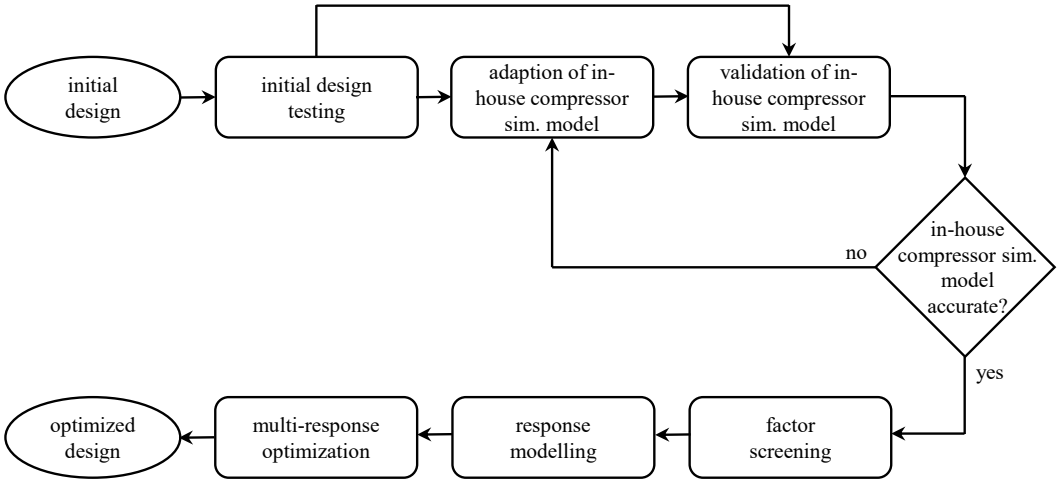

Fig. 40: Overall outline of optimization approach.

3.2 Compressor Simulation Model

3.2.1 Modelling

The underlying study is about a first optimization round of a novel valve system. Due to the novelty of the system and the associated lack of system knowledge, a large number of potentially relevant system factors were identified. A large number of factors require a large number of simulations to obtain the response models used for the multi-response optimization. Furthermore, the focus is not on the detailed examination of local phenomena, but on the optimization of the valve dynamics in order to improve the COP, cooling capacity and reliability of the compressor. For these reasons, a computationally intensive 3d approach was not

considered appropriate.

An existing in-house transient compressor simulation model based on [1] forms the basis for the design optimization. The model combines a 0d representation of the cylinder and a sequence of 1d pipes and 0d volumes that represent the remaining gas line of the compressor. Several adaptations of the model were necessary to correspond to the compressor considered in this study. In addition to the adaption of the geometry data such as suction muffler volumes, stroke volume, etc., the $\mu\sigma$-values of suction and discharge valve had to be determined. The $\mu\sigma$-value represents a dimensionless flow coefficient which is widely used in valve modelling. It allows to consider significant 3d flow effects when calculating the mass flow in the compressor simulation model based on the Saint-Venant equation for a theoretical isentropic flow, see equation 77 and equation 78. The $\mu\sigma$-value combines the flow coefficient μ, which expresses the flow resistance, and σ, which gives the ratio of the actual free flow area to the maximum possible flow area through the valve. A more detailed description of the $\mu\sigma$-value can be found in [45]. The determination of the $\mu\sigma$-values for suction and discharge valve was carried out based on 3d-CFD simulations including a 3d-FEM valve model. The $\mu\sigma$-values for suction and discharge valve are given in Fig. 41 and Fig. 42 respectively. In the case of the suction valve, the $\mu\sigma$-value only depends on the valve lift, whereas in the case of the discharge valve it depends on the valve lift and the piston position, as the piston nose influences the flow channel through the discharge port.

$$\dot{m} = A_{\mathrm{eff}}\, p_{\mathrm{u}} \sqrt{\frac{2}{R\, T_{\mathrm{u}}}} \sqrt{\frac{\kappa}{\kappa - 1}\left[\left(\frac{p_{\mathrm{d}}}{p_{\mathrm{u}}}\right)^{\frac{2}{\kappa}} - \left(\frac{p_{\mathrm{d}}}{p_{\mathrm{u}}}\right)^{\frac{\kappa+1}{\kappa}}\right]} \tag{77}$$

$$A_{\mathrm{eff}} = \mu\sigma\, \pi\, \frac{d_{\mathrm{v}}^2}{4} \tag{78}$$

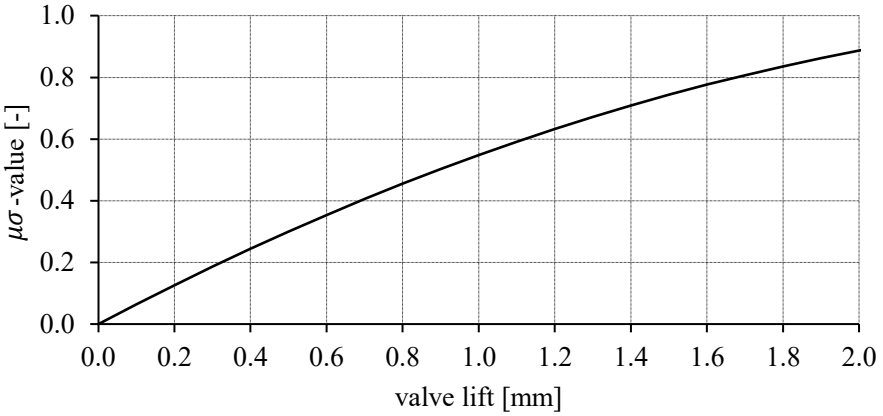

Fig. 41: $\mu\sigma$-value of the suction valve.

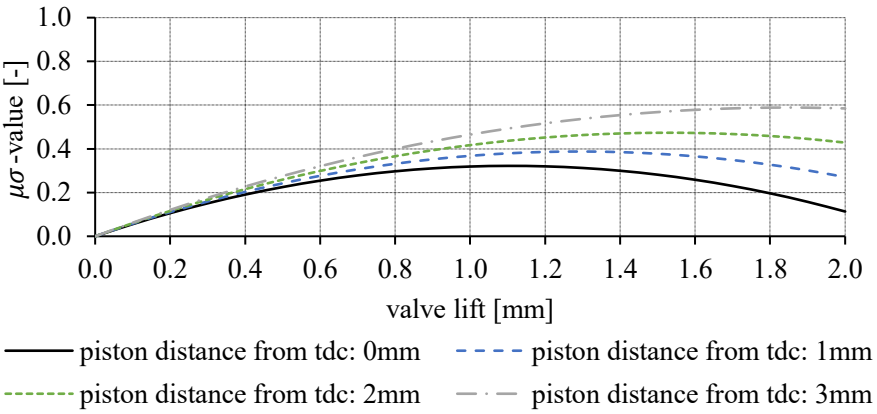

Fig. 42: $\mu\sigma$-value of the discharge valve.

The next important step was to model and implement the mechanism of the MASV. A common reed valve modelling approach is based on a simple single degree-of-freedom spring-damper-mass system. The first important work on this topic was presented by [17]. In the meantime the approach has been adopted and extended by various researchers, for example in [27] or [2]. The basic mathematical formulation of this approach is given in equation 79.

$$m_{\text{eff}}\,\ddot{x} + d\,\dot{x} + c\,x = F_{\text{gas}} + F_{\text{other}} \tag{79}$$

where m_{eff} is the effective mass of the valve which is calculated based on the stiffness c and the first natural frequency f_0 of the valve according to equation 80. The selection of the effective mass ensures that the natural frequency of the spring-damper-mass system is equal to the first natural frequency of the valve. x, $\dot{x}$ and $\ddot{x}$ represent the valve lift, valve velocity and valve acceleration. d refers to the damping coefficient and c refers to the stiffness of the valve. The term F_{gas} on the right side of equation 79 describes the gas force which actuates the reed valve and F_{other} combines all other forces i.e., the valve preload force and the oil sticking force.

$$m_{\text{eff}} = \frac{1}{4\,\pi^2}\,\frac{c}{{f_0}^2} \tag{80}$$

$$F_{\text{c}} = s_{\text{c}}\,[c_{\text{c}}\,(x_2 - x_3 - \Delta x_{23,0}) + \, d_{\text{c}}\,(\dot{x}_2 - \dot{x}_3)] \tag{81}$$

$$s_{\text{c}} = \begin{cases} 1 \; if \; (x_2 - x_3 - \Delta x_{23,0}) > 0 \\ 0 \; else \end{cases} \tag{82}$$

$$\sum F_x = m\,\ddot{x} \tag{83}$$

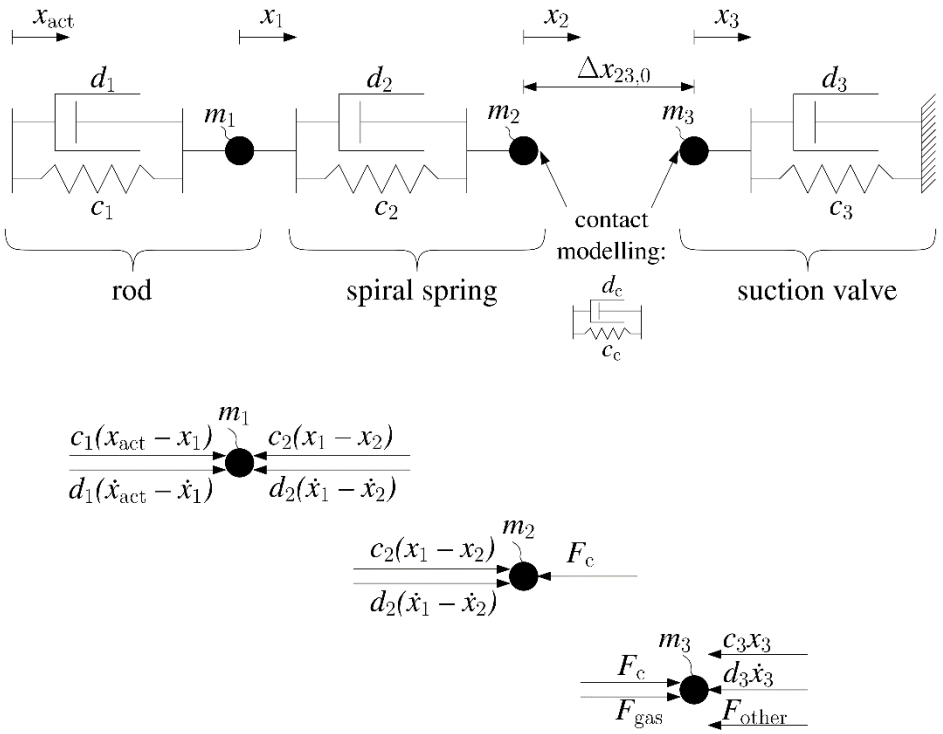

Fig. 43: 1d model of the MASV.

$$\dot{\boldsymbol{X}}(t) = \begin{bmatrix} \dot{x}_1 \\ \dot{x}_2 \\ \dot{x}_3 \\ \ddot{x}_1 \\ \ddot{x}_2 \\ \ddot{x}_3 \end{bmatrix}$$

$$= \begin{bmatrix} 0 & 0 & 0 & 1 & 0 & 0 \\ 0 & 0 & 0 & 0 & 1 & 0 \\ 0 & 0 & 0 & 0 & 0 & 1 \\ \frac{-c_1 - c_2}{m_1} & \frac{c_2}{m_1} & 0 & \frac{-d_1 - d_2}{m_1} & \frac{-d_2}{m_1} & 0 \\ \frac{c_2}{m_2} & \frac{-c_2 - s_c\, c_c}{m_2} & \frac{s_c\, c_c}{m_2} & \frac{d_2}{m_2} & \frac{-d_2 - s_d\, d_c}{m_2} & \frac{s_d\, d_c}{m_2} \\ 0 & \frac{s_c\, c_c}{m_3} & \frac{-s_c\, c_c - c_3}{m_3} & 0 & \frac{s_d\, d_c}{m_3} & \frac{-s_d\, d_c - d_3}{m_3} \end{bmatrix} \begin{bmatrix} x_1 \\ x_2 \\ x_3 \\ \dot{x}_1 \\ \dot{x}_2 \\ \dot{x}_3 \end{bmatrix} + \begin{bmatrix} 0 \\ 0 \\ 0 \\ \frac{c_1\, x_{act} + d_1\, \dot{x}_{act}}{m_1} \\ \frac{s_c\, c_c\, \Delta x_{23,0}}{m_2} \\ \frac{F_{gas} - F_{other} - s_c\, c_c\, \Delta x_{23,0}}{m_1} \end{bmatrix} \tag{84}$$

In addition to the suction reed valve, the MASV mechanism must be modelled. Fig. 43 shows the model of the entire MASV, a multi-body system consisting of the three components rod, spiral spring and suction valve. Since the spiral spring is not permanently in contact with the valve, a contact model based on a simple spring-damper element has been included. Equation 81 gives the mathematical formulation of the contact force F_c where s_c refers to the contact switch according to equation 82 to limit the contact to compressive forces. The dynamic balance of forces according to equation 83 of each of the point masses leads to a second order inhomogeneous linear differential equation system (DES). The second order DES can be transformed into the first order DES in equation 84 by means of the state vector $\boldsymbol{X}(t) = [x_1\ x_2\ x_3\ \dot{x}_1\ \dot{x}_2\ \dot{x}_3]^{\mathrm{T}}$. This first order DES has been implemented into the in-house compressor simulation model where it is solved based on the 4th order Runge-Kutta approach. The system parameters of equation 84, i.e. the stiffness coefficients and the masses of the three components were determined on the basis of physical experiments and finite element analysis. Both contact parameters as well as the damping coefficients of the three components were selected for a satisfactory fit of simulation and measurement results.

3.2.2 Validation

Once the adaption of the compressor simulation model was completed, the valve dynamics of the MASV was validated with measurement data. A schematic of the measurement setup is shown in Fig. 44. Table 17 summarizes the specifications of the measuring instruments used for the valve dynamics measurements.

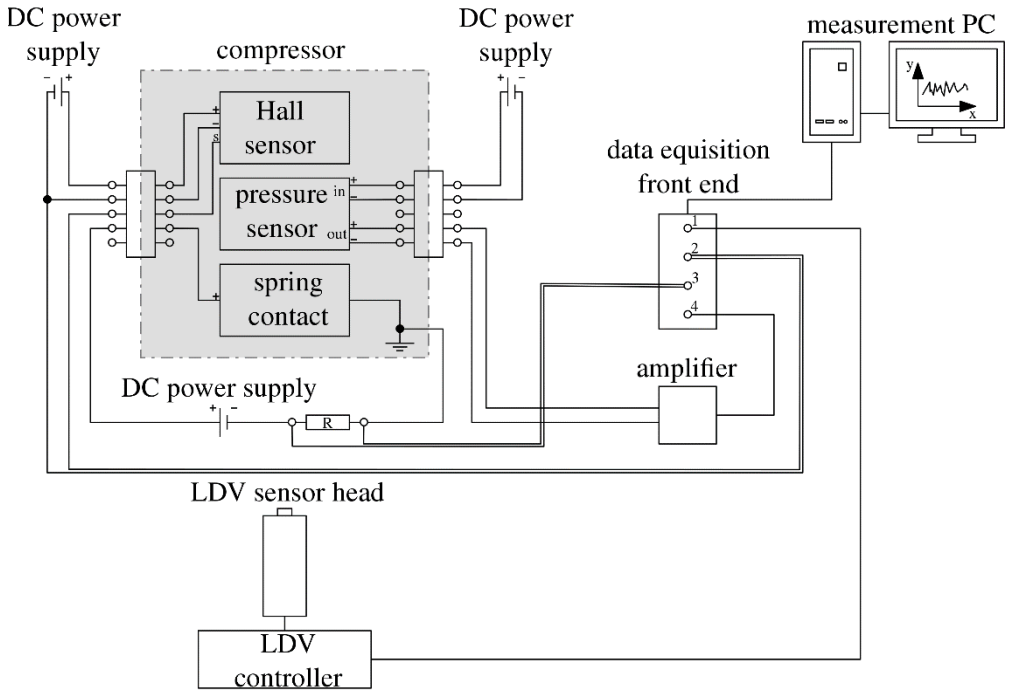

Fig. 44: Measurement setup of valve dynamics measurement.

Table 17: Specifications of measuring instruments.

device	name	range	uncertainty
pressure sensor	Kulite XTL-HA123C-190	0 - 0.17 MPa	± 2 % FS
Hall effect sensor	Honeywell SS496A1	0 - 2.5 V	± 3 % FS
LDV	OFV-5000	0 - 5 m s^{-1}	± 1.77 % FS
data acquisition front end	Brüel&Kjaer Pulse-3560-B-130	0 - 10 V	± 0.17 % FS

The valve velocity was measured with a laser Doppler vibrometer (LDV), which is a measurement device for measuring vibrations and velocities of moving surfaces using a laser beam that is directed towards the measuring object. LDV enables contactless valve velocity measurements where the valve dynamics is not distorted by the measurement device. Since the compressor is operated in a hermetically sealed environment with R600a, a pipe has been installed which leads from the suction muffler neck to the outside of the compressor shell. An acrylic plate attached at one end of the pipe ensures that the laser beam can reach the valve surface while at the same time the compressor remains hermetically sealed, see Fig. 45. The measured velocity signal was averaged over 100 cycles in order to increase the quality of the signal. The valve lift was determined by further processing of the mean velocity according to equation 85.

$$x_{3,j+1} - x_{3,j} = \int_{j}^{j+1} v_3(t)\,\mathrm{d}t \approx \frac{\left(v_{3,j+1} + v_{3,j}\right)}{2} * \Delta t_{\mathrm{samp}} \tag{85}$$

Where x_3 is the valve lift and v_3 is the valve velocity at the centre of the suction valve, j and $j+1$ describe two consecutive time steps and Δt_{samp} represents the measurement sampling time.

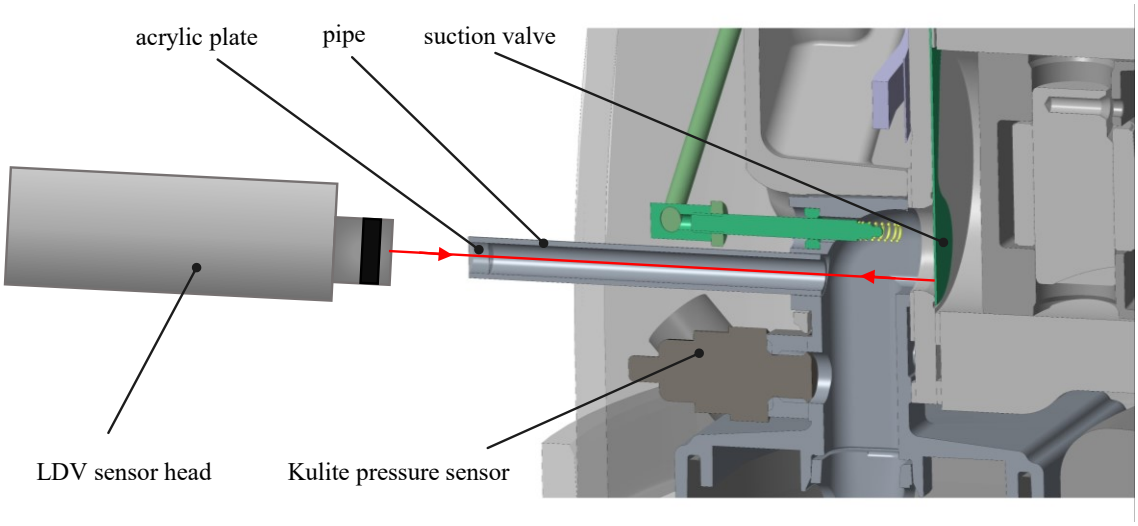

Fig. 45: Suction valve lift measurement concept using LDV.

A Kulite absolute pressure sensor was installed in the suction muffler neck to measure the suction pressure. To monitor the contact behaviour between the spiral spring and the suction valve, a contact measurement was included into the measurement setup. It is based on a simple electrical circuit which consists of a voltage source and an ohmic resistor. If contact between

spiral spring and suction valve occurs, the electrical circuit is closed and a voltage drop across the resistor can thus be measured. A Hall effect sensor was used to relate the measurement signals to the crank angle position. The sensor was attached to the crank case while a neodymium magnet was integrated into the counterweight of the crank shaft. Each time the magnet passes the Hall effect sensor, a peak signal can be detected. At a sampling rate of 65.5 kHz and a compressor speed of 3000 rpm, the maximum error of the detected crank angle is approx. ± 0.27 °ca.

The validation of the simulation model with measurements is given in Fig. 46 - Fig. 49. It turns out, that the simulation agrees very well with the measurements. The validation results also provide a good insight into valve dynamics of the initial design. Fig. 46 shows the suction valve lift as well as the motion of the non-deformed end of the spiral spring. If the non-deformed end of the spiral spring is ahead of the valve position, the spiral spring is compressed and thus a supporting force is applied to the valve. The intermediate valve closing near 150 °ca must be avoided in order to utilize the full potential of the MASV. Furthermore, the duration of one valve oscillation cycle is very long in relation to the duration of the suction phase. This may lead to valve closing delays at some operating conditions.

Fig. 47 shows the suction valve velocity over the crank angle position. A valve impact is indicated by a steep gradient of the valve velocity curve. The max. valve impact velocity is located near 210 °ca.

Fig. 48 illustrates the simulated spiral spring deformation and the measured contact between spiral spring and suction valve over the crank angle position. A comparison of both lines indicates, that the contact timing can be captured very well. It turns out, that there is no permanent contact between spiral spring and valve during the suction phase.

Fig. 49 shows a comparison of simulated and measured pressure at the suction muffler neck over the crank angle position, which also fits very well.

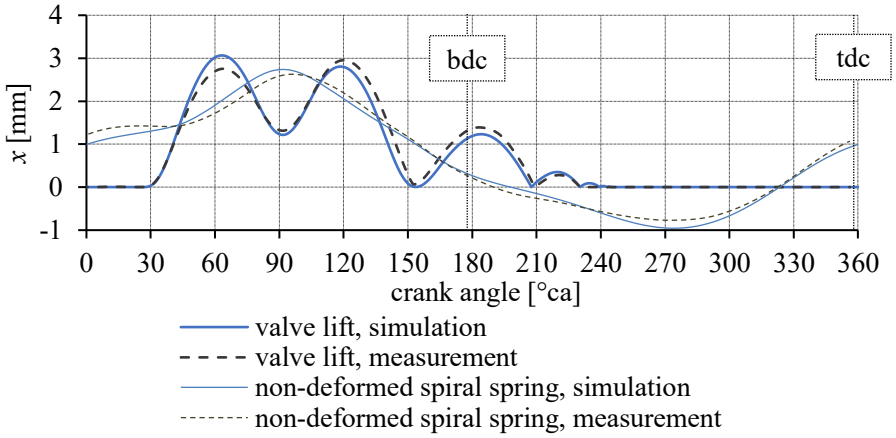

Fig. 46: Validation of suction valve and non-deformed spiral spring motion (T_{evap} = − 23.3 °C, T_{cond} = 45 °C, T_{amb} = T_{sub} = T_{sup} = 32.2 °C, $n_{comp,n}$ = 4000 rpm, R600a).

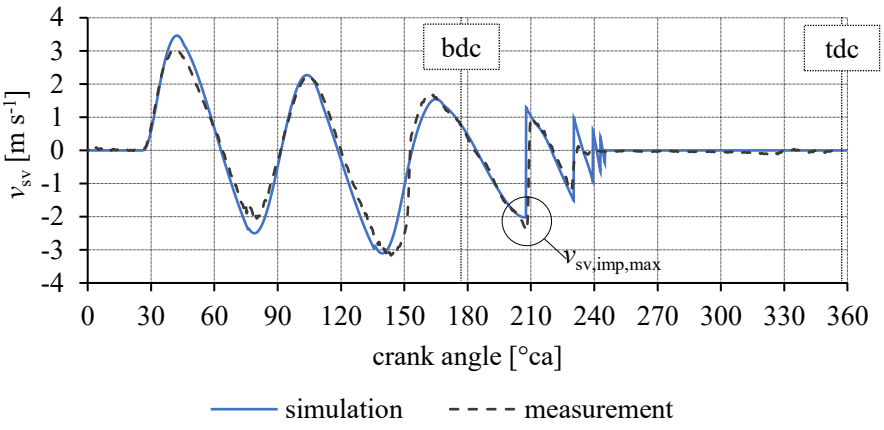

Fig. 47: Validation of suction valve velocity (T_{evap} = − 23.3 °C, T_{cond} = 45 °C, T_{amb} = T_{sub} = T_{sup} = 32.2 °C, $n_{comp,n}$ = 4000 rpm, R600a).

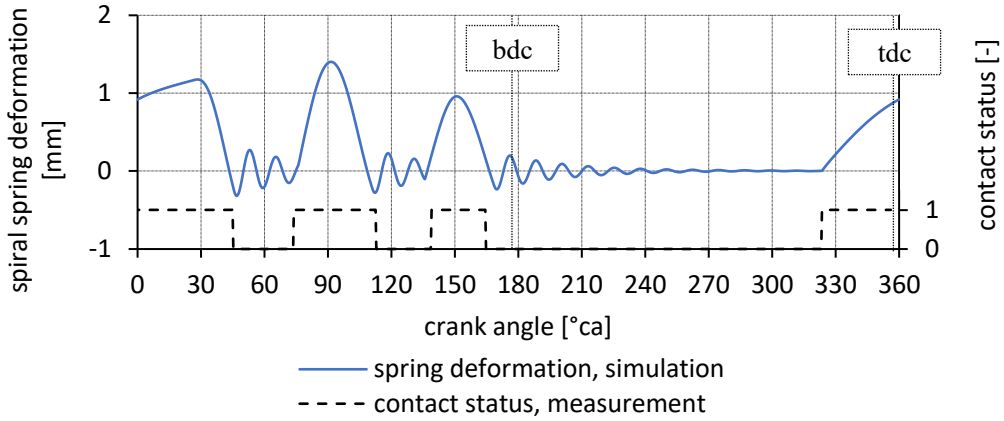

Fig. 48: Validation of spiral spring contact timing (T_{evap} = − 23.3 °C, T_{cond} = 45 °C, T_{amb} = T_{sub} = T_{sup} = 32.2 °C, $n_{comp,n}$ = 4000 rpm, R600a).

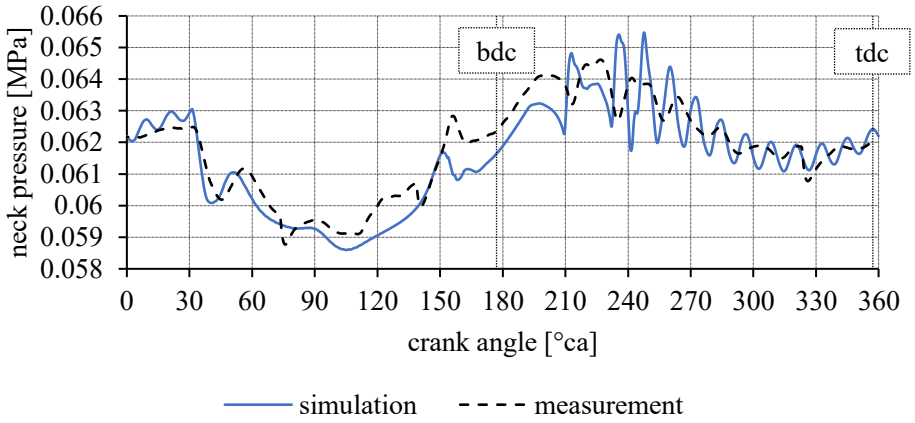

Fig. 49: Validation of suction muffler neck pressure (T_{evap} = − 23.3 °C, T_{cond} = 45 °C, T_{amb} = T_{sub} = T_{sup} = 32.2 °C, $n_{comp,n}$ = 4000 rpm, R600a).

3.3 Response Models

A response model describes the mathematical relationship between one dependent variable (response) and several independent variables (factors). This mathematical relationship will be obtained via a multiple regression analysis based on the results of a designed experiment.

3.3.1 Experimental Unit

The selected experimental unit forms the basis of the response models and can be either physical or virtual (e.g. simulation model). One advantage of a simulation-based experimental unit is that factor levels can be changed almost arbitrarily and with little effort. A further advantage of a simulation-based experimental unit is that no measurement uncertainties are involved in the experiments, which simplifies the creation of appropriate response models. However, an accurate simulation model is a prerequisite for the selection of a simulation-based experimental unit. It was considered reasonable to proceed with the compressor simulation model described in section 3.2 as experimental unit.

3.3.2 Selection of Responses and Factors

Fig. 50 gives an overview of the selected responses and factors. The selected responses must correspond to the optimization targets which are to increase COP, cooling capacity and reliability of the compressor. To increase COP and cooling capacity, suction losses as well as gas backflow due to valve closing delays must be reduced. Therefore, the two responses suction work and suction mass per cycle were selected as response variables. To account for the reliability, the maximal suction valve impact velocity was selected as third response.

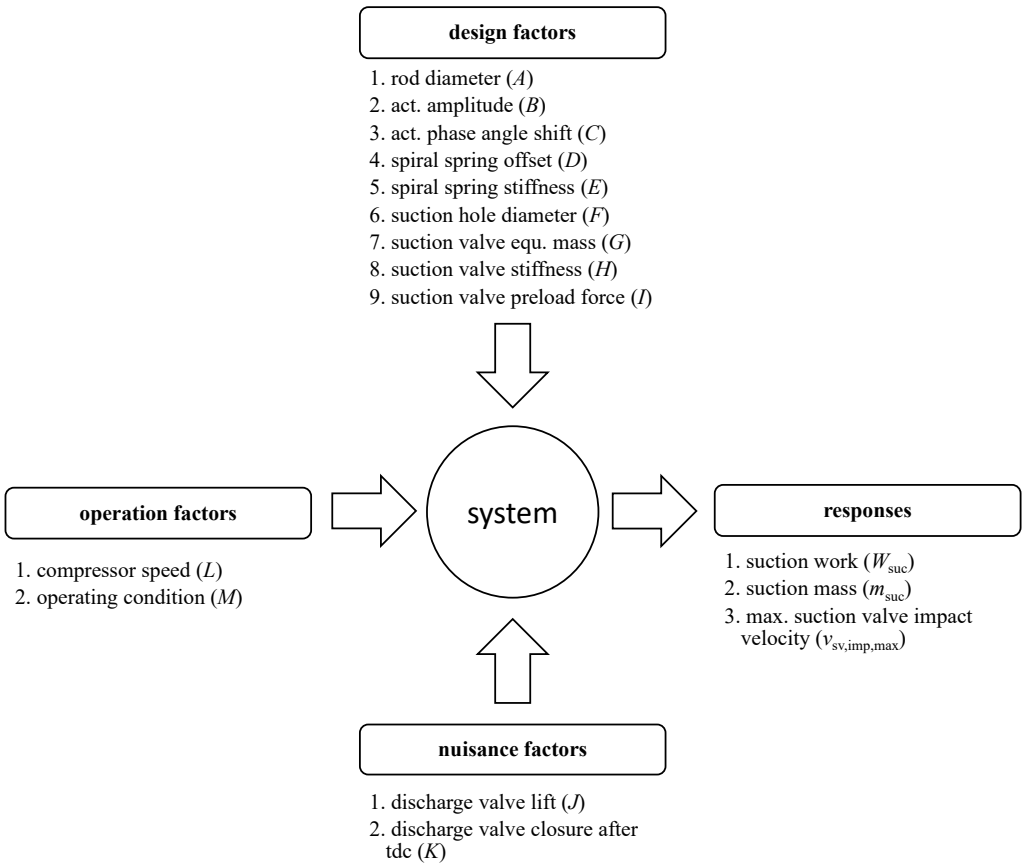

Fig. 50: Overview of optimization relevant system factors and responses.

Factors are system parameters which change their levels within the DOE approach. They form a carefully selected subset of the entire system parameter list. The selected factors are classified into three groups, the design factors, the nuisance factors and the operation factors. The design factors represent the MASV design and can be optimized to achieve the optimization targets. Fig. 51 shows the corresponding geometric design factors. The nuisance factors may significantly affect the responses, but are not part of the MASV design and the operation factors represent the operation point of the compressor.

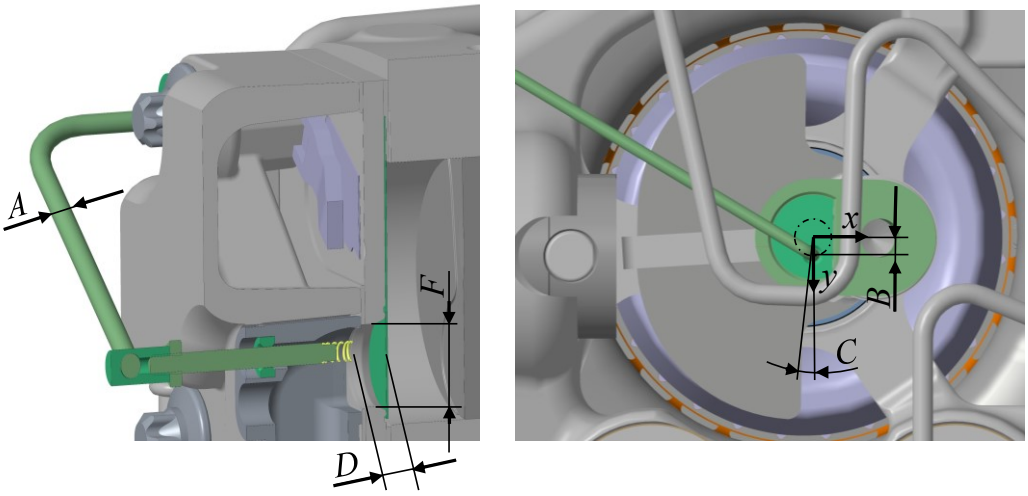

Fig. 51: Geometric design factors of MASV.

3.3.3 Factor Screening

A two-level factor screening experiment based on a PB20 experimental design (see section 2.6.3) was conducted to estimate factor effects and to check for a reduction of the initially selected factor set. Table 18 shows the included factors and their corresponding factor levels. To investigate the influence of the discharge valve dynamics on the responses, the discharge valve lift and closing point were included as factors.

Fig. 52 to Fig. 54 show the main effect plots of the three responses max. valve impact velocity, suction work and suction mass. It turned out, that the compressor speed has by far the largest effect on the max. valve impact velocity and the suction work (Fig. 52 and Fig. 53). In the case of the suction mass, the discharge valve closing point has a similar strong effect as the compressor speed, see Fig. 54.

Fig. 55 to Fig. 57 show the main effect diagrams separately for low and high compressor speeds, which allows to examine the differences in factor effects between low and high compressor speeds. As illustrated in Fig. 55, the max. valve impact velocity at low compressor speed is generally very small with the individual factors having little influence. At high compressor speed, however, the max. valve impact velocity is much higher with the factors C (actuation phase angle shift) and K (discharge valve closure after tdc) having the largest effect. The same applies to the suction work in Fig. 56, where the factor effects at low compressor speed are also smaller than at high compressor speed. The suction mass in contrast, show large factor effects at low and high compressor speed, see Fig. 57. The factor effect of H (suction valve stiffness) has one of the highest magnitudes and acts in a different direction at low and high compressor speed, i.e. increasing the factor level from −1 to +1 increases the suction mass at low compressor speed, whereas it reduces the suction mass at high compressor speed.

Table 18: Factors and factor levels considered for factor screening.

				level	
nr.	label	factor name	unit	low (−)	high (+)
1	A	rod diameter	mm	2	3
2	B	actuation amplitude	mm	1.5	2.5
3	C	actuation phase angle shift	°ca	−15	15
4	D	spiral spring offset	mm	0	1
5	E	spiral spring stiffness	N mm^{-1}	1	2
6	F	suction hole diameter	mm	8	10
7	G	suction valve equivalent mass	g	0.10	0.16
8	H	suction valve stiffness	N mm^{-1}	0.15	0.35
9	I	suction valve preload force	N	0.07	0.21
10	J	discharge valve lift	mm	1.5	2
11	K	discharge valve closure after tdc	°ca	0	10
12	L	compressor speed	rpm	1500	5000
13	M	operating condition	°C	− 23.3 / 45	− 23.3 / 55

The factor screening helps to better understand the system behaviour. However, since the design factor effects are of similar magnitude and the effects act in different directions, a significant reduction of the initially selected factor set was not possible without risking to miss important factors for the design optimization. It seems that the optimal design only can be achieved by adjusting many factors with small effects rather than by a few with large effects.

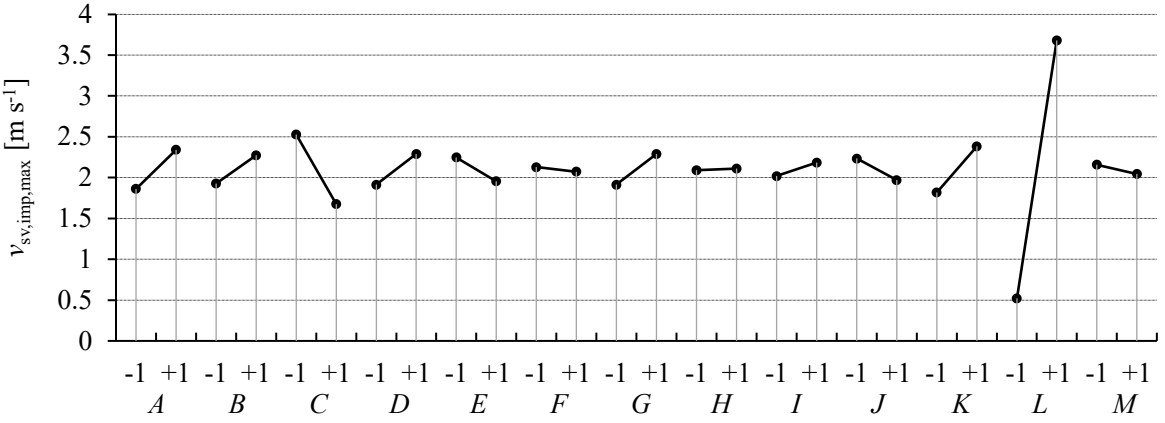

Fig. 52: Main effect plot of the response $v_{sv,imp,max}$.

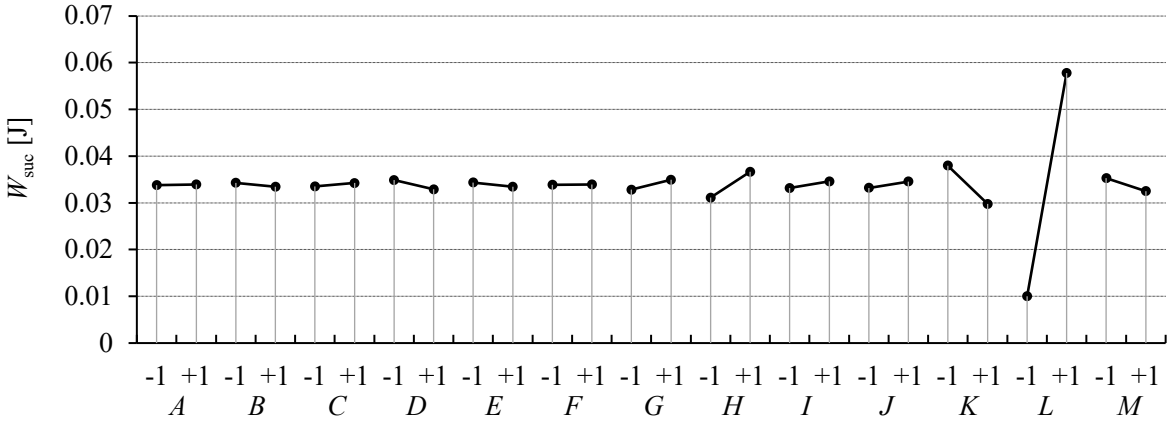

Fig. 53: Main effect plot of the response W_{suc}.

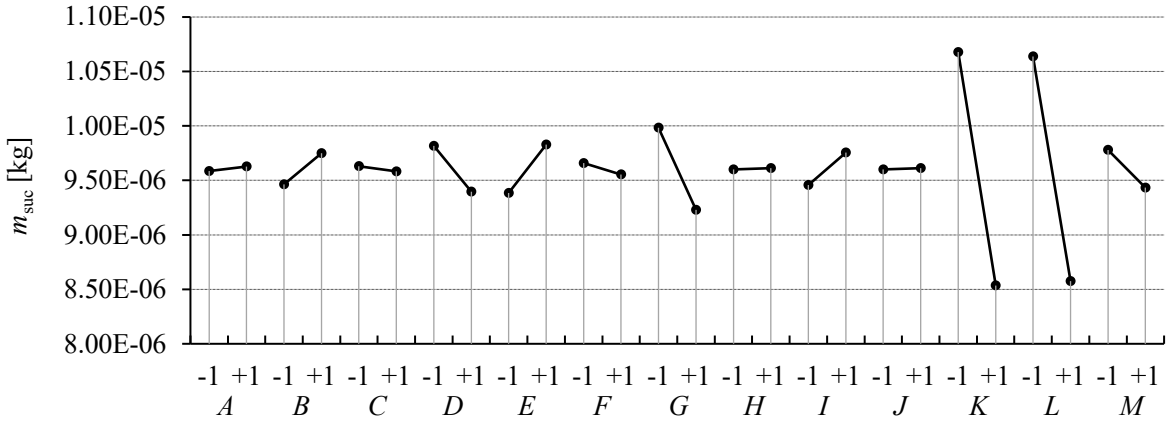

Fig. 54: Main effect plot of the response m_{suc}.

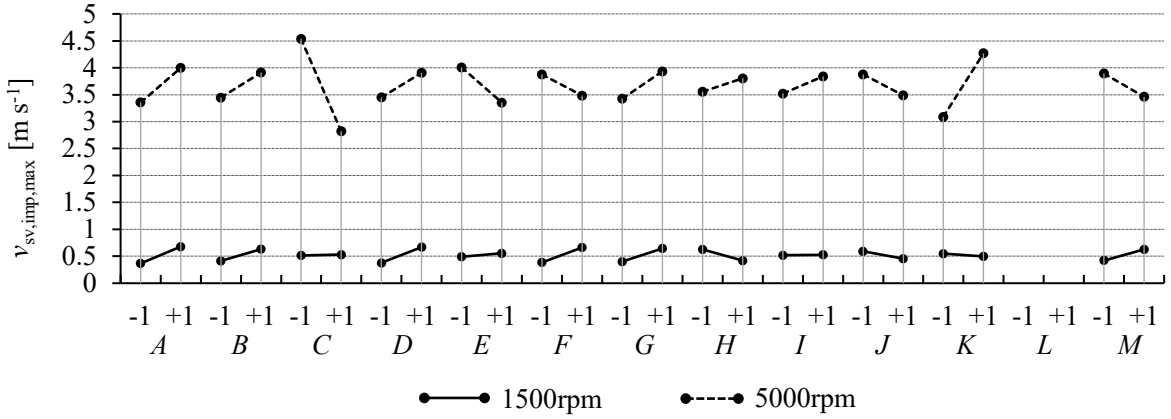

Fig. 55: Main effect plot of the response $v_{sv,imp,max}$ at low and high compressor speed.

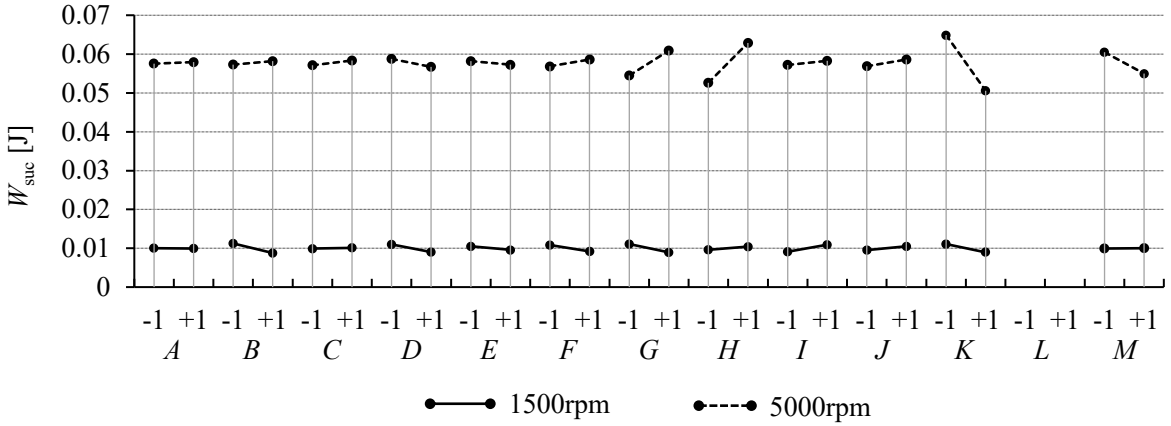

Fig. 56: Main effect plot of the response W_{suc} at low and high compressor speed.

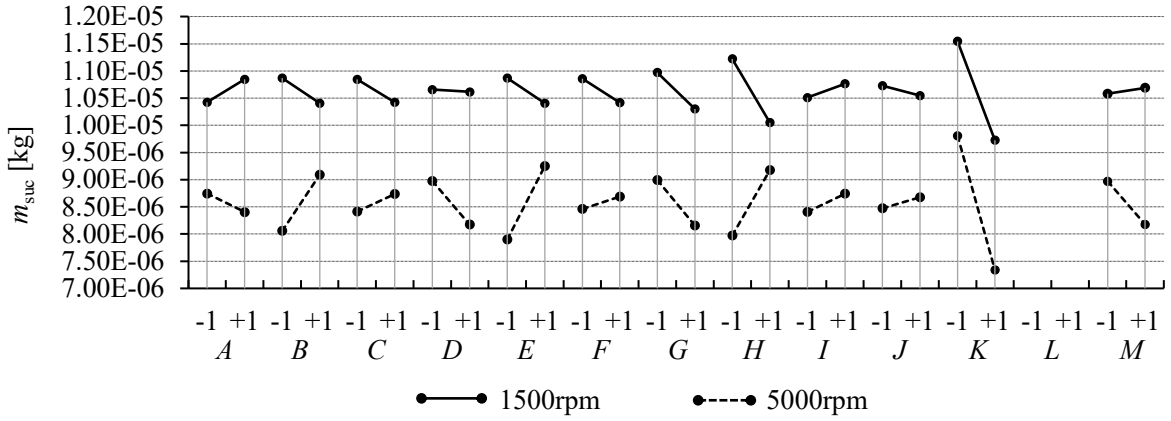

Fig. 57: Main effect plot of the response m_{suc} at low and high compressor speed.

3.3.4 Modelling

Due to the high number of relevant factors, a DSD (see section 2.6.3) was selected as experimental design to derive the relationship between factors and responses. Since the compressor speed has a very large effect on all three responses, separate response models for low (1500 rpm) and high (5000 rpm) compressor speed based on a DSD with 11 factors were created. The operating condition was set at − 23.3 °C / 45 °C, which is a good representation for the actual operating condition of the compressor in a cooling device. Table 19 shows the 11 factors and their corresponding low, medium and high factor levels. The experimental design was created with the daewr package [37] in Rstudio [49].

Table 19: Factors and factor levels considered for response modelling.

				level		
nr.	label	factor name	Unit	low	medium	high
1	A	rod diameter	mm	2	2.5	3
2	B	actuation amplitude	mm	1.5	2	2.5
3	C	actuation phase angle shift	°ca	0	10	20
4	D	spiral spring offset	mm	0	0.5	1
5	E	spiral spring stiffness	N mm^{-1}	1	1.5	2
6	F	suction hole diameter	mm	8	9	10
7	G	suction valve equivalent mass	g	0.1	0.13	0.16
8	H	suction valve stiffness	N mm^{-1}	0.15	0.25	0.35
9	I	suction valve preload force	N	0.07	0.14	0.21
10	J	discharge valve lift	mm	1.5	1.75	2
11	K	discharge valve closure after tdc	°ca	0	5	10

After the simulation experiment was carried out, a stepwise regression approach, as proposed by [33], was used to create the response models. The number of steps did not exceed 1/3 to 1/2 of the number of runs to avoid over-fitting. A total of five different response models were created. The responses suction work and suction mass were modelled at low and high compressor speed while the max. suction valve impact velocity was only modelled at high compressor speed.

All five models are displayed in coded factor units in equation 86 to equation 90. Coded factor units allow a direct comparison of the model coefficients due to the common scale of the factors. The relationship between coded and natural factor units is given in equation 38.

The model statistics of the response models (ANOVA) is shown in Table 20. Depending on the model, 88 % to 99 % of the response variance can be explained by the included factors. The values of the adjusted R^2 are of similar magnitude as the R^2, which is a good indicator that an appropriate number of factors are included in the models.

The predicted vs. actual plots illustrated in Fig. 58 indicate a good fit of all five response models. In addition, the model adequacy (see section 2.6.4) has been checked based on plots showing the normal probability of the residuals, residuals versus run order and residual versus predicted response. All five response models were found to be adequate.

Table 20: Response model statistics.

model	std. Err.	R^2	R^2_{adj}	F-statistics	p-value
$W_{\mathrm{suc,1500rpm}}$	5.74×10^{-4}	0.93	0.89	20.6	2.72×10^{-6}
$W_{\mathrm{suc,5000rpm}}$	1.96×10^{-3}	0.96	0.94	50.2	2.77×10^{-9}
$m_{\mathrm{suc,1500rpm}}$	1.18×10^{-7}	0.99	0.98	132.9	7.28×10^{-12}
$m_{\mathrm{suc,5000rpm}}$	3.15×10^{-7}	0.95	0.93	43.6	7.47×10^{-9}
$v_{\mathrm{sv,imp,max,5000rpm}}$	2.25×10^{-1}	0.88	0.83	16.1	6.23×10^{-6}

$$W_{\mathrm{suc,1500rpm}} = 1.01\times10^{-2} - 8.52\times10^{-4}\,B - 8.32\times10^{-4}\,K + 8.25\times10^{-4}\,C + 6.34\times10^{-4}\,B\,D - 6.20\times10^{-4}\,K\,C - 4.34\times10^{-4}\,D + 3.53\times10^{-4}\,H - 3.40\times10^{-4}\,B\,C + 2.46\times10^{-4}\,I \quad (86)$$

$$W_{\mathrm{suc,5000rpm}} = 5.99\times10^{-2} - 7.33\times10^{-3}\,K - 3.54\times10^{-3}\,D - 2.31\times10^{-3}\,B - 2.14\times10^{-3}\,E + 1.42\times10^{-3}\,C + 1.28\times10^{-3}\,H - 1.12\times10^{-3}\,E\,A \quad (87)$$

$$m_{\mathrm{suc,1500rpm}} = 1.13\times10^{-5} - 8.11\times10^{-7}\,K - 4.95\times10^{-7}\,K^2 - 4.10\times10^{-7}\,D - 2.54\times10^{-7}\,C + 1.58\times10^{-7}\,E\,H + 7.84\times10^{-8}\,H\,A + 7.38\times10^{-8}\,I - 5.87\times10^{-8}\,E \quad (88)$$

$$m_{\mathrm{suc,5000rpm}} = 8.90\times10^{-6} - 9.10\times10^{-7}\,K - 5.86\times10^{-7}\,G + 4.92\times10^{-7}\,H - 2.54\times10^{-7}\,A - 2.45\times10^{-7}\,D + 1.97\times10^{-7}\,I + 1.67\times10^{-7}\,E \quad (89)$$

$$v_{\mathrm{sv,imp,max,5000rpm}} = 3.18 - 0.38\,H - 0.23\,E + 0.21\,F + 0.20\,H\,G + 0.17\,B + 0.15\,D + 0.12\,A \quad (90)$$

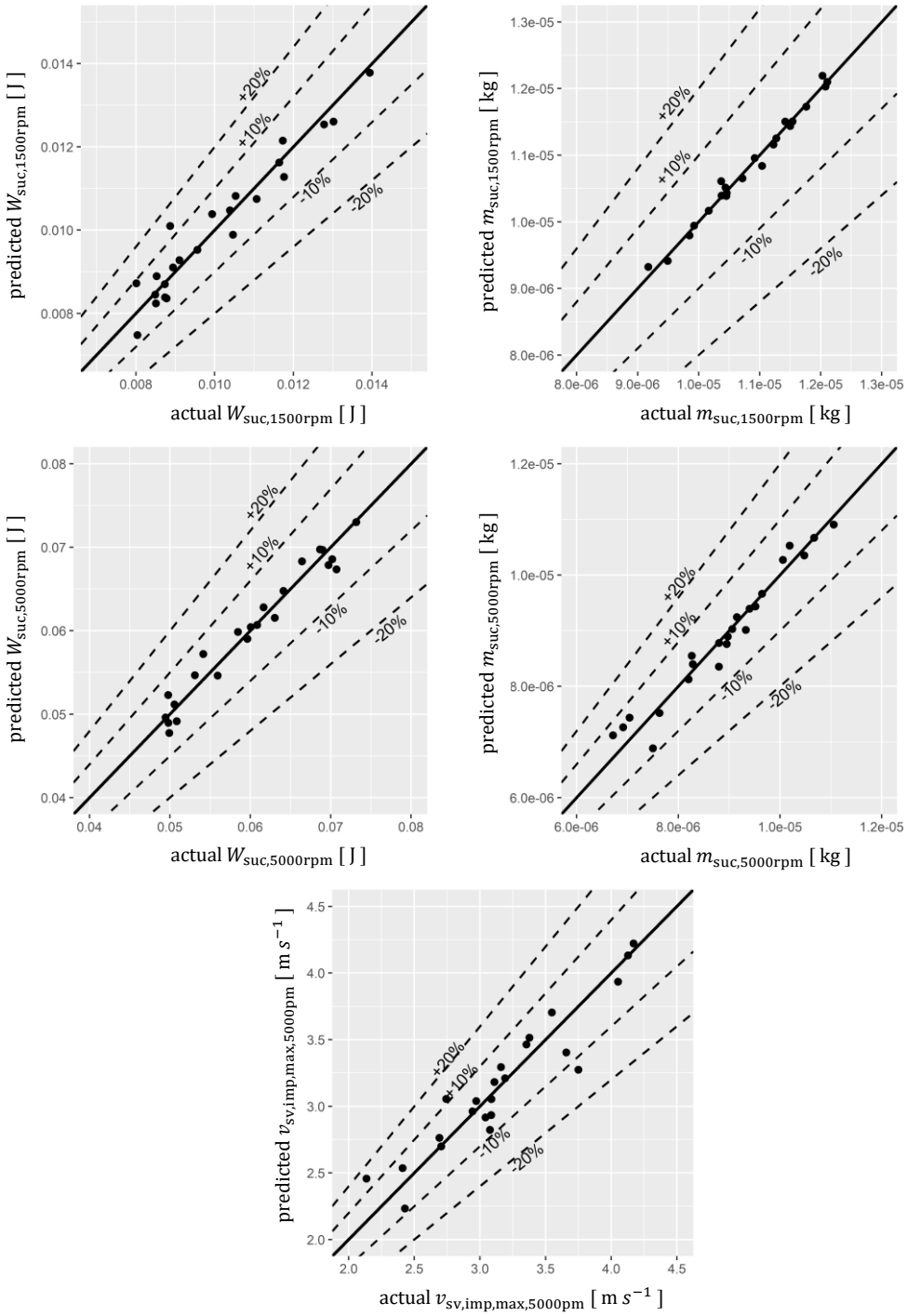

Fig. 58: Predicted (response model) vs. actual (compressor simulation model) responses based on training data set.

3.3.5 Validation

To finally check for the prediction capabilities of the created response models, a validation with a new data set was carried out. In a total of 20 runs, each of the 11 factors was simulated at 20 different and randomly selected levels between −1(low level) and +1 (high level). A comparison of the predicted (response models) and the actual (compressor simulation model) responses is given in Fig. 59.

In general, the predictions of the responses suction work and suction mass are in a very good

agreement with the simulation results. Most of them are within a range of ±10 %, despite intermediate factor levels, which were not considered in the response modelling process.

The prediction accuracy of the max. suction valve impact velocity is lower. Due to the strong nonlinearity of the max. suction valve impact velocity, a more accurate prediction would require a more complex modelling approach. However, most of the predictions were made within an accuracy of ± 20 % and the response model is able to describe a general trend. Thus, all response models are considered to be suitable for the subsequent multiple-response optimization.

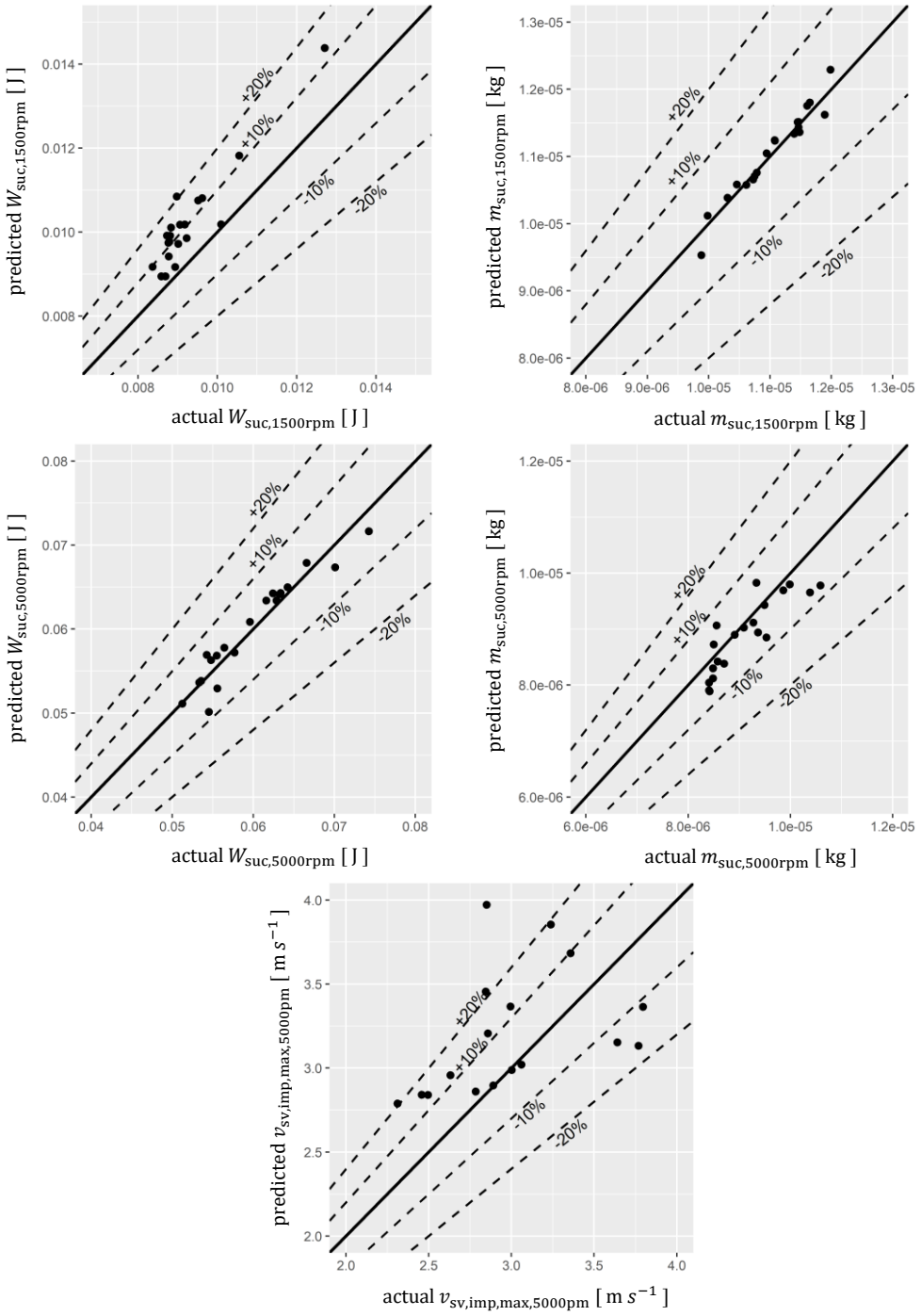

Fig. 59: Predicted (response model) vs. actual (compressor simulation model) responses based on validation data set.

3.4 Multiple Response Optimization

The desirability function approach based on [28] was selected to combine multiple quantitative responses in one quantity. Each individual response is converted into a desirability value between 0 and 1, the former being undesirable and the latter most desirable, using a linear desirability function given by an exponent r = 1 (see section 2.7).

The limits for the calculation of the individual desirability values are given in Table 21. The upper limit of the max. suction valve impact velocity must not exceed 4 m s^{-1} due to reliability reasons, while the lower limit corresponds to a realistic target value to improve the reliability and acoustics of the compressor. The limits of the remaining responses were selected based on the response range observed during the response modelling experiments.

The overall desirability is obtained by the calculation of the geometric mean of the individual desirability values according to equation 76. If a single individual desirability value is zero, the overall desirability is also zero. Thus, an undesirable individual response is avoided. The fmincon-function from the Optimization Toolbox [60] in MATLAB [59] was used to optimize the overall desirability. To verify that the global- or best local maximum has been found, several optimization runs at random factor start values were conducted.

Table 21: Response limits of the individual desirability functions.

response y_i	unit	min	max
$W_{\mathrm{suc,1500rpm}}$	J	0.008	0.015
$W_{\mathrm{suc,5000rpm}}$	J	0.04	0.08
$m_{\mathrm{suc,1500rpm}}$	kg	8×10^{-6}	1.4×10^{-5}
$m_{\mathrm{suc,5000rpm}}$	kg	6×10^{-6}	1.3×10^{-5}
$v_{\mathrm{sv,imp,max,5000rpm}}$	m s^{-1}	2	4

The multi-response optimization was performed based on two different optimization scenarios. In the first scenario (var.1), all design factors are adjustable while in the second scenario (var.2 – var.4) some design factors are fixed, as reported in Table 22. The optimization domain of the adjustable design factors is limited by the validity of the response models given by the low and high factor levels shown in Table 19. The fixed design factors represent different valve designs that can be easily implemented based on the current compressor design and common valve sheet thicknesses. The nuisance factors J (discharge valve lift) and K (discharge valve closure after tdc) were held constant at their midlevel in all variants.

Table 22: Design factor constraints of design optimization variants.

nr.	label	factor name	var. 1	var. 2	var. 3	var. 4
1	A	rod diameter	adjustable	adjustable	adjustable	adjustable
2	B	actuation amplitude	adjustable	adjustable	adjustable	adjustable
3	C	actuation phase angle shift	adjustable	adjustable	adjustable	adjustable
4	D	spiral spring offset	adjustable	adjustable	adjustable	adjustable
5	E	spiral spring stiffness	adjustable	adjustable	adjustable	adjustable
6	F	suction hole diameter	adjustable	fixed[1)]	adjustable	adjustable
7	G	suction valve equ. mass	adjustable	fixed[1)]	fixed[2)]	fixed[3)]
8	H	suction valve stiffness	adjustable	fixed[1)]	fixed[2)]	fixed[3)]
9	I	suction valve preload force	adjustable	fixed[1)]	adjustable	adjustable

[1)] value corresponds to the standard suction valve (thickness of 0.20 mm)

[2)] value corresponds to a valve with the shape of the standard suction valve and a thickness of 0.25 mm

[3)] value corresponds to a valve with the shape of the standard suction valve and a thickness of 0.15 mm

3.5 Results

The design factor levels of the optimized design variants are given in Table 23. The obtained values of the adjustable factors are located at the boundary of the optimization domain in each optimized design variant. This emphasizes a clear adjustment direction for an improved mechanism design, independent of the investigated suction valve.

Table 23: Design factor levels of optimized design variants.

nr.	label	factor name	unit	var. 1	var. 2	var. 3	var. 4
1	A	rod diameter	mm	2	2	2	2
2	B	actuation amplitude	mm	2.5	2.5	2.5	2.5
3	C	actuation phase angle shift	°ca	0	0	0	0
4	D	spiral spring offset	mm	0	0	0	0
5	E	spiral spring stiffness	N mm^{-1}	2	2	2	2
6	F	suction hole diameter	mm	8	8	8	8
7	G	suction valve equivalent mass	g	0.1	0.16	0.2	0.12
8	H	suction valve stiffness	N mm^{-1}	0.35	0.23	0.45	0.1
9	I	suction valve preload force	N	0.21	0.15	0.21	0.21

Simulations between 1500 rpm and 5000 rpm were carried out for each of the four optimized design variants, as well as for the initial design and the standard design. Fig. 60 – Fig. 62 show the simulation results of the three responses suction work, suction mass and max. suction valve impact velocity as a function of compressor speed.

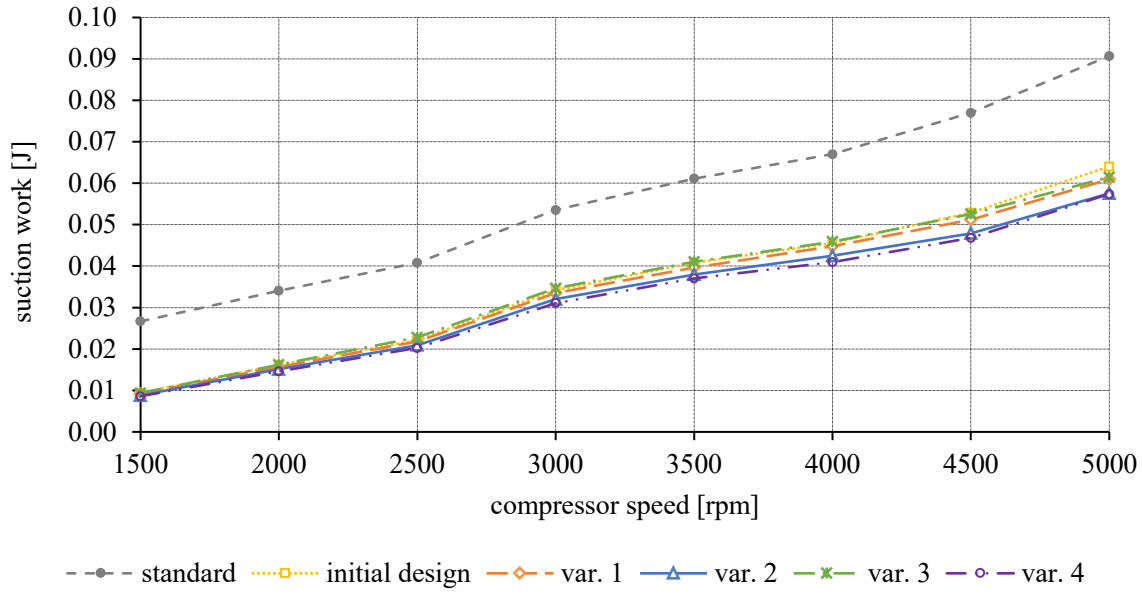

Fig. 60: Simulation results of the response suction work as a function of the compressor speed (T_{evap} = − 23.3 °C, T_{cond} = 45 °C). Results are presented for all four optimization variants (var. 1 to var. 4), the initial design and the standard valve.

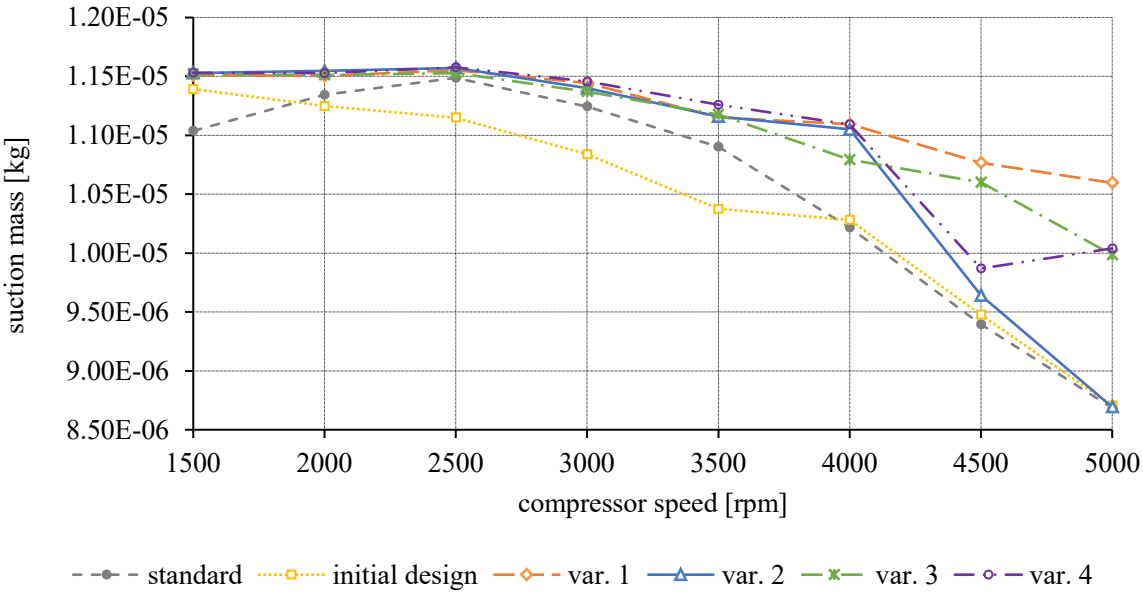

Fig. 61: Simulation results of the response suction mass as a function of the compressor speed (T_{evap} = − 23.3 °C, T_{cond} = 45 °C). Results are presented for all four optimization variants (var. 1 to var. 4), the initial design and the standard valve.

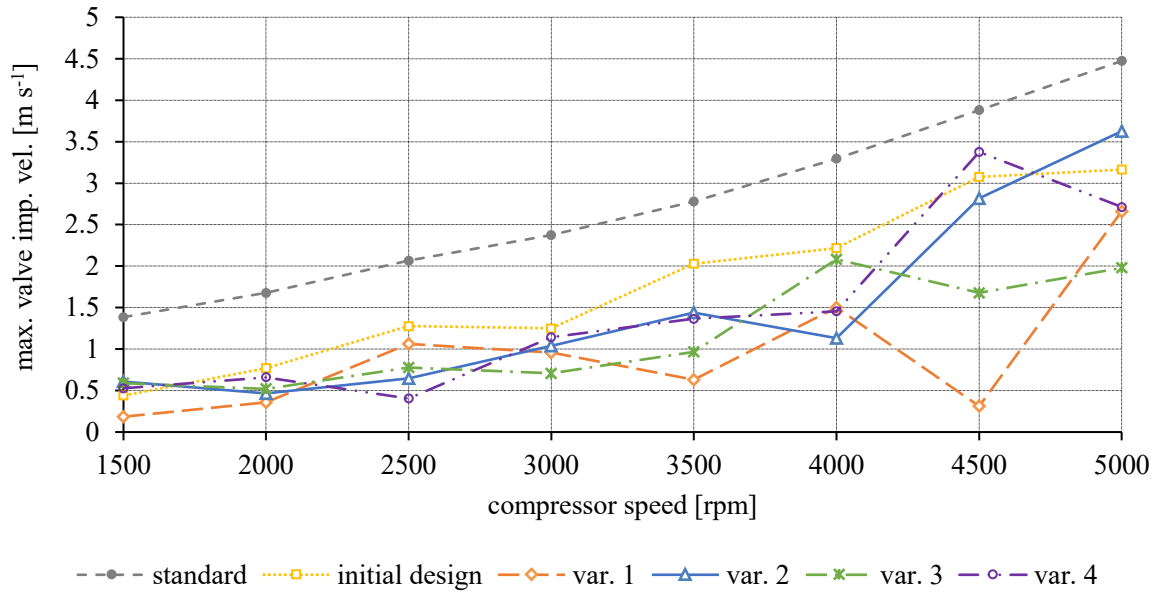

Fig. 62: Simulation results of the response max. valve impact velocity as a function of the compressor speed (T_{evap} = − 23.3 °C, T_{cond} = 45 °C). Results are presented for all four optimization variants (var. 1 to var. 4), the initial design and the standard valve.

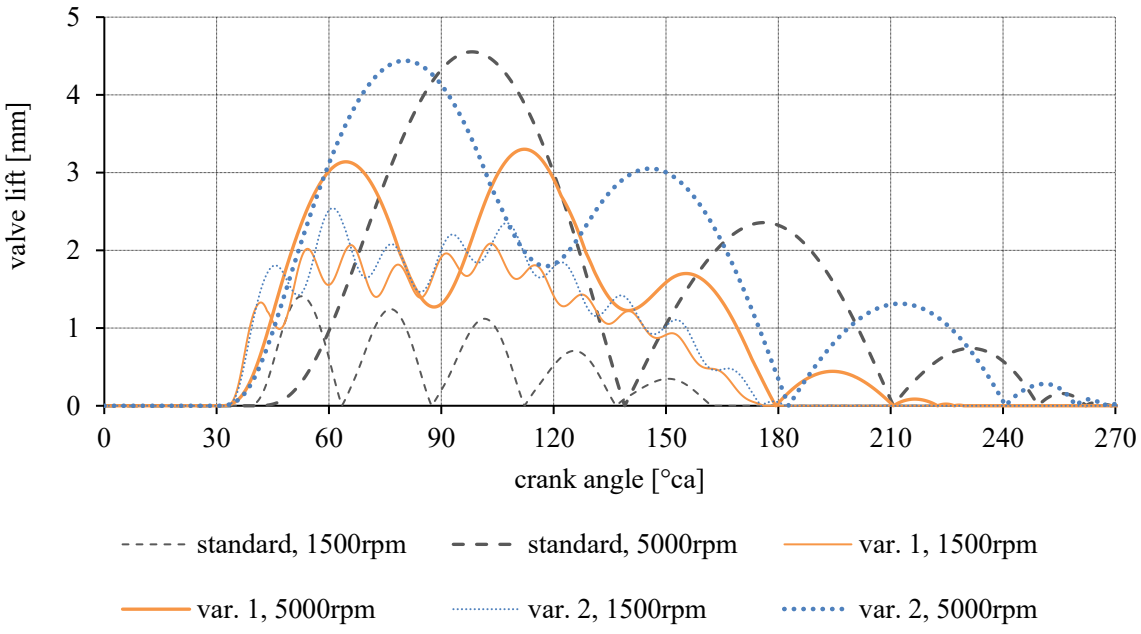

Fig. 63: Simulation results of the valve lift as a function of the crank angle (T_{evap} = − 23.3 °C, T_{cond} = 45 °C). Results are presented for design var. 1, var. 2 and the standard valve at minimum and maximum compressor speed.

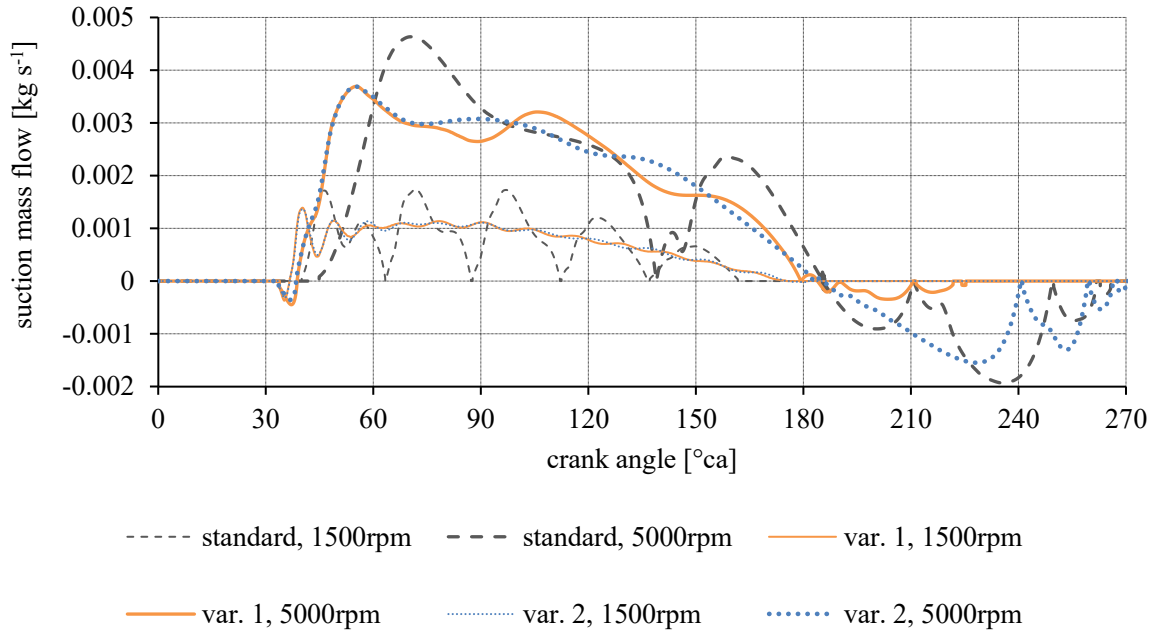

Fig. 64: Simulation results of the suction mass flow as a function of the crank angle (T_{evap} = − 23.3 °C, T_{cond} = 45 °C). Results are presented for design var. 1, var. 2 and the standard valve at minimum and maximum compressor speed.

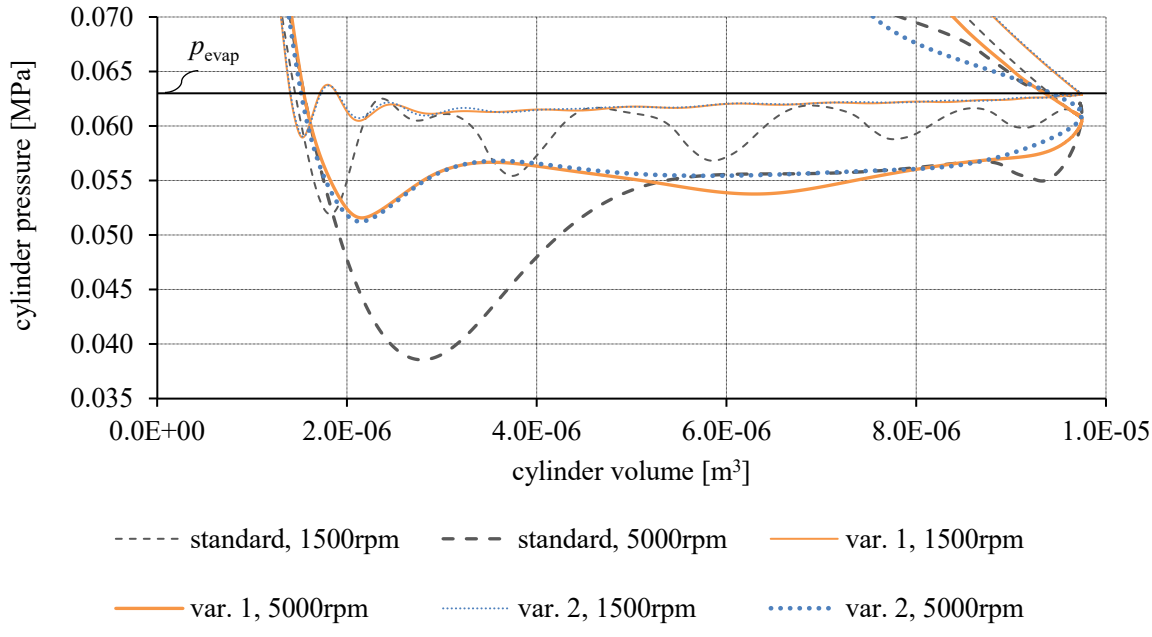

Fig. 65: Simulation results of the cylinder pressure as a function of the cylinder volume (T_{evap} = − 23.3 °C, T_{cond} = 45 °C). Results are presented for design var. 1, var. 2 and the standard valve at minimum and maximum compressor speed.

The suction work of all MASV design variants is significantly lower compared to the standard valve, while the difference between the individual variants is small. This reduced suction work of the MASV is due to the lower pressure loss of the suction process, which can be seen in Fig. 65. The enclosed area between the evaporating pressure and the cylinder pressure corresponds to the suction work. The higher the compressor speed, the lower the relative reduction of the suction work, as the flow losses through the suction port increase.

The suction mass shows larger differences between the individual variants, see Fig. 61. The optimized design variants show significantly better results than the standard valve and the initial design. The higher the compressor speed, the greater the differences between the individual variants. The best results over the entire compressor speed range are obtained by var. 1. At 5000 rpm, the suction mass can be increased by 22 %. Fig. 63 and Fig. 64 show the reason for the suction mass improvement on the basis of the valve lift curves and the suction mass flow of design var. 1, var. 2 and the standard valve. At 5000 rpm, significant differences in valve closing delays between the individual variants can be observed. Delayed valve closing leads to suction gas backflow, see Fig. 64, and thus to a reduction of the suction mass.

In Fig. 62, all MASV design variants show significantly lower max. suction valve impact velocities. Even at 5000 rpm, the max. valve impact velocity limit of 4 m s^{-1} is not exceeded. The high fluctuation of the max. impact velocities is due to the valve oscillation of the MASV. If the valve performs a small upswing shortly before closing at the end of the suction phase, the max. valve impact velocity is strongly reduced.

Design var. 1 shows the best results considering all three responses and the entire compressor speed range. While there is hardly any difference between the design variants in the low to medium compressor speed range, var. 1 leads to significantly larger suction masses at high compressor speeds and keeps the max. suction valve impact velocity below 3 m s^{-1}. Table 24 shows the relative response changes of design var. 1 and var. 2 compared to the standard valve.

Table 24: Relative response change of var. 1 and var. 2 compared to the standard valve.

	var. 1	var. 2	var. 1	var. 2	var. 1	var. 2
n_{comp}	$\Delta v_{\mathrm{sv,imp,max}}$		ΔW_{suc}		Δm_{suc}	
[rpm]	[%]		[%]		[%]	
1500	−87	−56	−66	−67	4.3	4.4
2000	−79	−72	−54	−56	1.4	1.8
2500	−49	−69	−46	−49	0.6	0.7
3000	−60	−56	−37	−40	1.8	1.4
3500	−77	−48	−35	−38	2.3	2.4
4000	−55	−66	−33	−37	8.6	8.2
4500	−92	−27	−33	−38	14.6	2.6
5000	−41	−19	−33	−37	22.0	0.1

3.6 Verification Measurements

The compressor simulation results in section 3.5 showed hardly any difference between the individual optimized design variants from low to medium compressor speed. Since design var. 2 is a combination of the optimized MASV mechanism and the standard valve, it is particularly suitable for first verification measurements representative for all optimized design variants. Therefore, calorimeter and valve dynamics measurements at nominal compressor speeds of 2000 rpm and 3000 rpm were carried out.

Table 25 shows the relative improvement of design var. 2 based on calorimeter measurement results. An improvement of the cooling capacity can be attributed to a higher mass flow per working cycle. At 2000 rpm, the cooling capacity improvement is higher than at 3000 rpm, which agrees with the compressor simulation results in Table 24. Despite the higher mass flow per cycle and the additional friction losses of the MASV mechanism, the power consumption of the compressor decreased due to the reduced suction work. Nevertheless, only a smaller COP improvement could be measured when the compressor speed was reduced from 3000 rpm to 2000 rpm. The reason might be that the friction losses of the MASV mechanism are becoming more relevant at lower compressor speeds.

Table 25: Measured improvement of design var. 2 compared to the standard compressor ($T_{evap} = -23.3$ °C, $T_{cond} = 45$ °C, R600a, ASHRAE test conditions [3]).

$n_{comp,n}$ [rpm]	ΔP_{el} [%]	$\Delta \dot{Q}_0$ [%]	ΔCOP [%]
2000	− 0.4 ± 0.1	+ 1.4 ± 0.4	+ 1.8 ± 0.5
3000	− 1.4 ± 0.1	+ 0.6 ± 0.2	+ 2.0 ± 0.2

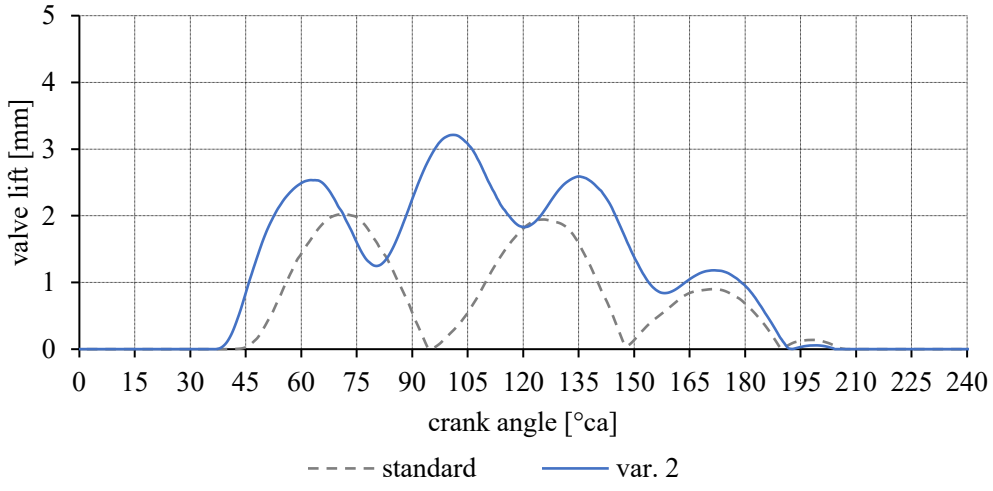

Fig. 66: Comparison of measured suction valve lift related to the crank angle ($T_{evap} = -23.3$ °C, $T_{cond} = 45$ °C, $T_{amb} = T_{sub} = T_{sup} = 32.2$ °C, $n_{comp,n} = 3000$ rpm, R600a).

A comparison of the measured valve lift curves of design var. 2 and standard valve is illustrated in Fig. 66. It shows that design var. 2 opens earlier and faster and remains open during the entire suction phase. Fig. 67 illustrates the corresponding valve velocities. The max. suction valve impact velocity is reduced from approx. 2.5 m s^{-1} to approx. 1 m s^{-1}. Fig. 68 gives a comparison

of the pressure curve in the suction muffler neck. The pressure curve of design var. 2 is much smoother compared to the pressure curve of the standard compressor, which reduces the suction gas pulsation and thus might contribute to noise reduction.

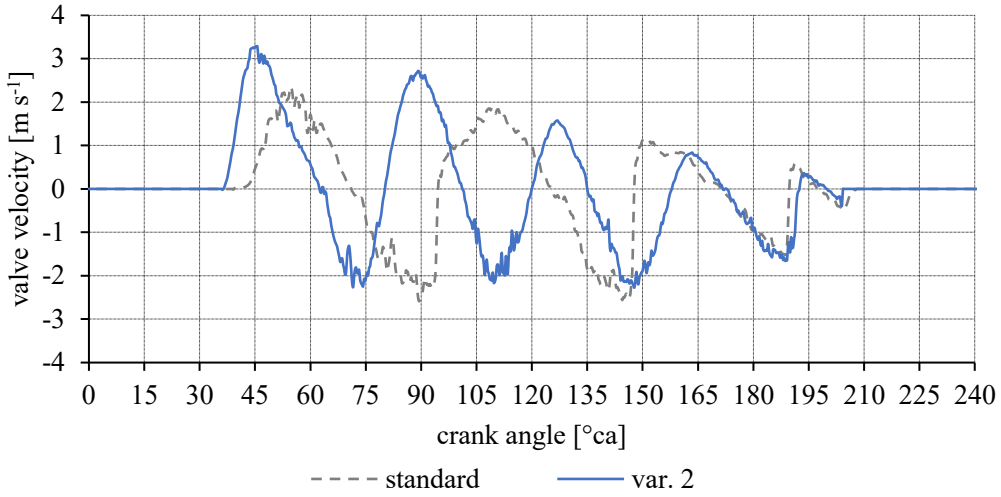

Fig. 67: Comparison of measured suction valve velocity related to the crank angle (T_{evap} = − 23.3 °C, T_{cond} = 45 °C, T_{amb} = T_{sub} = T_{sup} = 32.2 °C, $n_{comp,n}$ = 3000 rpm, R600a).

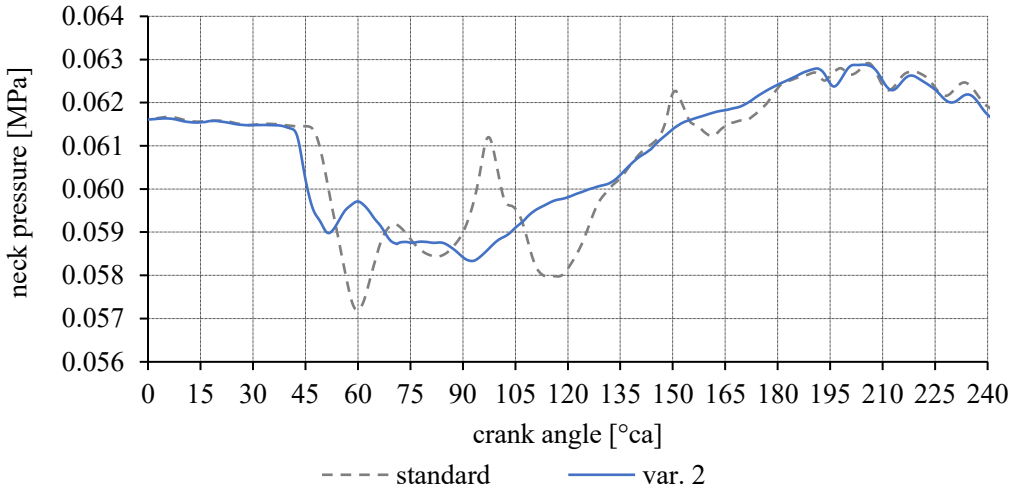

Fig. 68: Comparison of measured suction muffler neck pressure related to the crank angle (T_{evap} = − 23.3 °C, T_{cond} = 45 °C, T_{amb} = T_{sub} = T_{sup} = 32.2 °C, $n_{comp,n}$ = 3000 rpm, R600a).

4 Experimental Investigation of Optimized MASV Design

The main content of this section originates from [23], where the majority of the work was carried out by Andreas Egger. The contribution of the co-authors consisted in supporting the experimental setup and proofreading. The writing itself was solely carried out by Andreas Egger.

The goal of this experimental investigation is to determine the influence of a new MASV design on the performance values, i.e. COP, cooling capacity and acoustics over a wide compressor speed range and different operating conditions. The investigated MASV design is based on design var. 2 (see Table 23), whereby the actuation amplitude was reduced from 2.5 mm to 1.5 mm. A reduction of the actuation amplitude is expected to benefit the acoustic behaviour and the reliability of the compressor as the impact velocity of the spiral spring on the suction valve surface is reduced. Although the investigated MASV design composed of the optimized MASV mechanism and the standard suction reed valve does not lead to the best results over the entire compressor speed range (see section 3.5), results similar to the optimal design variant (design var. 1) are expected from low to medium compressor speeds while, at the same time, requiring fewer modifications to the experimental unit (standard compressor). Table 26 summarizes the most important design parameters of the tested MASV.

Table 26: Design parameter of MASV mechanism.

rod diameter (mm)	actuation amplitude (mm)	actuation phase angle shift (°ca)	spiral spring offset (mm)	spiral spring stiffness (N mm^{-1})
2.0	1.5	0	0	2.0

4.1 Experimental Unit

The MASV mechanism was assembled on a commercially available hermetic reciprocating compressor for R600a with 9.6 cm^3 displacement and a cooling capacity of 171 W (ASHRAE test conditions, 220 V, 50 Hz) as described in section 2.2.1. Fig. 69 shows the experimental unit (without the upper shell cover) which was used for the experimental investigations.

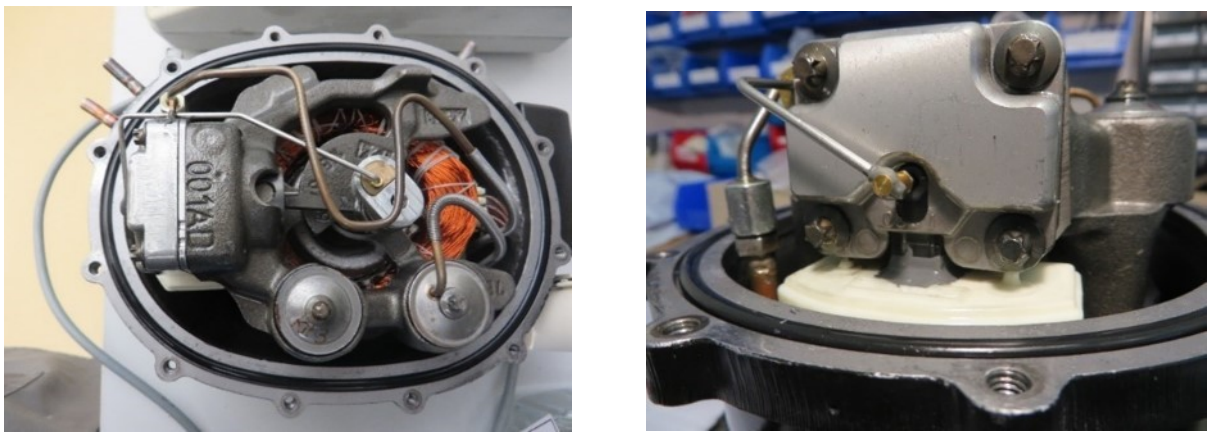

Fig. 69: Hermetic reciprocating compressor equipped with the MASV mechanism (without upper shell cover).

4.2 Experimental Approach

4.2.1 Calorimeter Measurements

A R600a secondary fluid calorimeter testbench as described in section 2.3 was used to determine the performance data, i.e. cooling capacity, electrical power consumption and COP of the compressor.

A total of three different variants were tested in the calorimeter testbench, see Table 27. Beside the standard compressor and the MASV variant, a further variant with an increased suction bore diameter was investigated. It was assumed, that the compressor simulation model described in section 3.2 does not fully cover the effects of different suction bore diameters, since the $\mu\sigma$-value was determined at nominal bore diameter. The underlying experimental investigation should verify this assumption.

Two different operating conditions in terms of evaporating and condensing temperature were tested at nominal compressor speeds starting from 2000 rpm up to 4500 rpm. Based on the measurement results of the cooling capacity and electrical power consumption of the compressor, the COP is calculated according to equation 15. The results obtained with the MASV are given as relative change compared to the standard compressor, e.g. the COP change ΔCOP is calculated according to equation 15.

Table 27: Tested variants with calorimeter testbench.

variant name	MASV	suction bore diameter
standard	no	standard
var. C1	yes	standard
var. C2	yes	+ 7.5 %

Table 28: Tested conditions with calorimeter testbench (based on ASHRAE [3]).

condition name (-)	evaporating temperature (°C)	condensing temperature (°C)	compressor speed (rpm)
− 23.3 °C / 45 °C	− 23.3	45	2000 - 4500 (500rpm steps)
− 23.3 °C / 55 °C	− 23.3	55	2000 - 4500 (500rpm steps)

4.2.2 Acoustic Measurements

Since the compressor is used in domestic refrigerators and freezers, the acoustic behaviour is another important quality criterion. In order to quantify the influence of the MASV on the acoustic behaviour of the compressor, a total of three different variants, as listed in Table 29, were tested with the compressor being operated in a reverberation room. In addition to the measurements of the standard compressor and the MASV (var. A1), a combination of both (var. A2) was tested to determine the acoustic influence of the small gap between the spring rod and the bearing in the suction muffler neck. Therefore, the spring rod was fixed in a position where no contact between the spiral spring and the suction valve could occur.

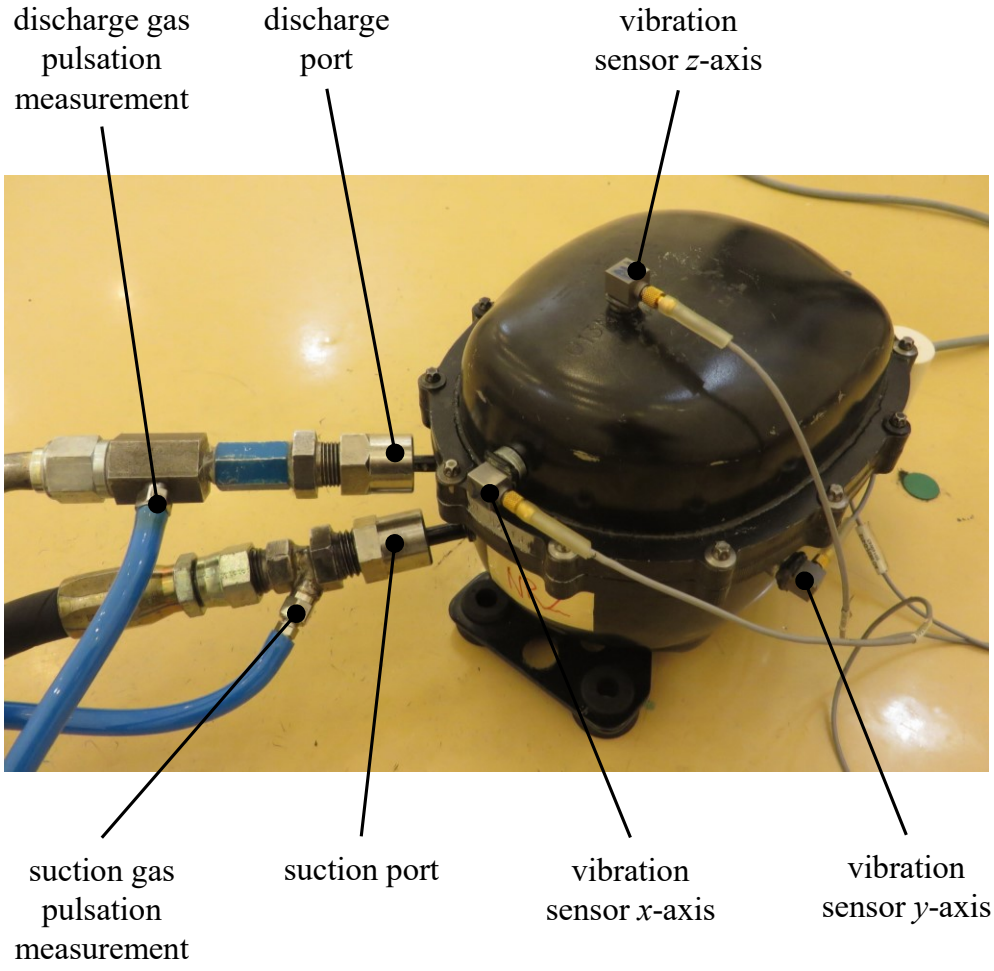

Fig. 70: Measurement setup of acoustic measurements in reverberation room.

Three different acoustic quantities were measured: sound power level, shell vibration as well as suction and discharge gas pulsation. The sound power level was determined according to DIN EN ISO 3741. Sound power level, suction gas pulsation and discharge gas pulsation were measured simultaneously, while the shell vibration had to be measured separately, since the vibration sensors influence the acoustics. The measurement setup of the acoustic measurements in the reverberation room is illustrated in Fig. 70. All three measurements were conducted from 2000 rpm to 4500 rpm at two common operating conditions for acoustic measurements, see Table 30.

Table 29: Tested variants in acoustic investigation.

variant name	MASV	suction bore diameter
standard	no	standard
var. A1	yes	standard
var. A2	yes[1]	standard

[1] to determine the acoustic influence of the small gap between the spring rod and the bearing in the suction muffler neck, the spring rod was fixed in a position where no contact between the spiral spring and the suction valve could occur.

Table 30: Tested conditions in acoustic investigation (based on ASHRAE [3]).

condition name (-)	evaporating temperature (°C)	condensing temperature (°C)	compressor speed (rpm)
− 25 °C / 55 °C (LBP)	− 25	55	2000 - 4500 (500rpm steps)
− 10 °C / 40 °C (MBP)	− 10	40	2000 - 4500 (500rpm steps)

4.3 Results

4.3.1 Calorimeter Measurements

Fig. 71 shows the relative COP change of var. C1 and var. C2 over the compressor speed. The error bars show the standard deviation of the measurement based on several measurement repetitions. In general, significant COP improvements were measured from low to medium compressor speeds. At − 23.3 °C / 45 °C slightly higher improvements are achieved over the entire compressor speed range. This could be due to the design optimisation in section 3, which was carried out for exactly this operating condition.

The results of var. A2 indicate, that a further enlargement of the suction bore has indeed a significant COP improvement potential. Furthermore, the difference between var. A1 and var. A2 increases with increasing compressor speed, which is plausible because the flow losses through the suction bore become more dominant at higher flow speeds. The largest measured COP improvement is about 3.6 % and can be observed at the first operating condition at 4000 rpm.

Fig. 72 illustrates the relative change of the cooling capacity over the compressor speed. In general, the cooling capacity curves of both variants show a similar trend as the corresponding COP curves in Fig. 71. This is not surprising as the cooling capacity is directly included in the calculation of the COP according to equation 14.

At − 23.3 °C / 45 °C, var. C2 shows a continuous increase in cooling capacity improvement from 2000 rpm up to 4000 rpm, with a maximum improvement of 5.8 % at 4000 rpm. At maximum compressor speed, however, var. C1 and var. C2 show large cooling capacity losses compared to the standard compressor. This is in accordance with the findings in section 3.5, where the simulation indicated weak valve dynamics at high compressor speeds if the MASV mechanism is combined with the standard suction reed valve.

Fig. 73 shows the relative change of the electrical power consumption over the compressor speed. The electrical power consumption depends strongly on the mass flow and thus also on the cooling capacity of the compressor. An increase in cooling capacity is associated with an increase in electrical power consumption. The effect of the MASV is clearly visible when comparing the electrical power consumption in Fig. 73 with the cooling capacity in Fig. 72. Some results with cooling capacity changes close to zero, nevertheless, show significant reductions in electrical power consumption, e.g. var. C1 at − 23.3 °C / 45 °C and 2500 rpm. As with the cooling capacity, the electrical power consumption also decreases drastically at maximum compressor speed.

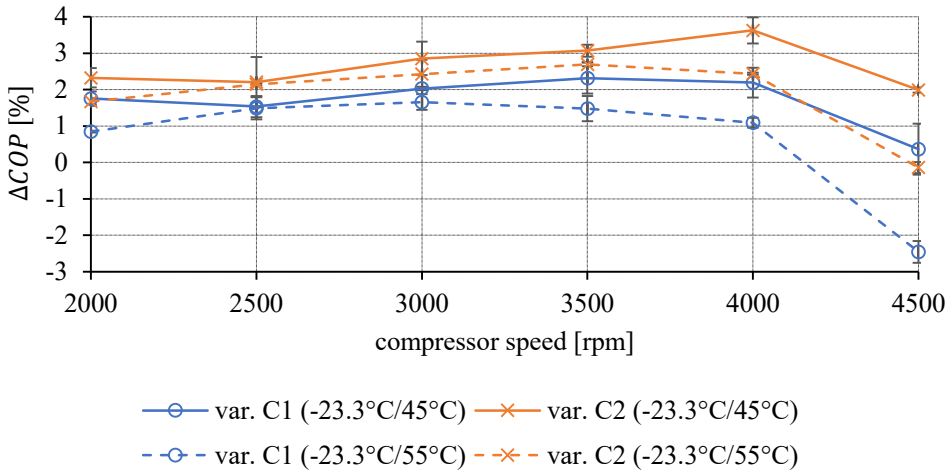

Fig. 71: *COP* change over the compressor speed at two different operating conditions. Test conditions according to ASHRAE [3], R600a.

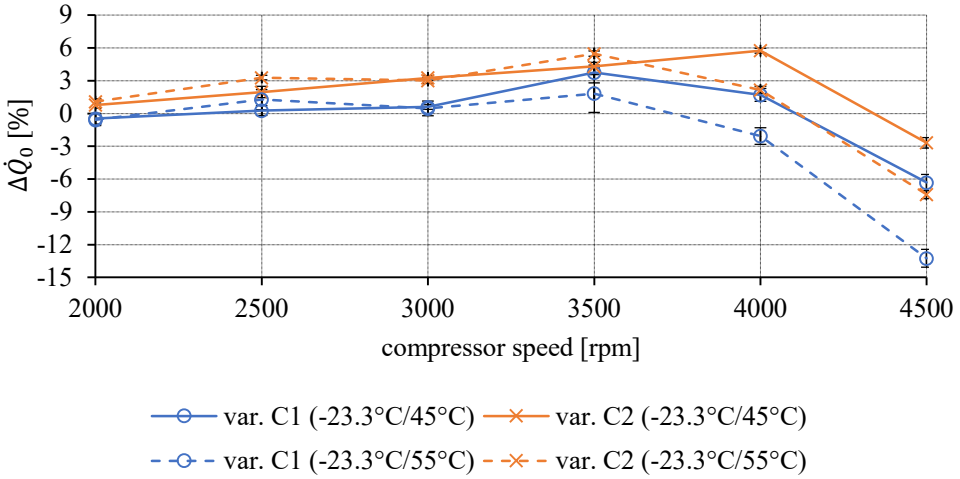

Fig. 72: Cooling capacity change over the compressor speed at two different operating conditions. Test conditions according to ASHRAE [3], R600a.

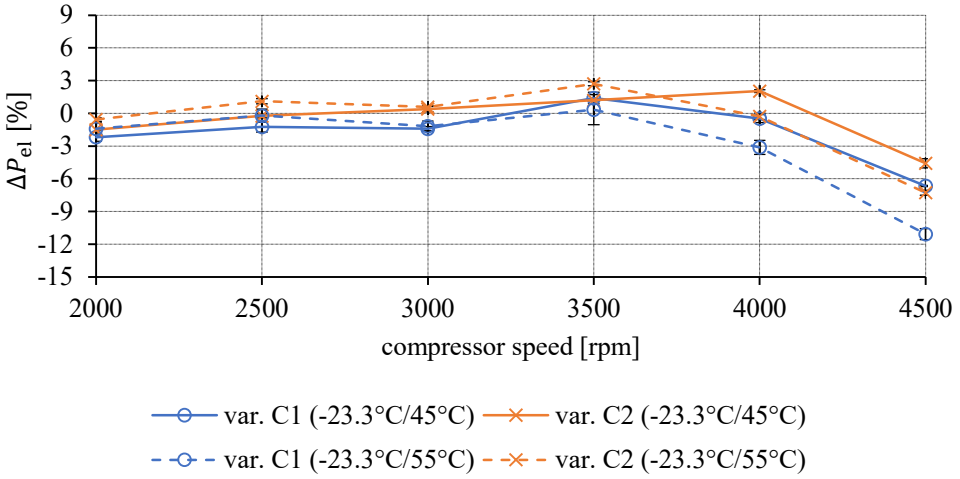

Fig. 73: Electrical power consumption change over the compressor speed at two different operating conditions. Test conditions according to ASHRAE [3], R600a.

4.3.2 Acoustic Measurements

Sound power level

Fig. 74 and Fig. 75 show the measured compressor sound power level in the frequency domain at low (2000 rpm) and high (4500 rpm) compressor speed respectively for – 25 °C / 55 °C (LBP) and − 10 °C / 40 °C (MBP). At − 25 °C / 55 °C and 2000 rpm (Fig. 74), var. A1 shows significant higher sound power levels between 2500 Hz and 6300 Hz than var. A2 and the standard compressor. Since var. A2 has similar levels as the standard compressor, it is likely that the increased level of var. A1 is caused by the mechanism movement rather than by the small gap due to the spring rod bearing in the suction muffler neck.

Fig. 76 shows the total sound power level related to the compressor speed at − 25 °C / 55 °C and – 10 °C / 40 °C. In general, higher compressor speeds lead to higher sound power levels and smaller differences between the individual variants. It turned out, that at − 25 °C / 55 °C, from low to medium compressor speeds, var. A1 leads to considerable higher total sound power levels than the standard compressor, which is in accordance with Fig. 74. At – 10 °C / 40 °C, however, the difference between the individual variants is small.

Furthermore, at a given compressor speed, var. A1 shows smaller differences in sound power level between − 25 °C / 55 °C and − 10 °C / 40 °C than the standard compressor. One explanation for this behaviour could be that the valve impact velocity and the associated noise of the standard compressor increases significantly from − 25 °C / 55 °C to − 10 °C / 40 °C, while the MASV leads to lower and more equalised valve impact velocities.

In general, it can be said that the influence of the compressor speed on the sound power level is much greater than the influence of the MASV.

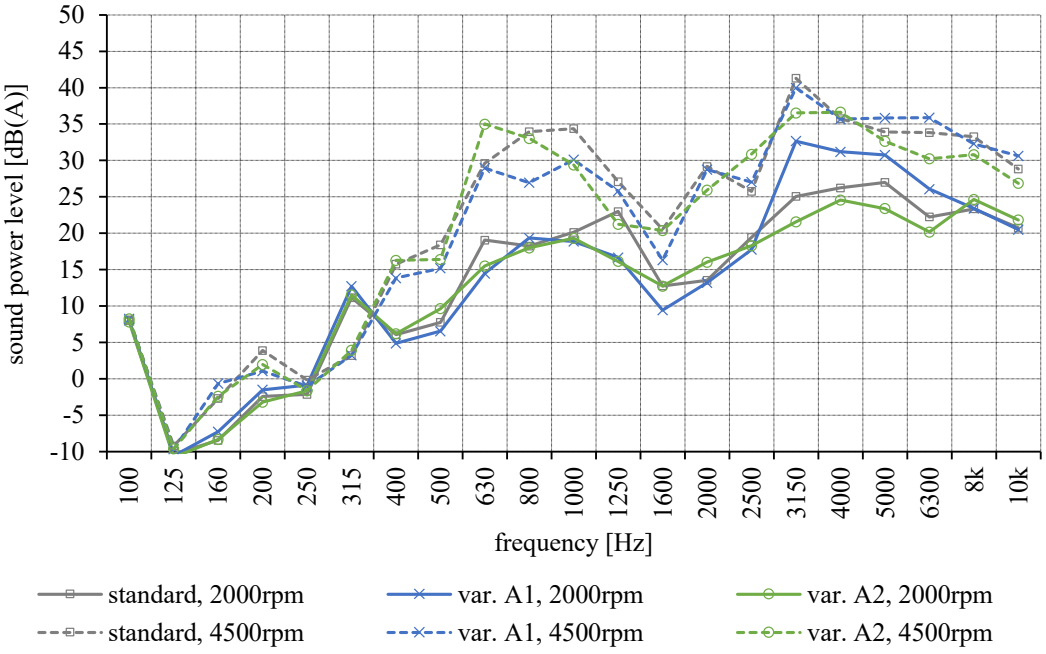

Fig. 74: Compressor sound power level in frequency domain (one-third octave spectrum) at − 25 °C / 55 °C, 2000 rpm and 4500 rpm, sound power reference 1pW.

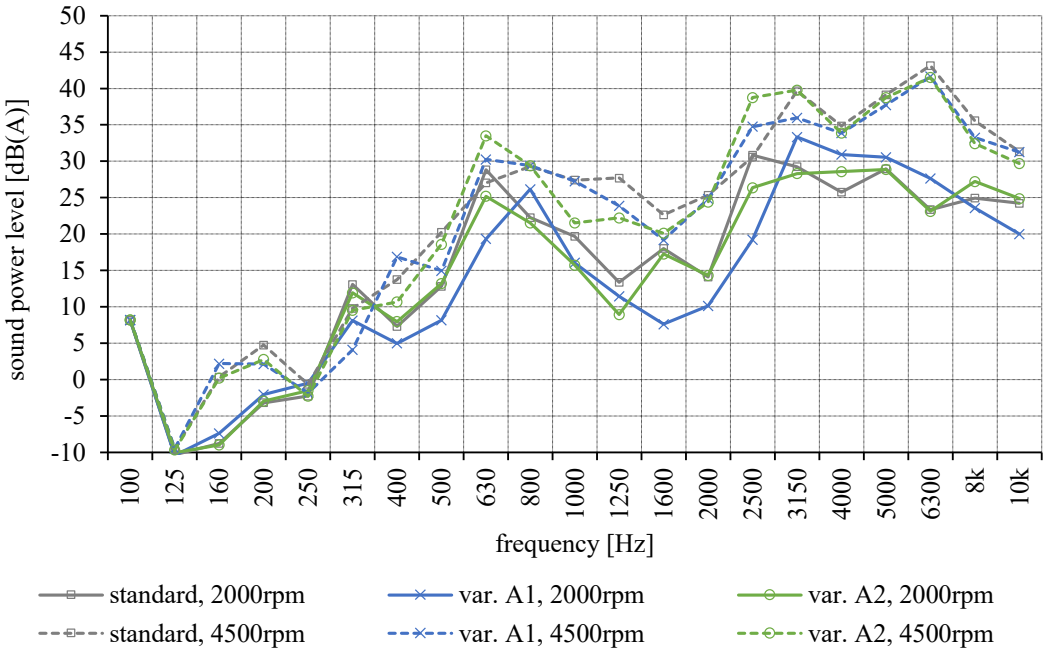

Fig. 75: Compressor sound power level in frequency domain (one-third octave spectrum) at – 10 °C / 40 °C, 2000 rpm and 4500 rpm, sound power reference 1pW.

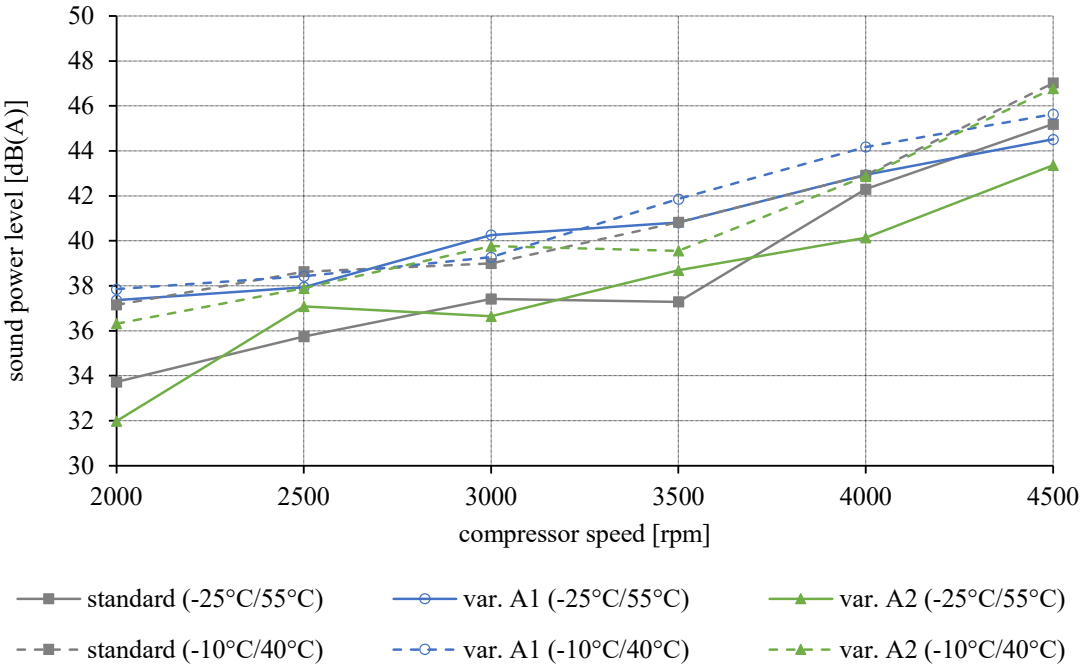

Fig. 76: Total sound power level over compressor speed at – 25 °C / 55 °C and – 10 °C / 40 °C.

Vibration

Fig. 77 and Fig. 78 show the compressor shell vibration in the frequency domain at – 25 °C / 55 °C and – 10 °C / 40 °C at low and high compressor speed. Both plots have a logarithmic ordinate due to the large differences in the size of the vibration values.

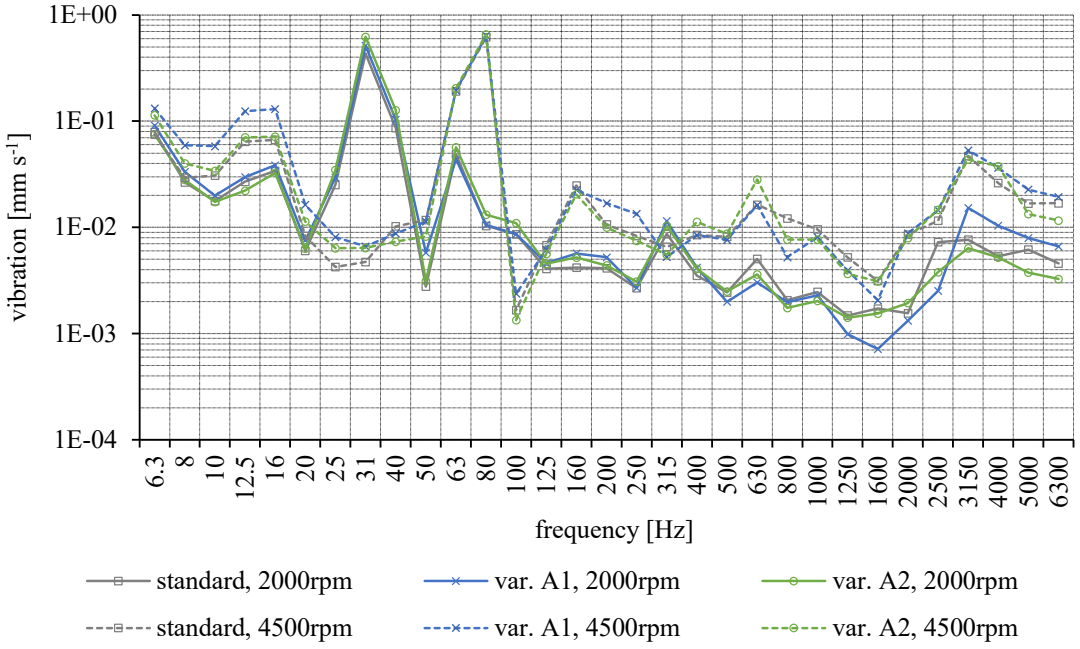

Fig. 77: Shell vibration in frequency domain (one-third octave spectrum) at – 25 °C / 55 °C, 2000 rpm and 4500 rpm.

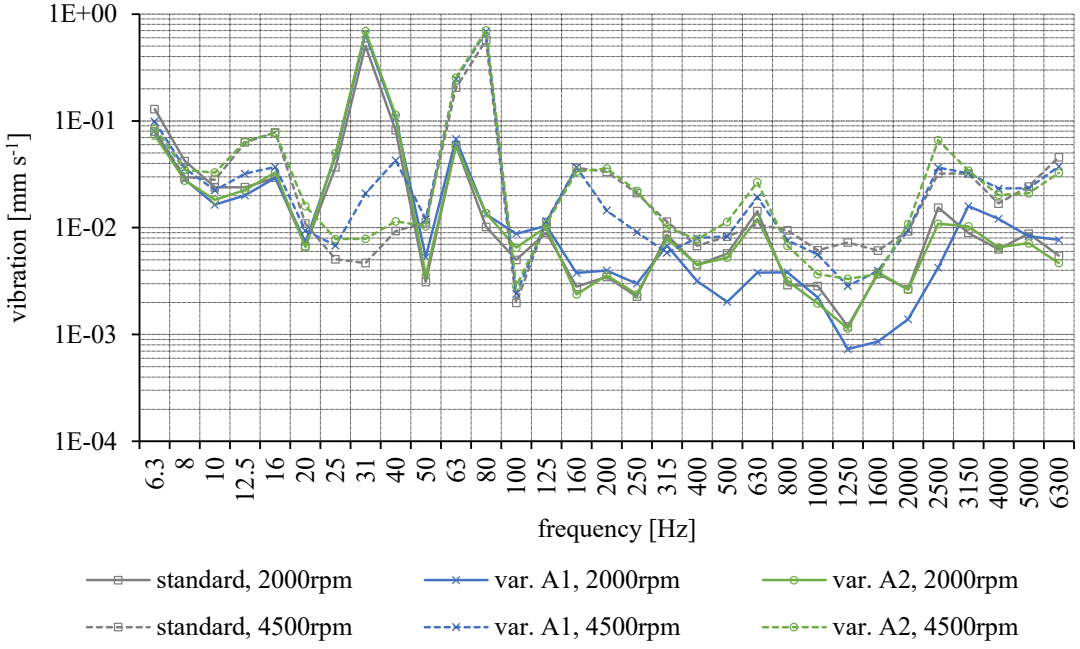

Fig. 78: Shell vibration in frequency domain (one-third octave spectrum) at – 10 °C / 40 °C, 2000 rpm and 4500 rpm.

The highest peaks occur near the operating frequency of the compressor, i.e. 33.3 Hz and 75 Hz for 2000 rpm and 4500 rpm respectively. No difference between the tested variants can be observed at these operation frequency related vibration peaks.

The remaining frequency range of var. A1 sometimes shows a higher and sometimes a lower vibration value compared to the standard compressor. The largest difference occurs at 630 Hz, at operating conditions − 10 °C / 40 °C and 2000 rpm (Fig. 78), where var. A1 has a significantly lower vibration value. However, considering the whole frequency spectrum, no general improvement or worsening of the MASV (var. A1) can be observed.

The small gap in the suction muffler neck caused by the bearing of the spring rod seems to have a neglectable effect on the vibration, because var. A2 has similar vibration values as the standard compressor.

Suction gas pulsation

Fig. 79 and Fig. 80 show the suction gas pulsation in the frequency domain at − 25 °C / 55 °C and − 10 °C / 40 °C at low and high compressor speed. As with the shell vibration measurement, the largest peaks in suction gas pulsation occur near the operating frequency of the compressor.

At 2000 rpm a significant reduction of the suction gas pulsation roughly between 250 Hz and 4000 Hz can be observed at both operating conditions. At 4500 rpm the reduction is slightly less pronounced. This could be due to the fact that higher compressor speeds lead to fewer intermediate valve closings, as the suction time decreases while the valve flutter frequency remains the same. Also, with regard to suction gas pulsation, the small gap in the suction muffler neck seems to be neglectable. The discharge gas pulsation is not influenced by the MASV and, therefore, not discussed further in the results.

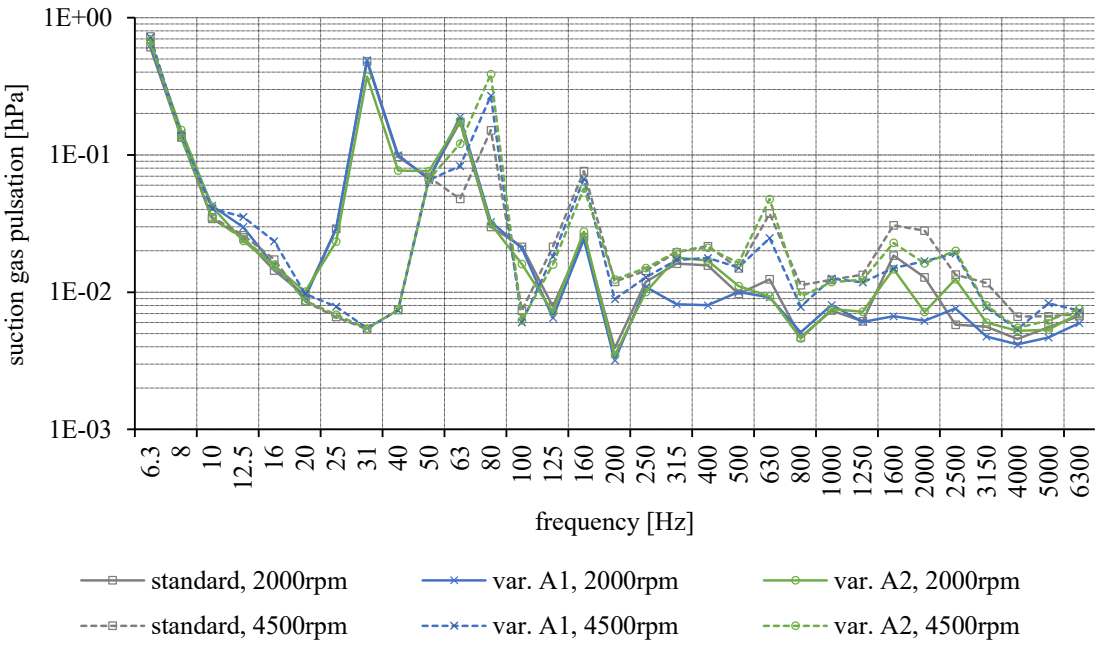

Fig. 79: Suction gas pulsation in frequency domain (one-third octave spectrum) at − 25 °C / 55 °C, 2000 rpm and 4500 rpm.

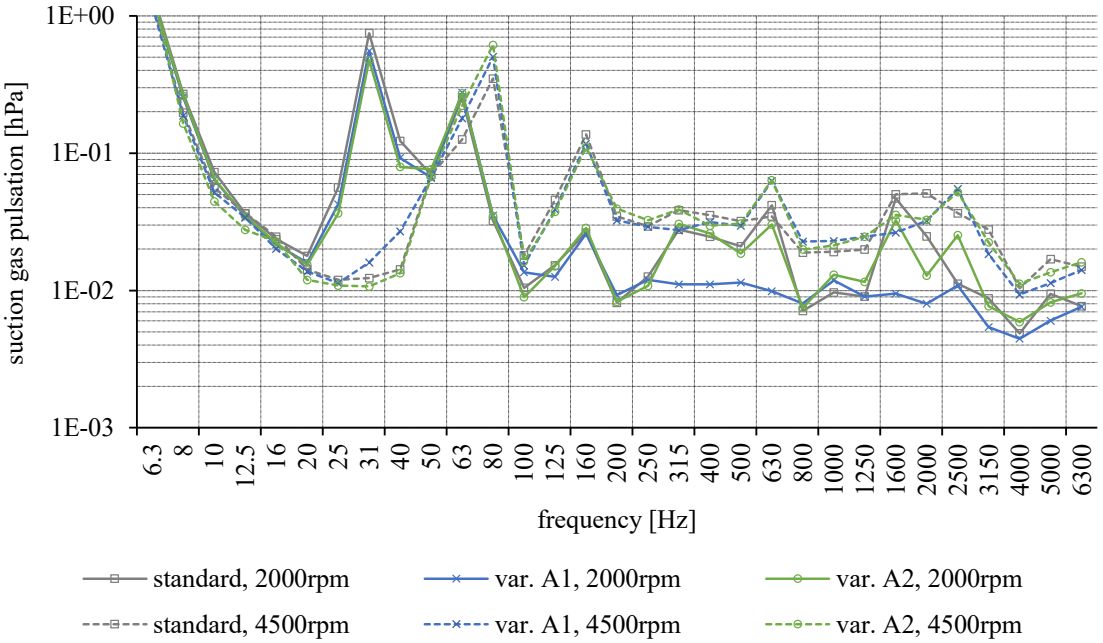

Fig. 80: Suction gas pulsation in frequency domain (one-third octave spectrum) at – 10 °C / 40 °C, 2000 rpm and 4500 rpm.

5 Summary

A novel, cost-effective concept of a mechanically assisted suction reed valve (MASV) was investigated based on a small hermetic reciprocating compressor for domestic refrigeration. The concept consists of a simple MASV mechanism and a reed valve of conventional shape.

After a proof-of-concept with an initial design, an in-house compressor simulation model was adopted for the compressor under investigation and extended to include the MASV system. Once the compressor simulation model had been validated with measurement data, several response models were created aiming to simultaneously improve the efficiency, cooling capacity, acoustics and reliability based on a multi-response optimization approach. Finally, extensive measurements of an optimized design variant were carried out to experimentally investigate the MASV regarding its actual improvements at various operating conditions and compressor speeds.

Surrogate Model Based Design Optimization of MASV

It turned out, that the investigated MASV is very robust in the reduction of the suction work. Simulations between 1500 rpm and 5000 rpm showed only small differences between the initial design and the optimized design variants. The lower the compressor speed, the higher the percentage of the suction work reduction. However, as the power consumption of the compressor decreases with decreasing compressor speed, the additional friction losses due to the MASV mechanism account for a larger proportion of the entire power consumption. This might be the reason why in initial verification measurements only a smaller COP improvement could be measured when the compressor speed was reduced from 3000 rpm to 2000 rpm.

Compared to the suction work, the suction mass is more sensitive to the design of the MASV. Simulations at different compressor speeds showed that the optimized design variants lead to significantly higher suction masses than the initial design and the standard valve. While the individual optimized design variants hardly differ from low to medium compressor speed, the difference is large at high compressor speeds. The best results at high compressor speeds were obtained with a reed valve design based on a high stiffness to mass ratio, which results in a high natural frequency of the valve. Simulations at 5000 rpm resulted in a suction mass increase of up to 22 % due to reduced valve closing delays. Assuming no additional backflow at the discharge valve, this would lead to a 22 % increase of the cooling capacity.

All optimized design variants led to significantly lower max. suction valve impact velocities than the standard valve. Even at 5000 rpm, most of the optimized design variants had max. valve impact velocities well below 4 m s^{-1}. A lower valve impact velocity corresponds to a lower impact stress, leading to a longer valve lifetime and thus to a higher reliability of the compressor. Assuming a given limit for the max. valve impact velocity, the MASV enables higher compressor speeds than the standard valve and, thereby, helps to increase the cooling capacity range of a variable-speed compressor.

Experimental Investigation of Optimized MASV Design

Calorimeter measurements indicated a significant increase of the COP at almost every compressor speed and operating condition when using the MASV. The highest COP improvements, up to 3.6 %, were obtained when the MASV was combined with an enlarged

suction bore. In the standard compressor, a suction bore enlargement is hardly feasible, as it usually increases the valve impact velocity, which is already close to the limit from reliability perspective. However, the MASV significantly reduces the valve impact velocity, making a suction bore enlargement feasible.

Not only the COP, but also the cooling capacity could be increased with the MASV. As with the COP, the highest cooling capacity improvements were obtained when the MASV is combined with a suction bore enlargement. From low to medium compressor speeds, improvements in cooling capacity tended to increase with increasing compressor speed. At 4500 rpm, however, a strong decline in cooling capacity was observed. According to the results of the design optimization, the MASV concept would basically be able to improve COP and cooling capacity even at high compressor speeds. However, this would require a suction reed valve design with valve parameters that are difficult to implement in the existing compressor design.

The acoustic measurements indicated that the sound power level of the compressor increases considerably at LBP from low to medium compressor speeds, when using a MASV. This can be attributed to the motion of the MASV mechanism and most likely has its origin in the bearing points. At MBP, which is usually the noisier operating condition, the total sound power level of the compressor equipped with the MASV remains almost the same as at LBP. This is why at MBP no significant differences in total sound power level between standard and MASV could be observed. The shell vibration measurement indicated no fundamental changes when using the MASV, while the suction gas pulsation between 250 Hz and 4000 Hz at 2000 rpm was significantly reduced.

6 Conclusion

A new valve concept (MASV) to improve the energy efficiency of fixed and variable-speed compressors for domestic refrigeration was presented. Extensive simulation and measurement-based investigations not only show the influence on important performance values such as COP, cooling capacity, reliability and acoustics, but also give a detailed insight into how the system works and which aspects are important to obtain an optimally working system.

The MASV, especially in combination with a larger suction bore, allows COP improvements of more than 3 %, whereby higher compressor speeds tend to achieve better results. In addition, it leads to a significant reduction in valve stress by avoiding intermediate valve impacts and a substantial reduction in valve impact velocity.

At low to medium compressor speeds, the MASV results in a higher overall sound power level of the compressor, possibly due to the current design of the mechanism, particularly the bearings. The shell vibration seems to remain almost the same, while the suction gas pulsation can be significantly reduced.

The current market value of around 1 % COP improvement for high efficiency refrigerant compressors is around 0.5 €. This means that the additional cost of integrating a MASV into a standard compressor can be a maximum of 1.5 €, assuming a COP improvement of 3 %. Considering the simplicity of the mechanism, the high production volumes of this type of compressors and assuming that it can be integrated into the highly automated assembly process of modern hermetic reciprocating compressors, the MASV also appears feasible from an economic point of view.

To successfully use the MASV in a standard compressor, a further investigation of the bearing situation is necessary. It is suspected that the bearing clearance in the current design of the MASV deteriorates the compressor acoustics. At the same time, if the bearing clearance is too small, there is a risk that the mechanism gets stuck. An industrial application of the proposed MASV also requires a more in-depth consideration of manufacturability and integrability into the highly automated assembly process. In addition, the reliability of the system must be proven in durability tests. This is also one of the most demanding barriers, as significantly more than 10^9 valve opening processes take place during the required lifespan of 15 – 20 years.

A successful global application of the MASV in all future compressors used in domestic refrigeration appliances would lead to annual electricity savings of 2.7TWh - 5.5TWh, assuming a 3 % increase in energy efficiency, an annual sales volume of currently approx. 250 million pcs. [54, 55] and an average energy consumption of 365 - 730 kWh per appliance and year. This corresponds to about 3.8% - 7.6% of Austria's annual electricity consumption, which was 71.8TWh [20] in 2019.

References

[1] Abidin, Z., Lang, W., Almbauer, R. A., Nagy, D., and Burgstaller, A. 2009. Development and validation of a one-dimensional simulation model of a hermetic reciprocating compressor for household refrigeration. *IJESMS* 1, 4, 193.

[2] Aigner, R. and Steinrück, H. 2007. Modelling Fluid Dynamics, Heat Transfer and Valve Dynamics in a Reciprocating Compressor. *5th Conference of the EFRC*, 171–179.

[3] American Society of Heating, Refrigerating and Air-Conditioning Engineers. 2010. *ANSI/ASHRAE Standard 23.1-2010. Methods of Testing for Rating the Performance of Positive Displacement Refrigerant Compressors and Condensing Units that Operate at Subcritical Temperatures of the Refrigerant*, Atlanta, Ga.

[4] American Society of Heating, Refrigerating and Air-Conditioning Engineers. 2013. *2013 ASHRAE Handbook. FUNDAMENTALS*. ASHRAE, Atlanta, GA.

[5] American Society of Heating, Refrigerating and Air-Conditioning Engineers. 2014. *2014 ASHRAE HANDBOOK. REFRIGERATION*. ASHRAE, Atlanta, GA.

[6] American Society of Heating, Refrigerating and Air-Conditioning Engineers. 2016. *2016 ASHRAE HANDBOOK. Heating Ventilating and Air-Conditioning Systems and Equipment*. ASHRAE, Atlanta, GA.

[7] Aylmer Fisher, R. 1926. The arrangement of field experiments. *Journal of the Ministry of Agriculture,* 33, 503–515.

[8] Aylmer Fisher, R. 1935. *The Design of Experiments*. Oliver and Boyd, Edinburgh.

[9] bdew. 2020. *Stromverbrauch der Haushalte*. https://www.bdew.de/service/daten-und-grafiken/stromverbrauch-der-haushalte/. Accessed 7 December 2020.

[10] Bhakta, A., Dhar, S., Bahadur, V., Angadi, S., and Dey, S. 2012. A Valve Design Methodology For Improved Reciprocating Compressor Performance. *International Compressor Engineering Conference*.

[11] Blauert, J. and Xiang, N. 2009. *Acoustics for Engineers. Troy Lectures*. Springer-Verlag Berlin Heidelberg, Berlin, Heidelberg.

[12] Box, G. E. P. and Behnken, D. W. 1960. Some New Three Level Designs for the Study of Quantitative Variables. *Technometrics* 2, 4, 455–475.

[13] Box, G. E. P. and Wilson, K. B. 1951. On the Experimental Attainment of Optimum Conditions. Journal of the Royal Statistical Society: Series B (Methodological), 13(1), 1-38. *Journal of the Royal Statistical Society: Series B (Methodological)* 13, 1, 1–38.

[14] Burgstaller, A. 2009. *Ansätze zu thermodynamischen Analysen und Bewertung von hermetisch verschlossenen Systemen am Beispiel von Kleinkältemittelkompressoren*. Dissertation, Technische Universität Graz.

[15] Burgstaller, A., Nagy, D., Almbauer, R., and Lang, W. 2008. Influence of the Main Parameters of the Suction Valve on the Overall Performance of a Small Hermetic Reciprocating Compressor. *International Compressor Engineering Conference*.

[16] Collings, D. A. and Lenz, J. R. 2010. A Study of Flapper Valve Motion in a Variable Speed Compressor. *International Compressor Engineering Conference*.

[17] Costagliola, M. 1950. The Theory for Spring Loaded Valves for Reciprocating Compressors. *Journal of Applied Mechanics,* vol. 17, 415–420.

[18] Dean, A., Voss, D., and Draguljić, D. 2017. *Design and Analysis of Experiments*. Springer Texts in Statistics. Springer, Cham.

[19] Derringer, G. and Suich, R. 1980. Simultaneous Optimization of Several Response Variables. *Journal of Quality Technology,* 12, 214–219.

[20] E-Control. 2020. *Statistikbroschüre 2020. Unsere Energie in Zahlen gemessen*, Wien.

[21] Egger, A., Almbauer, R., Dür, L., Hopfgartner, J., and Lang, M. 2020. Multi-Response optimization applied to a mechanically assisted reed valve of a hermetic reciprocating compressor. *International Journal of Refrigeration* 119, 119–130.

[22] Egger, A., Almbauer, R., Dür, L., Hopfgartner, J., Zuber, B., and Stangl, S. 2019. Experimental Investigation of a Mechanically Assisted Suction Reed Valve in a Small Hermetic Reciprocating Compressor. *IOP Conference Series: Materials Science and Engineering* 604, 12018.

[23] Egger, A., Almbauer, R., Lang, M., and Zainer, C. (in press). Experimental Investigation of an Optimized Mechanically Assisted Suction Reed Valve Design Concept in a Small Hermetic Reciprocating Compressor. *International Compressor Engineering Conference* ((in press)).

[24] European Union. 2010. *COMMISSION DELEGATED REGULATION (EU) No 1060/2010 of 28 September 2010 supplementing Directive 2010/30/EU of the European Parliament and of the Council with regard to energy labelling of household refrigerating appliances*.

[25] European Union. 2019. *COMMISSION DELEGATED REGULATION (EU) 2019/2016 of 11 March 2019 supplementing Regulation (EU) 2017/1369 of the European Parliament and of the Council with regard to energy labelling of refrigerating appliances and repealing Commission Delegated Regulation (EU) No 1060/2010*.

[26] Gonzalez, I., Lehmkuhl, O., Naseri, A., Rigola, J., and Oliva, A. 2016. Fluid-Structure Interaction of a Reed Type Valve. *International Compressor Engineering Conference*.

[27] Habing, R. A. and Peters, M.C.A.M. 2006. An experimental method for validating compressor valve vibration theory. *Journal of Fluids and Structures* 22, 5, 683–697.

[28] Harrington, E. C. 1965. The desirability function. *Industrial Quality Control,* Vol.21, 494–498.

[29] Heimel, M. 2015. *Simulation and experimental validation of adiabatic and non-adiabatic capillary tubes*. Dissertation, Graz University of Technology.

[30] Hopfgartner, J., Posch, S., Zuber, B., Almbauer, R., Krischan, K., and Stangl, S. 2017. Reduction of the suction losses through reed valves in hermetic reciprocating compressors using a magnet coil. *IOP Conference Series: Materials Science and*

Engineering 232, 12034.

[31] IEC. 2007. *Household refrigerating appliances - Characteristics and test methods*. International Electrotechnical Commission, 62552:2007.

[32] IIR. 2019. *The Role of Refrigeration in the Global Economy*. 38th Note on Refrigeration Technologies. https://iifiir.org/en/fridoc/142028.

[33] Jones, B. 2011. A Class of Three-Level Designs for Definitive Screening in the Presence of Second-Order Effects. *Journal of Quality Technology* 43, 1.

[34] Kadane, J. B. and Lazar, N. A. 2004. Methods and Criteria for Model Selection. *Journal of the American Statistical Association* 99, 465, 279–290.

[35] Kopppula, J. S., Rajagopal, T. K. R., and Gundabattini, E. 2017. Correlating the Experiment and Fluid Structure Interaction Results of a Suction Valve Model from a Hermetic Reciprocating Compressor. In *International Conference on Advances in Design, Materials, Manufacturing and Surface Engineering for Mobility*. SAE International. DOI=10.4271/2017-28-1948.

[36] Lawson, J. 2014. *Design and Analysis of Experiments with R*. Chapman and Hall/CRC Texts in Statistical Science Ser v.115. Chapman and Hall/CRC, Boca Raton.

[37] Lawson, J. 2016. *daewr: Design and Analysis of Experiments with R*. R package version 1.1-7.

[38] Letschert, V., Desroches, L.-B., Ke, J., and McNeil, M. 2013. Energy efficiency – How far can we raise the bar? Revealing the potential of best available technologies. *Energy* 59, 72–82.

[39] Li, X., Sudarsanam, N., and Frey, D. D. 2006. Regularities in data from factorial experiments. *Complexity* 11, 5, 32–45.

[40] Lohn, S. K., Lange Pereira, E. L., Ferreira Camara, H., and Deschamps, C. J. 2016. Experimental Investigation of Damping Coefficient for Compressor Reed Valves. *International Compressor Engineering Conference*.

[41] Montgomery, D. C. 2017. *Design and analysis of experiments*, Arizona State University.

[42] Möser, M. 2015. *Technische Akustik*. VDI-Buch. Springer Vieweg, Berlin, Heidelberg.

[43] Mu, G., Wang, F., Mi, X., and Gao, G. 2019. Dynamic modeling and analysis of compressor reed valve based on movement characteristics. *Applied Thermal Engineering* 150, 522–531.

[44] Nagata, S., Nozaki, T., and Akizawa, T. 2010. Analysis of Dynamic Behavior of Suction Valve Using Strain Gauge in Reciprocating Compressor. *International Compressor Engineering Conference*.

[45] Pischinger, R., Klell, M., and Sams, T. 2002. Analyse und Simulation des Systems Brennraum. In *Thermodynamik der Verbrennungskraftmaschine*, R. Pischinger, M. Klell and T. Sams, Eds. Springer Vienna, Vienna, 157–301. DOI=10.1007/978-3-7091-3826-7_4.

[46] Pizarro-Recabarren, R. A., Barbosa, J. R., and Deschamps, C. J. 2013. Modeling the stiction effect in automatic compressor valves. *International Journal of Refrigeration* 36, 7, 1916–1924.

[47] Real, M. A. and Gomes Pereira, E. A. 2010. Using PV Diagram Synchronized With the Valve Functioning to Increase the Efficiency on the Reciprocating Hermetic Compressors. *International Compressor Engineering Conference*.

[48] Ribas, F., Deschamps, C., Fagotti, F., Morriesen, A., and Dutra, T. 2008. Thermal Analysis of Reciprocating Compressors - A Critical Review. *Proceedings of the International Compressor Engineering Confconference Purdue*.

[49] RStudio Team. 2016. *RStudio: Integrated Development Environment for R*. RStudio, Inc., Boston, MA.

[50] Ryan, T. P. 2007. *Modern experimental design*. Wiley series in probability and statistics. Wiley-Interscience, Hoboken, NJ.

[51] Secop. *HXK95AA KAPPA LBP Compressor Superior Efficiency R600a 220-240V 50Hz*. https://www.secop.com/fileadmin/user_upload/SEPS/datasheets/hxk95aa_cdo00085_r600a_220v_50hz_12-2016_desd564r102.pdf. Accessed 8 December 2020.

[52] Siebertz, K., van Bebber, D., and Hochkirchen, T. 2017. *Statistische Versuchsplanung. Design of Experiments (DoE)*. VDI-Buch Ser. Vieweg, Berlin, Heidelberg.

[53] Soedel, W. 2007. *Sound and Vibrations of Positive Displacement Compressors*. Taylor & Francis Ltd, Hoboken.

[54] Statista. *Kühlschränke - weltweit*. https://de.statista.com/outlook/16010100/100/kuehlschraenke/weltweit. Accessed 9 December 2020.

[55] Statista. *Tiefkühltruhen - weltweit*. https://de.statista.com/outlook/16010200/100/tiefkuehltruhen/weltweit. Accessed 9 December 2020.

[56] Stefan, P. 2017. *Thermodynamic Influence of the Lubrication Oil in Hermetic Reciprocating Compressors,* Graz University of Technology.

[57] Tan, Q., Pan, S.-l., Feng, Q.-k., Yu, X.-l., and Wang, Z.-l. 2014. Fluid–structure interaction model of dynamic behavior of the discharge valve in a rotary compressor. *Proceedings of the Institution of Mechanical Engineers, Part E: Journal of Process Mechanical Engineering* 229, 4, 280–289.

[58] Tao, W., Guo, Y., He, Z., and Peng, X. 2018. Investigation on the delayed closure of the suction valve in the refrigerator compressor by FSI modeling. *International Journal of Refrigeration* 91, 111–121.

[59] The MathWorks, I. 2017. *MATLAB R2017b*, Natick, Massachusetts, United States.

[60] The MathWorks, I. 2017. *Optimization Toolbox version 8.0*, Natick, Massachusetts, United States.

[61] United Nations. 2016. *Paris Agreement*.

[62] Wang, F., Mu, G., and Guo, Q. 2016. Design optimization of compressor reed valve

based on axiomatic design. *International Journal of Refrigeration* 72, 132–139.

[63] Wang, Y., Feng, J., Zhang, B., and Peng, X. 2012. Modeling the valve dynamics in a reciprocating compressor based on two-dimensional computational fluid dynamic numerical simulation. *Proceedings of the Institution of Mechanical Engineers, Part E: Journal of Process Mechanical Engineering* 227, 4, 295–308.

[64] Wang, Y., Xue, C., Feng, J., and Peng, X. 2013. Experimental investigation on valve impact velocity and inclining motion of a reciprocating compressor. *Applied Thermal Engineering* 61, 2, 149–156.

[65] Yoshizumi, F., Kondoh, Y., Moroi, T., Tamano, S., and Morinishi, Y. 2014. Numerical Simulation on the Opening Delay of a Discharge Reed Valve in Compressors. *International Compressor Engineering Conference*.